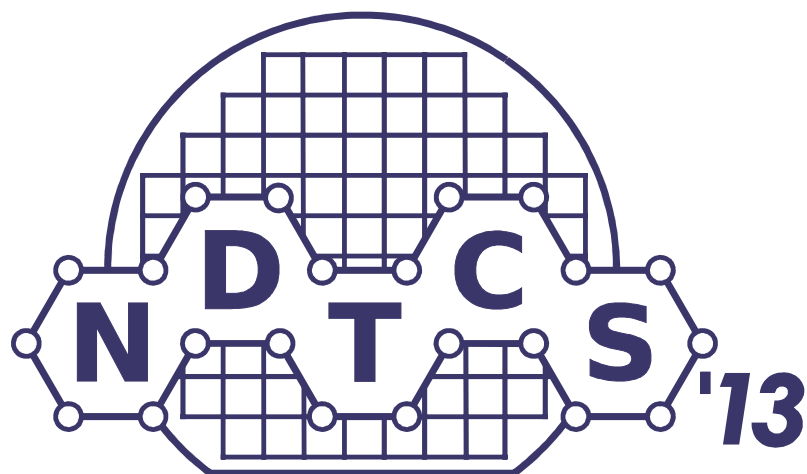# NANO-DESIGN, TECHNOLOGY, COMPUTER SIMULATIONS (NDTCS '13)

June 11-15, 2013

MINSK, BELARUS

Fifteenth International Workshop on

New Approaches to High-Tech:
Nano-Design, Technology, Computer Simulations

Preprints

June 11-15, 2013
Minsk, Belarus

Organized by

The Ministry of Education of the Republic of Belarus

Belarusian State University of Informatics and Radioelectronics (Belarus)

St. Petersburg Academy of Sciences for Strength Problems (Russia)

Sponsored by

LG Electronics

Research and Production Corporation Integral

Infopark Company

Edited by
V. Nelayev, V. Stempitsky

Volume 15

Published by
Belarusian State University of Informatics and Radioelectronics

EDITORIAL BOARD

A. Melker, *V. Nelayev*, *V. Stempitsky*

Proceedings of Fifteenth International Workshop on New Approaches to High-Tech: Nano-Design, Technology, Computer Simulations – NDTCS'2013, June 11-15 2013, Minsk, Belarus, BSUIR, 130 pages.

> Proceedings contain papers presented at 15th International Workshop "Nano-Design, Technology, Computer Simulations" and devoted to investigations in the fields of electronic, atomic and molecular dynamics, biology systems, nanomaterials and nanotechnologies, nano-, micro- and macromechanics and computer technologies and simulation.

INTERNATIONAL ORGANIZING COMMITTEE
Co-chairs of International Organizing Committee

Alexander Melker	Saint-Petersburg Academy of Sciences on Strength Problems, Russia
Vladislav Nelayev	Belarusian State University of Informatics and Radioelectronics (BSUIR), Belarus

INTERNATIONAL PROGRAM COMMITTEE

Alexandra Bezrukova	Saint-Petersburg State Polytechnical University, Russia
Teodor Breczko	University of Bialystok, Poland
Kirill Dobrego	Institute of Heat and Mass Transfer NAS B, Belarus
Sergey Kilin	B.I. Stepanov Institute of Physics NAS B, Belarus
Victor Feodorov	Derzhavin Tambov State University, Russia
Esko Kauppinen	Aalto University, Finland
Wieslaw Kuzmicz	Warsaw University of Technology, Poland
Vladimir Monin	Universidade do Estado do Rio de Janeiro, Brazil
Albert Nasibulin	Aalto University, Finland
Albrecht Ott	Universität des Saarlandes, Germany
Andrey Sanin	Saint-Petersburg State Polytechnical University, Russia
Jelena Tamuliene	Vilnus University, Lithuania
Vitali Tatartchenko	Saint-Gobain Crystals, Paris, France
Lyudmila Yakovenkova	Institute of Metal Physics, Ural Division of the Russian Academy of Sciences, Yekaterinburg, Russia

BELARUSIAN NATIONAL ORGANIZING COMMITTEE

Mikhail Batura	BSUIR Rector (Chair)
Vyacheslav Barkaline	Belarusian National Technical University (BNTU)
Viktor Borisenko	BSUIR, Belarus
Vladimir Borzdov	Belarusian State University (BSU)
Alexander Daniljuk	BSUIR
Sergey Gaponenko	Institute of Molecular and Atomic Physics NAS B
Alexander Gursky	BSUIR
Vladimir Labunov	BSUIR
Viktor Stempitsky	BSUIR

© Belarusian State University of Informatics and Radioelectronics, 2013

WORKSHOP SUPPORTED BY:

LG Electronics, Inc. is a global leader and technology innovator in consumer electronics, mobile communications and home appliances, employing 87,000 people working in over 110 locations around the world. LG comprises four business units – Home Entertainment, Mobile Communications, Home Appliance, and Air Conditioning & Energy Solution – and is one of the world's leading producers of flat panel TVs, mobile devices, air conditioners, washing machines and refrigerators.

From mobile innovations to digital media technology, LG is leading the electronics industry and bringing technology into your home. The LG Institute of Technology was founded to nurture ongoing innovation like improving energy devices, multimedia processing, and wireless networks around the world.

LG focuses on gaining advanced technologies to drive you forward. Our vigorous commitment to R&D is demonstrated by our creation of the world's first Blu-ray disc and the next-generation flat-panel display.

To achieve its lofty goals, LG Electronics continuously recruits new talent and strives to increase its global business by consolidating R&D systems oriented toward local markets in strategic countries such as China and India. The company is also building international R&D capacity by pushing ahead on strategic alliances with other major companies in regard to standardization and new products.

LG Electronics operates a global R&D system that consists of more than 30 research centers around the world. Through this system, the company facilitates open innovation utilizing innovative technologies from the outside, in order to secure core technologies and the early identification of future growth engines. In all these ways, LG is on target toward realizing its vision: Top Global R&D.

INTEGRAL JSC develops, manufactures and exports microelectronic components and electronic products.

INTEGRAL JSC provides a full cycle of design and manufacture: from silicon substrates up to integrated circuits and semiconductor devices, from microelectronic components up to electronic.

The main line of activity of INTEGRAL JSC is design and manufacture of microelectronic products - over 70 % of the total production volume - for the branches manufacturing goods of household and consumer electronics, electronic and medical devices.

INTEGRAL JSC exports more than 70 % of the volume of manufactured goods to the markets of the Russian Federation, South - East Asia, India and Western Europe.

The goods are exported to 28 countries of the world.

The main lines of the development of INTEGRAL JSC are as follows: design and implementation of microelectronic components of power electronics, microsensorics and optoelectronics.

Development of production of finished electronics is to be carried out in the following lines: displays; automotive electronics and electronics and equipment for health application: cashless payment systems, payment terminals, commercial and bank equipment, smart cards, identification and record keeping systems.

INTEGRAL JSC is open for cooperation both in design and deliveries of products, and in terms of joint realization of long-term investment projects.

The Scientific and Technological Association INFOPARK is the largest private voluntary union of software developing companies in the Republic of Belarus.

Infopark unites 69 enterprises and organizations of various patterns of ownership and provides employment for more than 11 000 IT professionals.

Being a fast-developing and socially responsible business, the companies of the Association INFOPARK render assistance to development of Belarusian IT educational system, high-skilled personnel consolidation, conducting inter-branch research and raising competitive abilities of the IT enterprises.

The project activity of Association INFOPARK reflects its priorities and is subjected to its main aim, i.e. consolidation the emerging in the region software engineering business-cluster on the global market (Software Solutions & Services).

INFOPARK develops cooperation with IT-associations and organizations in Russia, Ukraine, Latvia, Lithuania, the Czech Republic and other countries.

CONTENT

INVITED LECTURES

Section 1 – SYNTHESIS, STRUCTURE AND PROPERTIES OF NANOMATERIALS (GRAPHENE, FULLERENES, NANOTUBES, NANOPARTICLES, COMPOSITES ETC.)

Section 2 – APPLICATIONS OF NANOMATERIALS (ELECTRONICS, MECHANICS, BIOLOGY etc.)

Section 3 – MOLECULAR DYNAMICS AND DFT SIMULATION

INVITED LECTURES

POSSIBLE WAYS OF MINI-FULLERENE FORMATION: FROM FOUR TO TWENTY

A. Melker

Department of Mechanics and Control Processes
St. Petersburg State Polytechnic University, Russia

I. INTRODUCTION

It is customary to assume that fullerenes are the carbon molecules having a shape close to a spherical surface which can be composed of regular pentagons combined with regular hexagons. From this it follows that the least fullerene has twenty atoms forming twelve pentagons. We have supposed that this restriction is unnecessary [1]. In other words, we have taken the term "*fullerene*" in a broad sense as any convex shape inscribed into a spherical surface which can be composed of atoms, each atom having *three nearest neighbors*, as in usual fullerenes, whenever discussing hollow carbon clusters. This geometrical approach allowed us to obtain possible forms of the broad-sense fullerenes. To gain a more penetrating insight into their nature, we have also taken into consideration, along with the atomic structure of these spherical molecules, their electronic structure [2]. For this purpose we have developed an enlarged version of the theory by Sidgwick and Powell [3] according to which:
  – Geometry of a molecule is dictated by the arrangement of electron pairs in the valence shell of atoms;
  – Each shared electron pair, forming a covalent bond, can be considered as a point charge;
  – All the electron pairs of a molecule arrange themselves into such configuration which ensures their equal and maximal removing from each other.

Sidgwick–Powell's theory, created in 1940, allowed explaining and predicting stereochemical properties of many simple molecules (more than 1500 [3]). This theory was extended in the twenty-first century and applied to cyclic molecules such as cyclohexane [4] and usual fullerenes [5], which have no a central atom. The all-important result of such extension consists in the following: *the hidden symmetry of special electronic pattern does not coincide with that of atomic one*. However, it is precisely *the electronic pattern that defines the atomic structure*.

The modified approach developed in [4] was applied to the broad-sense fullerenes [1]. Contrary to the previous approaches [3, 4], where atoms and electron pairs had their own spheres, the main innovation in [1] is the additional postulate:
  – Atoms and shared electron pairs, forming covalent bonds, are located *on one and the same sphere*.

It follows herefrom that the geometry of both the electronic structure as well as of the atomic structure of fullerenes can be most conveniently constructed and studied with the help of *spherical geometry*.

Up to now mechanism of fullerene formation is unclear. The irrefutable fact is as follows. If to take one electrode of $_6C^{13}$ graphite and another of ordinary $_6C^{12}$ graphite, the fullerene, formed in an electric arc, has $_6C^{13}$ – and $_6C^{12}$ – atoms arranged on a fullerene surface in random way. It follows herefrom that fullerene assemblage originates from separate atoms (or maybe from C_2 fragments).

In this contribution we used this fact and the approach developed in [1] as the basis for predicting possible ways of broad-sense fullerenes formation. Besides, as in [6], we have used graph theory [7] to represent formation of carbon clusters, their transformation from a cluster to a fullerene, and their final configurations.

II. TETRAHEDRAL FULLERENE C_4

Let us start with a reaction-active single carbon atom. One can envision two ways of forming a cluster of four carbon atoms (Figs. 1a, 1b). Consider the first way which incorporates three stages (Fig.

1a). In the first stage the single atom adds another atom and activates it. In its turn the second atom adds two other atoms, forming a simple branching. The second way consists of two stages (Fig. 1b). Here the reaction-active atom adds at once three atoms which create covalent connected pairs. If the process starts with a reaction-active carbon dimmer (Fig. 1c), we have only two stages. At the first one each dimmer atom adds other atoms; then mutual turning of the covalent bonds formed leads to arranging a tetrahedron. In all the cases the process consists of several stages which can differ, but the final configuration due to folding is one and the same tetrahedron. It can be represented with one of isomorphic graphs having four vertices (Figs. 1d, 1e).

It should be noted that the diagram shown in Fig. 1a is identical with one of the diagram (simple branching) illustrating formation process not only of an athermal tetravacancy under irradiation but also that of a branched polymer during polymerization [6].
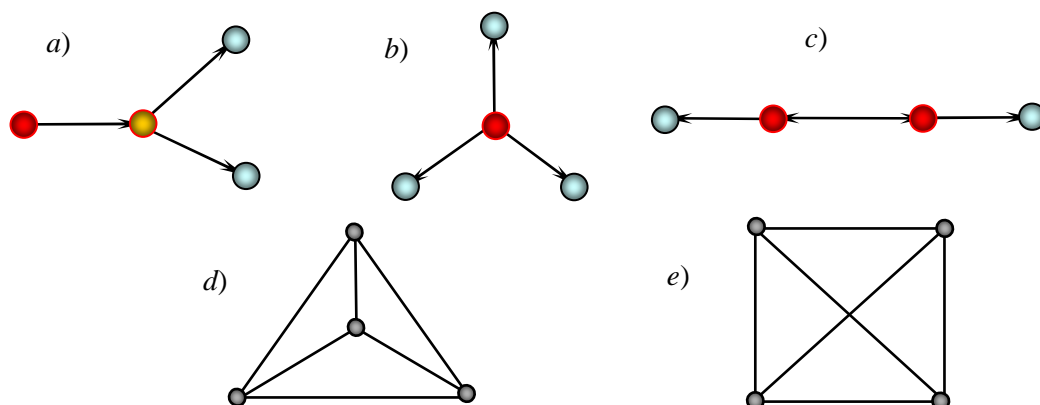
Figure 1 – Different ways of forming a cluster of four carbon atoms (*a*, *b*, *c*) and graph representation of a tetrahedral fullerene in the form of isomorphic graphs (*d*, *e*).

Consider the transform of a carbon cluster into a tetrahedron. According to our postulate, each carbon atom can have, as usual fullerenes, three neighbors who are located with the nucleus atom on one and the same sphere (Fig. 2a). Here the large circles represent carbon atoms; the small ones refer to electron pairs. In other words, we have a cluster with three covalent bonds; the tail atoms having unshared electron pairs which also lie on a sphere. If the growth of this cluster is suppressed, the tail atoms, due to the interaction of their unshared electron pairs (Fig. 2b), create covalent bonds between themselves fashioning a tetrahedron (Fig. 2c). It should be emphasized that in the qualitative theory by Sidgwick and Powell it is supposed that any electron pairs, shared or unshared, can only repel, but not attract. This restriction is a consequence of the assumption that the electron pairs can be considered as point charges. More careful quantitative analysis on the basis of dynamics reveals that it is necessary to take into account eigenvibrations of an electron pair considering the electron pair as a dynamic variable [2].

With this in mind, we have shown that each pair plays the role of an external field with respect to another pair, thus polarizing it. Therefore the electron pair is a dynamic electric dipole rather than a quasi-point electric charge. Such dipole represents itself to be an oscillator, i.e. the system of two opposite point charges which are equal in absolute value; the distance between them is changing in consequence of vibrations near a stable equilibrium position. As a result, there appeared intramolecular van der Waals interaction between the electron pairs. It follows herefrom an essential difference between static charges and dynamic dipoles. The first produce only Coulomb repulsion whereas the second both repulsion and van der Waals attraction. It is just this attraction which leads to producing the tetrahedral fullerene (Fig. 3a), having the electronic structure in the form of an octahedron (Fig. 3b). According to [8] an octahedron is the only stable configuration for six electron pairs.
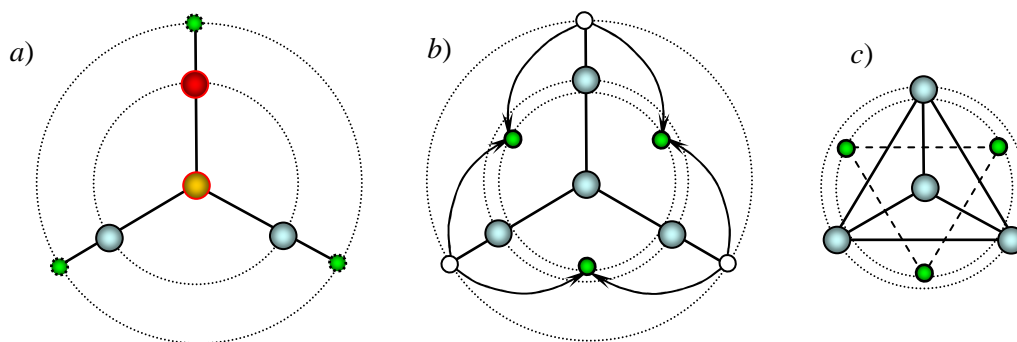
Figure 2 – Top view: (*a*) cluster of four carbon atoms, each tail atom having an unshared electron pair; formation of new covalent bonds (*b*) gives rise to a tetrahedron (*c*). Atomic and electronic parallels are shown by dotted circles. The edge length of the tetrahedron is *a*; the radius of the atomic parallel is $a/\sqrt{3}$; the radius of the electronic parallel is $a/2$.
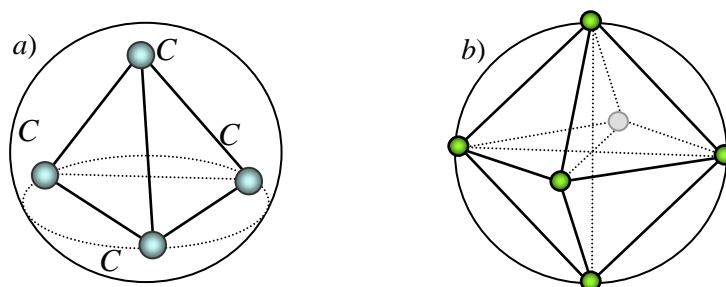
Figure 3 – Carbon tetrahedron inscribed into a sphere (*a*); here any three atoms lie on one and the same parallel; (*b*) shared-electron-pairs octahedron corresponding to (*a*).

III. TRIANGULAR PRISMATIC FULLERENE C_6

The next in size carbon cluster, each atom of it having three nearest neighbors, which can be inscribed into a sphere, is a triangular prism. Similar to the previous procedure for a tetrahedral fullerene, we can envision different ways of forming at first a cluster of six carbon atoms (Figs. 4a through d) and then a triangular-prism fullerene as two graphs having six vertices (Figs. 4e, 4f). It should be noted that these graphs are isomorphic [7].

It should be noted that from a mathematical viewpoint the diagram (a) is identical with one of the diagram (double branching) illustrating formation process not only of an athermal hexavacancy at irradiation but also of a branched polymer at polymerization [6].
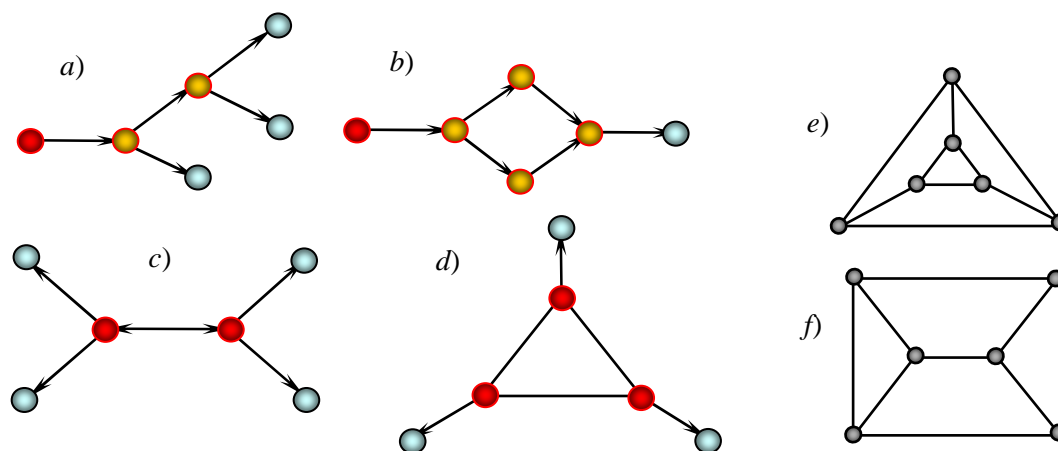
Figure 4 – Different ways of forming a cluster of six carbon atoms (*a*, *b*, *c*, *d*) and graph representation of a triangular-prism fullerene in the form of isomorphic graphs (*e*, *f*)

Due to the attraction of electron pairs, there forms the triangular-prism (Fig. 5a), having the electronic structure in the form, which contains nine point charges with maximum removal from each

other (Fig. 5b). The electronic configuration of this mini-fullerene coincides with that of an ordinary molecule having nine electron pairs in its valence shell [8]. For this reason we will use the terminology accepted in molecular geometry. According to [8] this configuration is named a three-cap trigonal prism.
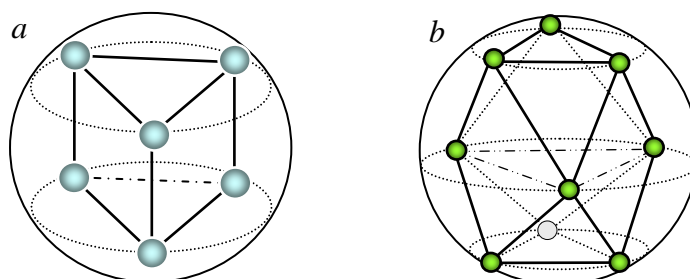
Figure 5 – Carbon triangular prism inscribed into a sphere. Here (*a*) three atoms of two bases lie on one and the same parallel; (*b*) nine shared electron pairs on a sphere surface with maximum removal from each other, so called a three-cap trigonal prism.

Because of the page restriction we limited ourselves by these two examples of mini-fullerene formation; other examples will be given during the workshop.

REFERENCES

[1] A.I. Melker, V. Lonch, Atomic and electronic structure of mini-fullerenes: from four to twenty // *Materials Physics and Mechanics*, **13** (2012) 22-36.
[2] A.I. Melker and M.A. Vorobyeva, Electronic theory of molecule vibrations // *Proc. SPIE*, **6253** (2006) 625305-1–625305-15.
[3] N.V. Sidgwick, H.M. Powell, Bakerian Lecture, Stereochemical types and valency groups // *Proc. Roy. Soc. Series A*, **176** (1940) 153-180.
[4] A.I. Melker and M.A. Krupina, Hidden symmery or why cyclic molecules have so strange forms // *Materials Physics and Mechanics*, **9** (2010) 11-19.
[5] A.I Melker, S.N. Romanov, D.A. Kornilov, Computer simulation of formation of carbon fullerenes // *Materials Physics and Mechanics*, **2** (2000) 42-50.
[6] A.I. Melker and S.N. Romanov, Group representation of the formation probabilities of athermal vacancy clusters in atomic collision cascades // *Physica status solidi b*, **126** (1984) 133-140.
[7] Frank Harary, *Graph Theory* (Addison-Wesley Publishing Co. Reading, 1969).
[8] R.J. Gillespie, *Molecular Geometry* (Van Nostrand Reinhold Co. London, 1972).

SINGLE NV CENTERS IN NANOSTRUCTURED DIAMOND
FOR QUANTUM INFORMATICS AND QUANTUM MAGNETOMETRY

A. Nizovtsev[1], *S. Kilin*[1], *A. Pushkarchuk*[2], *V. Pushkarchuk*[3], *F. Jelezko*[4]

[1] *B.I. Stepanov Institute of Physics NASB, Minsk, Belarus*
[2] *Institute of Physical Organic Chemistry NASB, Minsk, Belarus*
[3] *Belarusian State University of Informatics and Radioelectronics, Minsk, Belarus*
[4] *Institute for quantum optics, Ulm University, Germany*

Abstract – Using density functional theory we have simulated hyperfine interactions (hfi) in the $C_{291}NVH_{172}$ cluster for all possible positions of the ^{13}C atom in the cluster and calculated hfi splittings of the EPR lines for arbitrary $^{14}NV+^{13}C$ spin systems. Applications of the systems for quantum information processing and single-spin quantum magnetometry will also be reviewed.

I. INTRODUCTION

The ability to create, control and measure the coherence in multi-spin systems in solids is crucial for scalable applications of quantum information processing, quantum sensing and metrology. Coupled electron-nuclear spin systems where electrons act as fast processing qubits while nuclei can store quantum information for a long time owing to their exceptional isolation from environment are especially useful for the purposes.

The most successful and promising representative of such systems is the nitrogen-vacancy (NV) color center in diamond [1] whose ground-state electron spin (e-spin) S=1 is coupled to the nuclear spin (n-spin) $I^{(N)}=1$ of its own ^{14}N atom and, potentially, to nearby n-spins $I^{(C)}=1/2$ of isotopic ^{13}C atoms that are distributed randomly in diamond lattice with the 1.1% probability. Hyperfine interactions (*hfi*) in such systems lead directly to a few-qubit gates which can be implemented using a sequence of optical, microwave or radio frequency pulses to initialize, coherently manipulate and readout the electron-nuclear spin system states [2-4]. Initially, it has been done [3] on single NV centers strongly coupled to a ^{13}C n-spin being nearest neighbor of the vacancy. Later [2,4] more distant ^{13}C nuclear spins located in the third coordination sphere have been distinguished in optically detected magnetic resonance (ODMR) spectra and spin echo modulation. Most recently usage of dynamical decoupling methods to suppress background spin noise allows to observe single NV centers coupled to much more distant single ^{13}C nuclear spins and to study them systematically [5-8]. Here, we report on the systematic study of hyperfine interactions between the electronic spin of single NV center and ^{13}C nuclear spins in the NV-hosting H-terminated carbon cluster $C_{291}NVH_{172}$ using computational chemistry simulation.

II. METHODS AND RESULTS

The geometric structure of the cluster was optimized and the spin density distribution was calculated by DFT using the B3LYP1 functional with the MINI/3-21G basis sets. The calculations have been performed for singly negatively charged cluster in the triplet ground state (S=1). We used the PC GAMESS (US) and ORCA software packages to calculate *hfi* matrices for all possible positions of the ^{13}C atom in the cluster. To be general, it has been done in the principle axis system (PAS) of the NV center where the Z axis coincides with the C_{3V} symmetry axis of the center while the X and Y axes are chosen arbitrarily. Evidently, various ^{13}C lattice sites showed different and generally anisotropic interactions with the NV e-spin, leading to different spin properties of various $NV+1^{13}C$ spin systems.

The simulated *hfi* matrices have been used in the standard spin Hamiltonian of an arbitrary $^{14}NV+1^{13}C$ system that took into account i) zero-field fine structure splitting of the ^3A ground-state of the center in a diamond crystal field, ii) *hfi* of the S=1 e-spin of the NV center with I=1 n-spin of the ^{14}N atom of the center, iii) the quadrupole moment Q=1 of the ^{14}N nucleus, iv) *hfi* with the I=1/2 n-spin of a ^{13}C nucleus disposed somewhere in the cluster and v) Zeeman interactions of all three spins with arbitrarily directed external magnetic field. Numerical diagonalization of these spin Hamiltonians

provides 18 eigenenergies and respective 18 eigenstates of all possible $^{14}NV+1$ ^{13}C spin systems in the cluster.

Using this approach we have simulated spectra of optically detected magnetic resonance (ODMR) of $^{14}NV+1$ ^{13}C spin systems and compare them with those experimentally observed in [6]. Typical *hfi* structure of e.g. $m_S=0 \leftrightarrow m_S=-1$ line in the ODMR spectrum of a system in low magnetic field consisted of six lines corresponding to allowed EPR transitions in the system with their frequency differences determined by the *hfi* with the ^{14}N and ^{13}C nuclear spins. From these ODMR spectra one can extracts zero-field splittings Δ_{0i} of e.g. the $m_S=-1$ NV e-spin state resulted from its *hfi* with single ^{13}C n-spin taking specific (i-th) position in diamond lattice with respect to the NV center. If we compare these experimental data with those obtained by spin-Hamiltonian method using simulated *hfi* matrices for all possible $^{14}NV+^{13}C$ system we will be able to address the specific ^{13}C nucleus among other positions.

Simulated values of hfi and spatial characteristics for 121 positions of a ^{13}C n-spin in the $C_{291}NVH_{172}$ cluster are presented in the Table 1. Calculations showed that owing to the C_{3V} symmetry of the NV center there are N_C (=3 or 6) positions of ^{13}C nuclei in the cluster exhibiting very close values of their hfi and spatial characteristics. In the Table 1, we indicate data for 26 sets of such near-equivalent lattice sites (families) which are termed by English alphabet letters A-Z with indication of most important elements A_{ZZ}, $A_{nd} = (A_{XZ}^2 + A_{YZ}^2)^{1/2}$ of hfi matrices, zero-field *hfi* splittings Δ_{0i}, Z coordinates, distances from Z-axis and from N atom of the NV center. All data are averaged over the family members.

TABLE 1 – Simulated *hfi* and spatial characteristics for the "families"
of ^{13}C n-spin in the $C_{291}NVH_{172}$ cluster.

Family	N_C	$\overline{A}_{ZZ}$ (MHz)	$\overline{A}_{nd}$ (MHz)	$\overline{\Delta}_i^{(0)}$ (MHz)	$\overline{Z}$ (Å)	$\overline{r}_{XY}$ (Å)	$\overline{r}_{NC}$ (Å)
A	6	12.451	1.166	12.471	- 0.522	3.937	4.536
B	3	11.386	1.434	11.451	- 2.655	2.972	5.298
C	3	-8.379	0.827	8.437	- 2.109	1.487	4.118
D	6	-6.450	0.931	6.521	- 0.010	2.552	3.089
E	3	4.055	0.826	4.136	-2.643	1.491	4.621
F	6	3.609	0.738	3.682	1.577	2.562	2.566
G	6	2.281	0.240	2.292	0.008	5.166	5.446
H	3	1.884	0.208	1.895	-4.242	2.976	6.673
I	3	-1.386	0.130	1.392	0.005	4.458	4.780
J	6	-1.145	0.328	1.191	-2.110	3.932	5.497
K1	3	-0.886	0.510	1.022	-2.118	2.985	4.871
K2	3	-1.011	0.014	1.012	-0.002	4.460	4.785
L	3	0.980	0.121	0.986	-0.535	2.972	3.737
M	3	0.602	0.557	0.819	2.127	1.460	1.513
N	6	0.725	0.095	0.731	-0.541	6.467	6.855
O1	3	0.673	0.171	0.694	-4.712	4.479	7.847
O2	3	0.655	0.166	0.676	3.707	2.983	3.578
P	6	0.474	0.190	0.510	-2.635	5.355	6.909
Q	6	0.391	0.273	0.477	-2.645	3.953	5.897
R	3	-0.226	0.393	0.453	2.115	2.985	3.009
S	3	0.412	0.060	0.417	-0.511	5.942	6.351
T	3	0.366	0.149	0.395	3.709	1.504	2.485
U	3	0.286	0.225	0.364	1.578	4.481	4.484
V	6	-0.209	0.232	0.312	2.105	3.927	3.945
W	3	-0.200	0.171	0.266	-4.220	1.489	6.135
X	6	0.211	0.152	0.259	-4.768	2.573	6.990
Y	6	-0.228	0.001	0.227	-0.522	5.381	5.834
Z1	3	0.158	0.131	0.205	4.226	3.001	3.903
Z2	3	0.086	0.184	0.203	1.576	4.447	4.447
on-NV-axis	1	0.187	0.001	0.187	-4.734	0.009	6.465

we do not show in the Table 1 largest simulated *hfi* splittings of ~130 MHz for the three sites being NN of the vacancy, as they are well documented in the literature.

We have shown that all simulated data correlate well with available experimental data of works [5-8] which demonstrates that *hfi* parameters simulated for the $C_{291}NVH_{172}$ cluster by DFT in conjunction with spin Hamiltonian method provide good fit to the experimental *hfi* splittings, allowing simultaneously to address possible positions of ^{13}C in diamond lattice. Moreover, we were able to describe well the experimental ODMR spectra shown in [6] for the specific $^{14}NV+^{13}C$ spin system. We also have calculated cosines of angles between Z axis of the NV PAS and z axis of ^{13}C PAS for all possible positions of ^{13}C in the cluster. For a first time we predict the zero-field *hfi* splitting of 187.4 kHz for the nearest ^{13}C atom position lying on the NV axis. These data will be published elsewhere.

REFERENCES

[1] F. Jelezko, J. Wrachtrup, "Quantum information processing in diamond", *J. Phys. Condens. Matter*, vol. 18, pp. S807-S824, 2006.

[2] L. Childress et al. "Coherent dynamics of coupled electron and nuclear spin qubits in diamond," *Science*, vol. 314, pp. 281-285, 2006.

[3] F. Jelezko et al. "Observation of coherent oscillation of a single nuclear spin and realization of a two-qubit conditional quantum gate", *Phys. Rev. Lett.*, vol. 93, p. 130501, 2004.

[4] P. Neumann et al. "Multipartite entanglement among single spins in diamond", *Science*, vol. 320, pp. 1326-1329 (2008).

[5] B. Smeltzer, L. Childress, A. Gali, "^{13}C hyperfine interactions in the nitrogen-vacancy centre in diamond," *New J. Phys.* **13**, 025021 (2011).

[6] A. Dreau et al. "High-resolution spectroscopy of single NV defects coupled with nearby ^{13}C nuclear spins in diamond", *Phys. Rev. B*, vol. 85, p. 134107, 2012.

[7] N. Zhao et al. "Sensing single remote nuclear spins", *Nature Nanotechnology*, vol. **7**, pp. 657-662, 2012.

[8] S. Kolkowitz et al "Sensing distant nuclear spins with a single electron spins," *Phys. Rev. Lett.*, vol. 109, p. 137601 2012.

HIERARCHICAL APPROACH TO NANODESIGN
ROM THE SYSTEM THEORY VIEWPOINT

V. Barkaline

Belarusian National Technical University, *Minsk*, *Belarus*

Abstract – Hierarchy of nanosystems' simulation models are discussed from the viewpoint of the multilevel hierarchical systems' theory by S. Novikava (Aed theory).

I. Introduction

Current scientific and technological progress is usually understood in close links with the development of nanotechnology, the subject of which includes structures, processes and functions based on materials with properties defined on spatial scales 1 – 100 nm. The fundamental difficulty of nanotechnology is the fact that nanostructures are so small that it is very hard to manipulate them precisely, and simultaneously too large for direct application of precise chemical methods such as genetic engineering for their treating. Methods of simulation of them have to be both fast and precise enough for the prediction and optimization of the electronic, atomic and phase structures, functional properties and chemical behaviour of nanomaterials. Modeling of nanomaterials and nanosystems is a sophisticated task due to the fact that properties of nanomaterials are defined by interacted groups of hundreds of atoms and could hardly be computed by *ab initio* quantum mechanics (QM) methods even on supercomputers [1]. Components of nanosystems composed from such atomic groups contain millions of atoms and can be treated by molecular dynamics (MD) methods rather than QM, while the whole nanosystem can contain dozens of billions of atoms and only the finite elements' (FE) continuous approximation can be applied to it. In general system theory it is established [2] that the description of such systems have to be decomposed into interrelated description levels when at every lower level only these properties and variables of the system are calculated which are necessary for modeling it on the upper level, and, on the other hand, the upper level determines modeling tasks and constrains for calculation on the lower level. The full model represents the hierarchy of the decision making according to Mesarovich. Then the hierarchical multilevel system theory (HMST) must be used in nanosystems computing too. This approach generalizes multiscale simulation approach and corresponds to combined traditional "up-to-down" and novel "down-to-up" technologies in nanodesign.

II. S. Novikava's Aed Mathematics and Nanodesign

Current stage of HMST is Aed theory by S.Novikava [3], which has now two main hierarchical symbolic images $^\times\alpha^\lambda$ and $^+\alpha^\lambda$ corresponding to the acts of multiplying (learning) and uniting (design) respectively. They contain the new means of control and connect the strata (directions) of A^λ. Aed strata are: Λ,λ–level (time), Γ,γ–statute (law, connection), P,ρ– act (process), Ω, ω – unit (state) Σ,σ – construction (contents), B, β – new time (arising level), A, α – sway (coordinator). Aed statute A^λ in current level λ is described by its symbol image $^\times\alpha^\lambda$ in following way:

$$A^\lambda \xleftrightarrow[\rho]{\gamma} \left\{ {\beta \atop \omega}{A\atop}{\gamma\atop\sigma}\lambda \right\} \xrightarrow[\rho]{\lambda\xrightarrow{A^\lambda}\beta} \qquad \Lambda^\lambda \xleftrightarrow[\rho]{\gamma} \left\{ {\beta \atop \omega}{\Lambda\atop}{\gamma\atop\sigma}\lambda \right\} \xrightarrow[\rho]{\lambda\xrightarrow{\Lambda^\lambda}\beta} \qquad \Gamma^\lambda \xleftrightarrow[\rho]{\gamma} \left\{ {\beta \atop \omega}{\Gamma\atop\rho}{\gamma\atop\sigma}\lambda \right\} \xrightarrow[\rho]{\lambda\xrightarrow{\Gamma^\lambda}\beta} \qquad P^\lambda \xleftrightarrow[\rho]{\gamma} \left\{ {\beta \atop \omega}{P\atop\rho}{\gamma\atop\sigma}\lambda \right\} \xrightarrow[\rho]{\lambda\xrightarrow{P^\lambda}\beta}$$

$$\Omega^\lambda \xleftrightarrow[\rho]{\gamma} \left\{ {\beta \atop \omega}{\Omega\atop}{\gamma\atop\sigma}\lambda \right\} \xrightarrow[\rho]{\lambda\xrightarrow{\Omega^\lambda}\beta} \qquad \Sigma^\lambda \xleftrightarrow[\rho]{\gamma} \left\{ {\beta \atop \omega}{\Sigma\atop}{\gamma\atop\sigma}\lambda \right\} \xrightarrow[\rho]{\lambda\xrightarrow{\Sigma^\lambda}\beta} \qquad B^\lambda \xleftrightarrow[\rho]{\gamma} \left\{ {\beta \atop \omega}{B\atop}{\gamma\atop\sigma}\lambda \right\} \xrightarrow[\rho]{\lambda\xrightarrow{B^\lambda}\beta} \qquad A^\beta \xleftrightarrow[\rho]{\gamma} \left\{ {? \atop \omega}{A\atop\rho}{\gamma\atop\sigma}\beta \right\} \xrightarrow[\rho]{\beta\xrightarrow{A^\beta}?}$$

In this way all aed strata can renovate its original unit A^λ they have all its signs and abilities. The strata $\Lambda,\Gamma,B,P,\Sigma,\Omega$ are strongly connected both by their original.unit A^λ and by the details of their own constructions (by their new interactions). Thanks to that all aed strata may be renovated when any stratum is changed. The acts of original unit A^λ multiplying and their symbol images uniting lead to

the arising of the new time unit A^β. It contains hazy symbols in its image (they are signed by the symbol ? and they will be defined in time β).

The image $^+\alpha^\lambda$ (Fig.1) allows to see the acts of multiplying & uniting (learning & design), their bases, aims and connections. In Fig 1 A^λ - original state of aed ($A^\lambda \leftrightarrow \omega^\lambda$), A^β - its leading state in time λ; multiplying act $^\times\rho^\lambda$ of original order γ^λ (original statute of A^λ) executes learning process in the units ω^{λ_τ} of construction σ^{λ_τ} which was created in time λ_τ; thanks to that the units ω^{λ_τ} turn into the ordinary units ω_τ^λ in the new construction σ^λ; uniting act $^+\rho^\lambda$ in σ^λ connects the ordinary units ω_τ^λ and creates the new sway $\omega^\beta \leftrightarrow A^\beta$; in the process ρ^λ the image of arising time β^λ has two strata - $^\times\beta^\lambda$ and $^+\beta^\lambda$ which answer to the stages of this process: $^\times\rho^\lambda$ and $^+\rho^\lambda$.

Application of HMST to nanosystems leads to hierarchical structure presented in Table 1. Every level must be split on two sublevels corresponding to classical and quantum descriptions of electromagnetic field.

TABLE 1 – Hierarchical simulation levels of nanosystems

N	Simulation level name. Basic equations	Space and time scales. Elementary unit. Number of atoms.		Values calculated at the level	Comments
6	System level. State space models $\begin{cases} \dot{\vec{x}} = \mathbf{A}\vec{x} + \mathbf{B}\vec{u} \\ \vec{y} = \mathbf{C}\vec{x} + \mathbf{D}\vec{u} \end{cases}$	100 nm - 1 m, 1 ps - 1 year. System unit, subsystem, element of system. 10^{23} atoms/mole		Transition functions, frequency responses, control algorithms, regular and stochastic regimes.	Models used in system theory and automatic control
5	Continuum level. Maxwell's and balance equations, state equations, boundary conditions	500 nm - 1 mm, 1 mcs -100 s. Continuum media element. 10^6- 10^{10} atoms		Electromagnetic, mechanical and thermal behavior of micro- and nanosystems' elements.	Systems of partial differential equations for averaged fields
4	Mesoscopic level. Fluctuations' dynamics on the basis of level V equations with fluctuation sources included	50 nm - 1 mcm, 50 ns -1 ms. Polycrystalline grains, granules, nanoclusters, powders. 10^6- 10^{10} atoms		Electromagnetic, mechanical and thermal behavior of elements, linear response theory, fluctuation-dissipation relations.	Systems of stochastic partial differential equations for fluctuated physical fields
3	Molecular dynamics level. Newton's equations	1 - 500 nm, 1ps - 50 ns	Atomic clusters, macromolecules, multiwall nanotubes. 10^3- 10^8 atoms	viscosity, thermo- and electroconductivity, material constants, phase diagrams, state equations, steady state structures, phase transitions, non-equilibrium processes	Solution of Newton's equations for all atoms in thermostat
	Kinetics level. Liouville's equation	1 nm - 10 mcm, 1 ps - 10 mcs			Probability distribution densities of various order
2	Quantum statistical level. Von Neuman's equation	10 Å–100 nm, 100 fs – 10 ps Crystal unit cell, cluster in adjacent medium 10 – 1000 atoms		Inter-cluster interaction, cluster surfaces, stochastic energy spectrum	Statistic operator or density matrix
1	Quantum mechanical level. Schrödinger's equation	0.1-20 Å, 1-1000 fs. Molecule, isolated cluster. 10 – 100 atoms		Interatomic interaction potentials, electronic subsystem distribution density	*ab initio* models, molecular orbitals' theory, DFT
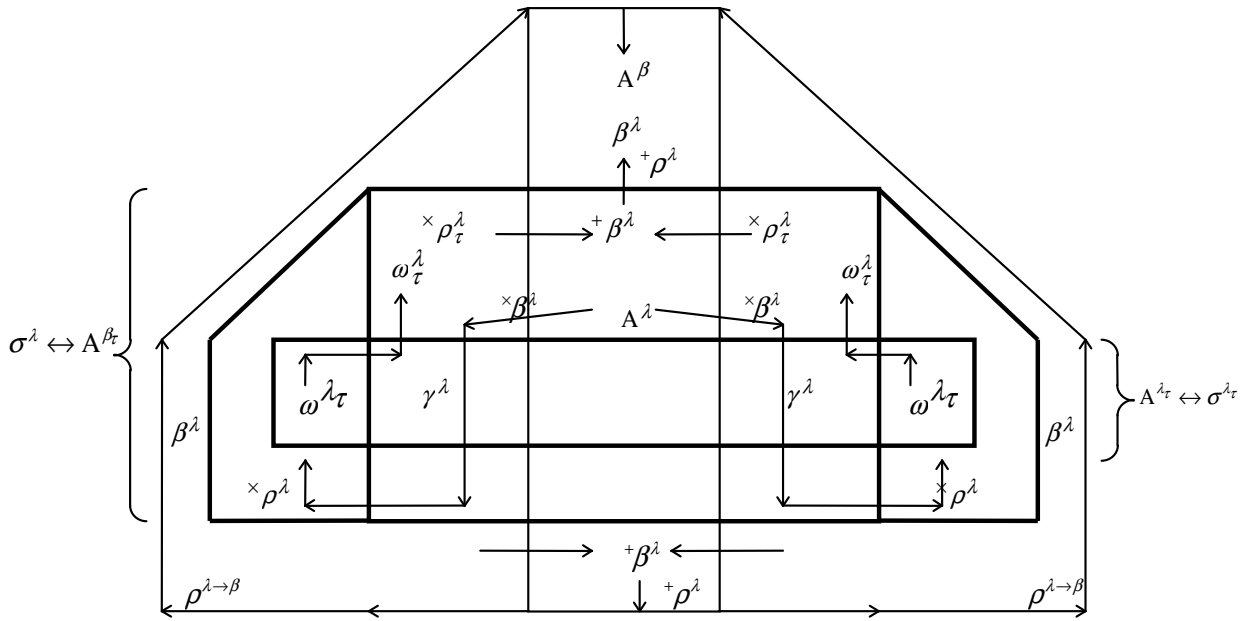
Figure 1 – Symbolic image of aed

III. CONCLUSION

In this paper the we discuss the hierarchical approach to nanodesign and present its formal realization on the basis of the aed theory. Description of nanosystems have to be decomposed into interrelated levels when at every lower level only these properties and variables of the system are calculated which are necessary for modeling it on the upper level, and, on the other hand, the upper level determines modeling tasks and constrains for calculation on the lower level.

REFERENCES

[1] H. Primas, *Chemistry, Quantum mechanics and Reductionism*. Berlin, Heidelberg, New York: Springer-Verlag, 1981.
[2] M. Mesarovich, D.Mako, Y. Takahara, *Theory of hierarchical multilevel systems*. New York and London : Academic press, 1970.
[3] S. Novikava, K. Miatluk, S. Ganchrova, A. Ivahow, A. Zhybul, A. Danichaw, P. Buka, V. Siargeichyk, A. Demyanenka, "Theory in Hierarchical Knowledge Networks," *Studies in Informatics and Control*, vol.6, N 1, pp.75-85, 1997.

SECTION 1. SYNTHESIS, STRUCTURE AND PROPERTIES OF NANOMATERIALS (GRAPHENE, FULLERENES, NANOTUBES, NANOPARTICLES, COMPOSITES ETC.)

OPTICAL CHARACTERIZATION OF 3D DISPERSE SYSTEMS WITH NANO- AND MICRO- PARTICLES: LIGHT SCATTERING MATRIX ELEMENTS

A. Bezrukova, O. Vlasova

St. Petersburg State Polytechnical University, Russia

Abstract – The multiparametric analysis of simultaneous optical data for nano- and micro- particle systems (ensembles, dispersions) by presentation of system characteristics as N-dimensional optical parameter vectors can help to elucidate the nature of particles, the process of particle interactions, the particle share in mixtures of particles and so on. In this paper the application of light scattering matrix elements as vector parameters is shown on the example of influenza virus and colibacillus dispersions. The presentation as N-dimensional optical parameter vectors can serve as innovative research platform for sensing of different particle interfaces including biological ones.

I. INTRODUCTION

Ensembles of nano- and / or micro- particles can be considered as three-dimensional ($3D$) disperse systems (DS) with particles as a disperse phase in dispersive medium [1]. Multiparametric analysis of optical data for $3D$ DS can provide further progress for detailed characterization and control of $3D$ DS with particles of different nature (including biological ones). Taking into account optical theory [1-4] and results of experiments [5-20] can help to elaborate sensing elements for on-line control of $3D$ DS state. Our research [5-19] has investigated different $3D$ DS with nano- and / or micro- particles (with diameter less than 10 micrometers) and has included: a) simultaneous measurements of $3D$ DS by different compatible nondestructive optical methods such as refractometry, absorbance, fluorescence, light scattering (integral and differential, static and dynamic, unpolarized and polarized), and b) solution of inverse optical problem by different methods and technologies of data interpretation by information-statistical theory [21]. The experience suggests that the set of optical parameters of so-called "second class" [11-13, 16-18] is unique for each $3D$ DS [13]. In another words each $3D$ DS can be characterized by N-dimensional vector (ND vector) in N-dimensional space of second class optical parameters [13]. ND vectors can reflect in "unobvious" form all peculiarities of $3D$ DS: nature (constituent substances); form, inner and surface structure of particles; distributions of particle size, number, mass, refractive index, etc.; possibilities to aggregation, destruction or interaction with another particles, and so on.

The light scattering matrix elements [2-4] being "second class" parameters by definition (obtained by processing of measured values, dimensionless, mainly independent on the concentration of particles) are very perspective for multiparametric analysis of $3D$ DS. In this paper the application of light scattering matrix elements as ND vector parameters (alone and in complex with second class parameters from other optical methods) is shown on the example of such biological $3D$ DS as colibacillus and influenza virus dispersions.

II. MATERIALS AND METHODS

The form of influenza virus particle can be approximated as a homogeneous sphere, but in some cases, the bilayered sphere approximation can be useful. Colibacillus bacterial cells (Escherichia coli, E. coli, colibacillus rods) can be approximated as a homogeneous equivalent volume sphere or as prolate ellipsoids of rotation. In our research the influenza virus strain A1 (H1N1) dispersions with mean diameter of particles ~100 nm and dispersions of colibacillus with equivalent volume sphere

mean diameter of cells ~0,6 μm (strain K-802) and ~1,3 μm (strain AB 1157) were used. Due to the great sensitivity of biological objects to the surrounding medium and conditions, it is necessary to use simultaneous measurements for object comparison and to take into account all details of experiments (pH, content of nutrition medium, temperature, etc.).

There is the description of main optical methods used for 3D DS characterization (*refractometry*, *fluorescence*, *absorbency*, *integral light scattering*, *differential static* and *dynamic light scattering*) in the previous articles [17, 19]. For the measurements of light scattering matrix elements laser (wavelength 633 nm) self-made installation with detector angles from 60 up to 120 degrees, polarizes and retardation element was used.

III. RESULTS AND DISCUSSION

The Stokes vector **F** – describes the complete polarization properties of a beam of light. The effect of scattering on a beam of light can be represented by the Mueller matrix – *M* (with 16 dimensionless elements – S_{ij}), that transforms the Stokes vector for the incident light – $\mathbf{F}_{inc}$, to the Stokes vector representing the scattered light - $\mathbf{F}_{sc}$ [2,3]:

$$\mathbf{F}_{sc} = M \cdot \mathbf{F}_{inc}, \tag{1}$$

where: $\mathbf{F}_{inc}$ - the Stokes vector for the incident light, $\mathbf{F}_{sc}$ – the Stokes vector for the scattered light, *M* – 16-element Mueller matrix:

$$M = \begin{bmatrix} S_{11} & S_{12} & S_{13} & S_{14} \\ S_{21} & S_{22} & S_{23} & S_{24} \\ S_{31} & S_{32} & S_{33} & S_{34} \\ S_{41} & S_{42} & S_{43} & S_{44} \end{bmatrix}$$

S_{ij} are functions of the scattering angle and contain all information about the elastic light scattering properties of a particle system at a given wavelength [2-4]. The scattering matrix is determined by the size, shape, symmetry, internal structure and optical properties of the particles in system. In general, all 16 dimensionless elements of the scattering matrix for nonspherical particles can be nonzero and depend on the orientation of the scattering plane. Angular dependence of scattered light depends on the polarization of incident light.

The 3D DS state characterization as *ND* vector can be implemented in the *N*-dimensional space of matrix element parameters alone or in the complex with other optical parameters. The first case can be demonstrated on the S_{11} and S_{34} matrix elements data for colibacillus in classical work [20]. The published experimental data about S_{34}/S_{11} angular dependences for two E. coli strains (strain B/r [20, Fig. 5a] and strain K-12 [20, Fig. 5b]) were processing according our *ND*-vector approach: the eight informative parameters was found for dispersion state differentiation in about ten orders and in sign.
In our research, the 3D DS state differentiation by *ND* vector of matrix element parameters was used in complex with other optical parameters in order to construct optimal scheme for dispersion on-line control. As example S_{11} data was combined with integral light scattering data for differentiation of two colibacillus strains (K-802 and AB1157) in about one order.

In other example the S_{11} and S_{12} data was combined with integral and static light scattering data for differentiation of influenza virus (strain A1-H1N1) and colibacillus (strain K-802) dispersions. Optical data were presented as the 12*D*, 4*D* and in complex 16*D* vectors. Taking into account the angular dependences of S_{11} (parameters denoted with subscription S) and S_{12} (parameters denoted with subscription P) it is possible to form *ND* vectors $\mathbf{P_S}$ {P_{S1}, P_{S2},… P_{SN}} and $\mathbf{P_P}$ {P_{P1}, P_{P2},… P_{PN}} correspondingly (in this example N = 6). The four informative second class optical parameters from integral and differential static light scattering - 4*D* vectors [13], were combined with $\mathbf{P_S}$ and $\mathbf{P_P}$. The complex 16*D* vectors allow differing the state of viral and bacterial dispersions in about seven orders.

IV. CONCLUSION

Optical parameter vector can reflect in "unobvious" form many peculiarities of the system state. $3D$ DS can be characterized and compared one with another by means of ND vectors. The vectors can also reflect the changes in the state of mixtures. Due to the fusion of various optical data and by the information statistical theory, it is possible to find the set of informative parameters and to solve the inverse physical problem on the presence of the component of interest in mixtures without any regularization. In this case, the polymodality of particle size distribution is not the obstacle. The number of parameters can be enlarged if to consider angular and wavelength dependences of optical data. ND vector approach can be considered as "integral" for the study of whole system as unity with the minimum interference. The presentation of $3D$ DS as ND vectors can serve as the innovative research platform for sensing of particle interfaces. It also can demonstrate an awareness of the potential applications for bio- and nano- technology, medicine, industry and for the protection of environment.

REFERENCES

[1] V.J. Klenin, Thermodynamics of Systems Containing Flexible Chain Polymers. Elsevier, 1999.

[2] C.F.Bohren, D.R.Huffman, Absorption and Scattering of Light by Small Particles .Wiley, New York, 1983.

[3] Light Scattering by Nonspherical Particles. Theory, Measurements and Applications, ed. by M.I. Mishchenko, J.W. Hovenier, L.D. Travis, AP, 1999, 690 pp.

[4] F.Ya.Sid'ko, V.N.Lopatin, L.E.Paramonov, Polarization Characteristics of Biological Particles Dispersions. Siberian branch of Nauka publishing house, Novosibirisk, 1990, in Russian.

[5] A. G. Bezrukova //Progr. Colloid Polym. Sci. **93** (1993) 186.

[6] A.G. Bezrukova // Proc. SPIE **3107** (1997) 298.

[7] A. G. Bezrukova //Mater. Res. Soc. Proc. **711** (2002) FF7.9.

[8] O.L. Vlasova and A.G. Bezrukova // Proc. SPIE **5127** (2003) 154.

[9] A.G. Bezrukova // European Cells and Materials Journal **6,** Supplement 1 (2003) 88.

[10] A.G. Bezrukova // Proc. SPIE **5400** (2004) 189.

[11] A.G. Bezrukova // Proc. SPIE **5831** (2005) 112.

[12] A.G. Bezrukova // CD: 2006 Spring National Meeting Conference Proceedings, New York: AIChE, 2006.

[13] A.G. Bezrukova // Proc. SPIE **6253** (2006) 62530C-1

[14] A. Bezrukova, M. Lubomska, P. Magri, M. Rogalski // Proc. SPIE **6597** (2007) 65970M.

[15] A. Bezrukova, M. Lubomska, M. Rogalski // Rev. Adv. Mater. Sci. **20** (2009) 70.

[16] A. G. Bezrukova, Proc. SPIE, **7377** (2009) 73770B-1.

[17] A.G. Bezrukova, O.L. Vlasova // Materials Physics & Mechanics **9** (2010) 167.

[18] A.G. Bezrukova // European Cells and Materials Journal **20,** Supplement 3 (2010) 19.

[19] A.G. Bezrukova, O.L. Vlasova // Materials Physics & Mechanics **13** (2012) 162.

[20] B.V. Bronk, S. D. Druger, J. Czege, W.P. Van De Merwe // Biophysical Journal **69** (1995) 1170.

[21] F.M. Goltsman, Physical Experiment and Statistical Conclusions (Leningrad University Publishing House, Leningrad, 1982), - in Russian.

THE DEPENDENCE OF GALLIUM NITRIDE NANOWIRES PROPERTIES ON SYNTHESIS PRESSURE AND TEMPERATURE

M. Danilyuk[1], A. Messanvi[2]

[1]*Belarusian State University of Informatics and Radioelectronics, Minsk, Belarus*
[2]*Institute National des Sciences Appliquées de Rennes, France*

Abstract – The main task of the investigation was to perform the synthesis of gallium nitride nanowires using a low pressure chemical vapor deposition system. The nanowires were grown via a catalyst-assisted reaction based on the vapor-liquid-solid mechanism. The influences of catalyst, temperature and pressure on the growth of gallium nitride nanowires were explored. Optimal results were obtained at a temperature of $750^{o}C$ and a pressure of 400 to 500 mTorr.

I. INTRODUCTION

Among the various kind of investigated nanowire systems, Gallium Nitride (GaN) nanowires are of particular interest because this III-V semiconductor has already showed interesting properties in bulk form. The growth parameter to be varied was the temperature. The following experiments were performed with nickel as the catalyst as successful growth of nanowires was obtained with this metal. Temperature is a very important parameter to tune in nanowire growth as changes of a few tens of degrees have been reported to produce nanowires with very different morphologies. GaN is well-known for its resistance to temperature, strain and high electric fields. As a result it is a material of choice for high power/high temperature applications. In addition to, the optical properties of GaN are useful for optoelectronic device operating at ultraviolet and blue wavelengths [1].

II. EXPERIMENTAL RESULTS

In our case, four temperatures were tested: 700°C, 750°C, 800°C, and 850°C. SEM images below show typical nanowire morphology obtained for 750°C, 800°C temperature (Figure 1). By lowering the temperature, it was expected to avoid the formation of the $NiSi_2$ compound and reach the temperature region where NiSi start to aggregate. The trial at 800°C resulted in successful growth of a high density of nanowires on the Si substrates. Although some nanowires grew straight with a smooth surface most of them exhibited a rough surface. The nanowire body could be seen as a succession of cones stacked all along the main axis.
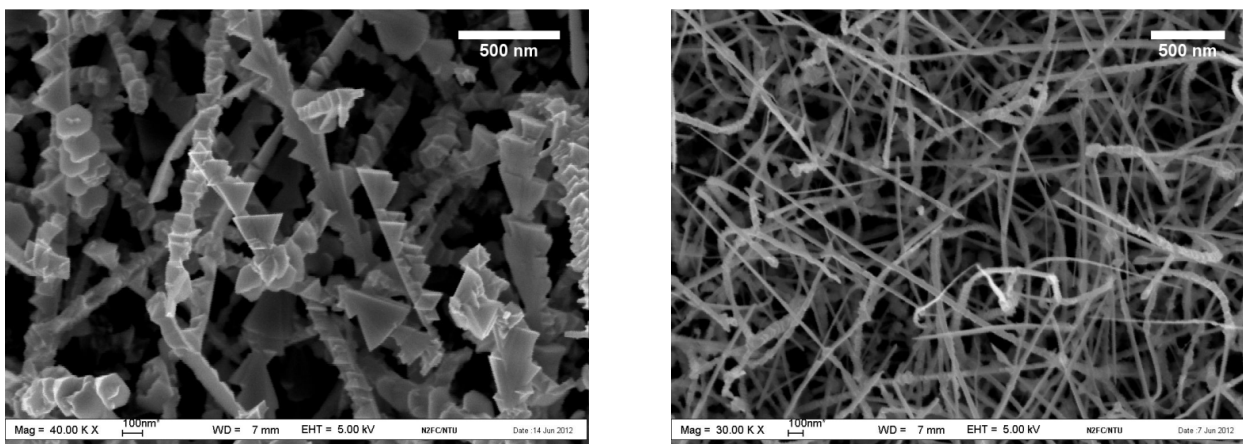
Figure 1. SEM images of nanowires obtained at 800°C, 750°C temperatures.

The photoluminescence (PL) spectra of the GaN nanowires were obtained under excitation at 260 nm [2]. Figure 2 shows the PL spectrum obtained for GaN nanowires at different temperatures. For each temperature, the spectrum is characterized by two main peaks: an intense and broad peak which corresponds to the near band-edge emission and a much weaker peak centered around 300 nm. Influence of the growth temperature on the PL spectrum of the GaN nanowires is clearly visible. As the temperature increases from 700°C to 800°C, the emission peak becomes broader: peak fitting rises

from 65 nm at 700°C to 200 nm at 800°C. Moreover, at 800°C, the near band-edge emission seems to result from the overlapping of multiple peaks centered at 407 nm, 425 nm and 440 nm. A red-shift of the emission peak can also be observed with increasing temperatures from 390 nm at 700°C to 425 nm at 800°C. The near-band-edge peak normally located around 360 nm for GaN material is shifted towards red wavelengths for our GaN nanowires by more than 30 nm. Previous comparisons between luminescence from GaN bulk and nanowires have shown that emission from nanowires is usually broader and red-shifted due to strain as well as surface and impurity states. Therefore, the decrease in peak broadening seems to indicate that the structures grown at lower temperatures exhibit a lower density of defects than those grown at higher temperatures. Correlation between the previous observations and the nanowire morphology shows that the stacked-cone nanowires grown at 800°C have a quite broad luminescent peak whereas the very thin nanowires grown at 700°C exhibit a narrower emission peak; however the peak intensity in the latter case is reduced by one third.
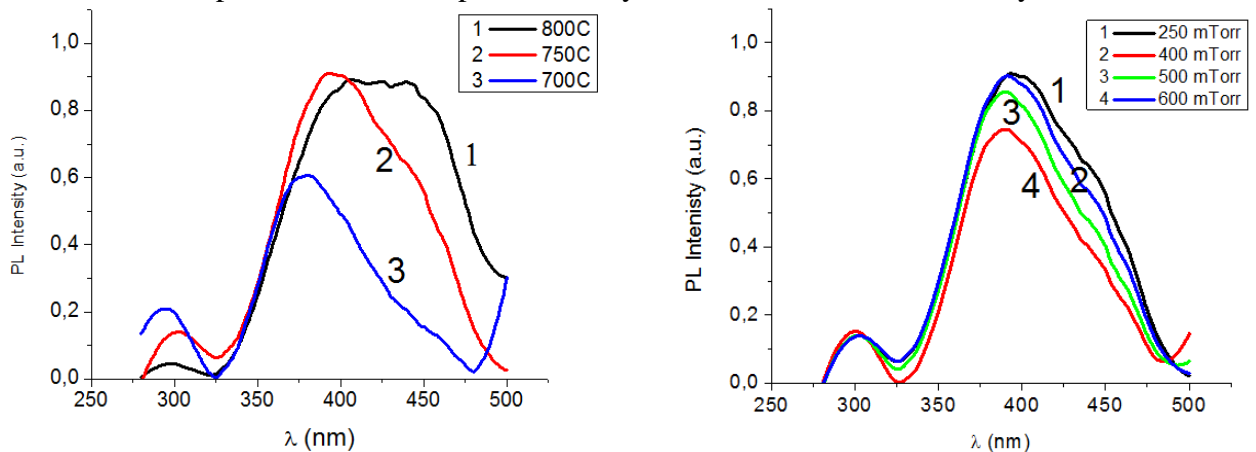
Figure 2. PL spectra of GaN nanowires synthesized at different temperatures and different pressures.

For nanowires grown under various pressure conditions, the PL spectra exhibit a more consistent shape. This is in agreement with the observed morphology of the wires. The PL spectra present a near band-edge emission around 390-395 nm and a UV-emission centered at 300 nm. We can observe an increase in the peak intensity and width when the pressure increases from 400 mTorr to 600 mTorr: the tops of the fitted peaks goes from 115 nm at 400 mTorr to 158 nm at 600 mTorr. The broadest emissions are obtained at 250 mTorr and 600 mTorr. This seems to confirm that rough surface nanowires induce peak broadening as they incorporate a higher amount of defects than smooth and thin nanowires.

III. CONCLUSION

These results indicate that the optical quality of 1-D GaN nanostructures can be improved by controlling their dimensions and their diameter in particular. In our case, the lowest growth temperatures (750°C-700°C) at which thin nanowires have been produced gave the best optical results. PL spectra at these temperatures exhibited narrower emission peak and a reduced red-shift. However it can be observed that the decrease in peak broadening is also associated with a reduction in peak intensity. The conclusions drawn from these photoluminescence measurements are expected to be confirmed with further experiments including electrical measurements and Raman spectroscopy. At these pressures, nanowires with stacked cone features were observed.

REFERENCES

[1] M. Q. He, P. Z. Zhou, S. N. Mohammad, G. L. Harris, J. B. Halpern, R. Jacobs, W. L. Sarney, and L. Salamanca-Riba. Growth of GaN nanowires by direct reaction of Ga with NH3.// Journal of Crystal Growth. - 2001. vol. 231. – p. 357-365.
[2] B. Monemar. III-V nitrides – important future electronic materials. // Journal of Materials Science-Materials in Electronics. – 1999. vol. 10. – p. 227-254.

A CONTINUAL APPROACH TO VAN DER WAALS INTERACTIONS IN CARBON NANOTUBE BASED SYSTEMS

Y. Belahurau, V. Barkaline

Belarusian National Technical University, Minsk, Belarus

Abstract – Ordered arrays of carbon nanotubes (CNT) are promising elements of nanoelectromechanical systems based on transformation of electromagnetic fields into mechanical motion. Simulation of these phenomena accounting various nonlinear interactions can be realized on the basis of macroelectrodynamics of moving media, theory of elasticity and van der Waals interactions' phenomenological theory. The balance equations of mass, momentum, angular momentum and energy as well as entropy inequality describing interacting continua of the mass, electric charge and internal spin are presented. To include van der Waals forces the additional terms are introduced into these equations which transform the system into indegro-differential one. It is shown that integral terms can be neglected if the gap between tubes is greater than CNT outer diameter. The occurrence of multiple resonant vibrations of ordered CNT arrays is characteristic of them. Solving the system numerically the essential influence of van der Waals forces on CNT array resonant frequencies was proved.

I. INTRODUCTION

Dynamic mechanical behaviors of CNTs have been studied widely in recent years. Ordered arrays of carbon nanotubes (CNT) are prospect materials of nanoelectromechanical systems based on transformation of electromagnetic fields to the mechanical motion [1]. Such arrays may be used as sensitive elements of different sensors with acoustoelectronic output signal [2]. Electromechanical coupling theory for such arrays is based on combined solution of kinetic equation for electrons, Maxwell's equations and the equations of lattice dynamics [3]. But there can be also a phenomenological approach based on macroscopic electrodynamics and continuum mechanics. Correct simulation of electromagnetic and mechanical behavior of such system requires accounting of all interactions in the system as precise as possible. An approach [4] can be used here. In this article we tried to take into account van der Waals's interactions in CNT arrays and analyze the influence of these interactions on the mechanical resonance dynamics of CNT arrays.

II. FUNDAMENTAL OF THE PROBLEM

Development and creation of the continual approach which can take into account van der Walls' (vdW') interactions is the main aim of the article. VdW' interactions is described with the through the Lennard–Jones (LJ) potential [5].

$$U(\vec{r}) = -\frac{C_6}{\vec{r}^6} + \frac{r_0^6 \cdot C_6}{2 \cdot \vec{r}^{12}}, \tag{1}$$

where $r_0 = 3.88$ A, $c_6 = 2.5 \cdot 10^{-77}$ J·m^6.

Volume force density acting on tube t_1 of array is represented as:

$$\vec{F}(\vec{r}) = 6 \cdot C_6 \cdot r_0^{-7} \cdot \frac{\vec{r}}{r_0} \cdot \left(\frac{r_0}{\vec{r}}\right)^8 \cdot \left(\left(\frac{r_0}{r}\right)^6 - 1\right). \tag{2}$$

Modelling interaction of nanotubes {10, 10}, length is 100 A, outer diameter is 13.56 A, internal diameter 3.354 A, density is 2260 kg/m^3, atom concentration $n = 2{,}7587 \cdot 10^{29}$ m^{-3} have been performed for studying van der Waals' interactions influence on resonance frequencies of CNT arrays. Elasticity modulus of CNT has been calculated with a molecular dynamics approach (force field is MM+): $c_{11} = c_{12} = 44{,}6 \cdot 10^{10}$ Pa, $c_{12} = 14{,}2 \cdot 10^{10}$ Pa, $c_{13} = c_{23} = 13{,}9 \cdot 10^{10}$ Pa, $c_{33} = 119 \cdot 10^{10}$ Pa, $c_{44} = c_{55} =$

22,6·10^{10} Pa, c_{66}=14,9·10^{10} Pa. Minimal distance between nanotubes is 3.4 A, 6 A, 10 A. In figure 1 the tubes are demonstrated with using finite element mesh.
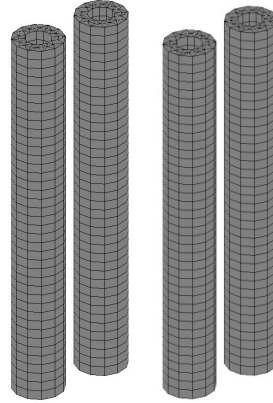
Figure 1 – Nanotubes with using finite element mesh

III. VAN DER WAALS' INTERACTIONS' INFLUENCE ON CNT ARRAY EIGENFREQUENCIES

In figure 2 the results of modeling of CNT static displacement in consequence of van der Waals' interactions are presented.

a)   b)   c)
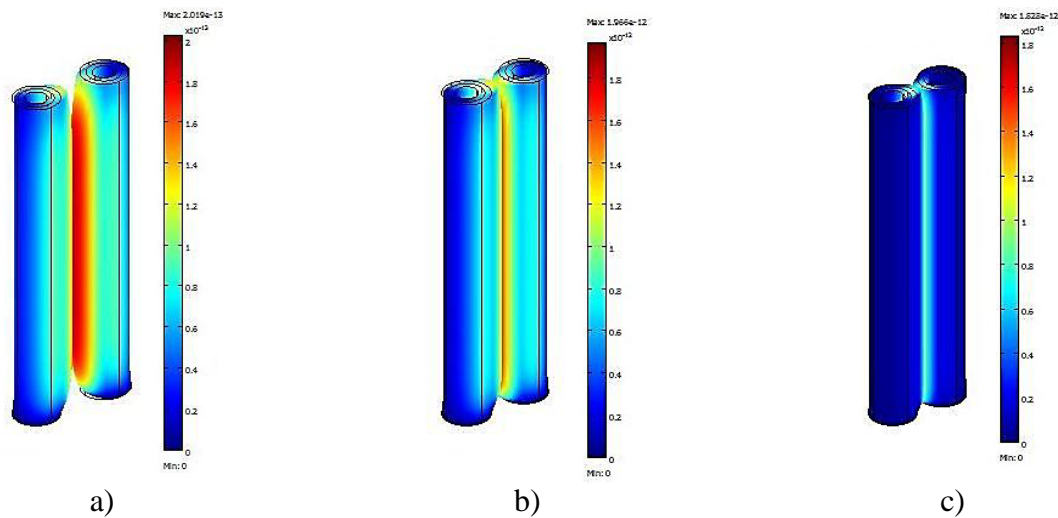
Figure 2 – CNT static displacement as consequence of van der Walls' interactions:
a) distance between CNT is 10 A; б) 6 A: в) 3,4 A

Eigenfrequencies have been calculated for the nanotubes which have been deformed in consequence of van der Waals' interactions. The results are presented in table 1.

TABLE 1 – The CNT array resonance frequencies dependence on distance between nanotubes

Mode shape	Frequencies, GHz			
	Distance between the nanotubes			
	∞	10 A	6A	3.4 A
The 1st bend sagittal on the right tube	43,6112	41,39366	8,538689	16,02657
The 1st bend sagittal on the left tube	43,6112	41,3937	8,544155	16,02649
The 1st bend normal on the right tube	44,4347	41,66737	11,7175	21,07665
The 1st bend normal on the left tube	44,4347	41,66789	11,7232	21,19131
The 1st inflating on the right tube	213,9189	205,8242	58,15274	59,22345
The 1st inflating on the left tube	213,9189	205,8243	58,15945	59,24583
The 2^{d} bend sagittal on the right tube	227,6754	217,2999	84,75225	87,56229
The 2^{d} bend sagittal on the left tube	227,6754	217,301	84,75846	87,58248
The 2^{d} bend normal on the right tube	234,8002	236,6432	112,2834	116,2563
The 2^{d} bend normal on the left tube	234,8002	236,644	112,3166	116,6587

IV. CONCLUSION

Modeling the dynamics of CNT arrays taking into account nonlinear effects can be performed with the help of continuous electrodynamics of moving bodies, the elasticity theory and van der Waals' interactions' theory. Accounting of van der Waals' interactions transforms a set of balance equations to an integro-differential one. If distance between nanotubes in an array is more than tube outer diameter the integral terms may be neglected. Influence of van der Waals' forces is considerable if distance between nanotubes in the array is 3–10 A.

REFERENCES

[1] V. Barkaline, I. Abramov, E. Belogurov, A. Chashynski, V. Labunov, A. Pletezhov and Y. Shukevich, Nonlinear Phenomena in Complex Systems 15, 23 (2012).

[2] V. Barkaline and A. Chashynski, in Chemical Sensors: Comprehensive Sensor Technologies, V. 7, DOI: 10.5643/9781606503171/ch7.

[3] V. M. Kontorovich, Physics Uspekhi 142, 265 (1984).

[4] J. Mozhen. Electromagnetic continuum mechanics. M: Mir, 1991. 560 p.

[5] Lennard-Jones, J.E., 1931. Cohesion. Proceedings of the Physical Society 43, 461–482.

STRUCTURAL AND MAGNETIC PROPERTIES
OF MULTIWALL CARBON NANOTUBE ARRAYS
WITH INCORPORATED IRON-PHASE NANOPARTICLES

A. Prudnikava[1], *A. Danilyuk*[1], *K. Yanushkevich*[2], *J. Fedotova*[3],
I. Komissarov[1], *S. Prischepa*[1], *F. Le Normand*[4], *F. Antoni*[4]
[1]*Belarusian State University of Informatics and Radioelectronics, Minsk, Belarus*
[2]*SSPA "Material Science Center of NASB", Minsk, Belarus*
[3]*NC PHEP Belarusian State University, Minsk, Belarus*
[4]*Laboratoire ICube – DESSP, Strasbourg, France*

Abstract – We have performed an experimental study of the structure, composition and magnetic properties of carbon nanotube (CNT) arrays at different catalyst source concentrations during their synthesis. Floating catalyst chemical vapor deposition was chosen for the synthesis of CNT arrays as a low-cost, simple and effective technique. Various concentrations of ferrocene/xylene solution used as a feedstock for CNT growth allowed obtaining arrays of aligned multi-wall CNTs on Si/SiO_2 substrates with different percentage content, shape and aspect ratio of catalyst inclusions being incorporated in the channels and between the shells of CNTs. In this way the nanoparticles are mostly isolated from interaction with each other, and protected from oxidation in the air atmosphere. The structure and composition of the obtained material was investigated by scanning and transmission electron microscpies, Raman, Mössbauer spectroscopies, and X-ray diffraction. Magnetic properties of CNT arrays were studied by SQUID magnetometer in parallel and perpendicular to the substrate directions at various temperatures (2-380 K). Our results show that magnetic properties of CNT-iron phases can be easily varied depending only on the initially used catalyst source concentration for CNTs synthesis.

I. INTRODUCTION

The interest of reserchers to exploring carbon nanotubes (CNTs) properties haven't subsided since their discovery. The range of their possible applications is very broad, spreading from nanoelectronics to civil engineering. Vertically aligned CNTs filled with magnetic nanoparticles are very promising as a building blocks for many nanoelectronic devices, such as nanothermometers [1], sensors for scanning force microscopy [2], ferromagnetic nanocontainers for biomedical applications [3], high density magnetic storage media [4]. Among various technological methods, floating catalyst chemical vapor deposition (CVD) is one of the most promising, since it allows creating CNT arrays over the large surface areas in controllable manner, and introducing the magnetic particles into CNTs *in situ* during their synthesis.

In this work we used three concentrations of ferrocene/xylene solution, $C_F = 0.5\%$, 1% and 10%, as a feedstock for CNT synthesis. The temperature in the reaction zone during synthesis was 1150 K, and the growth duration was 30 s. As a result, the vertically aligned CNT arrays of 50–100 µm height were obtained. In Fig. 1 the scanning (a,b) and transmission (c) electron microscopy (SEM/TEM) images of CNT arrays synthesized on Si substrate at $C_F = 10\%$ are shown. In TEM image (Fig. 1c), the elongated catalyst nanoparticle in the CNT channel is shown, and a smaller size nanoparticle is indicated by an arrow.

In our earlier study by Mössbauer spectroscopy and X-ray diffraction revealed, that these catalyst nanoparticles represent Fe_3C phase mostly [5].

II. RESULTS

Magnetic properties of the samples were studied by measuring the zero filed cooled (ZFC) and field cooled (FC) magnetizations at magnetic field of $H = 75$ Oe applied either parallel (//) or perpendicular (⊥) to the CNT axis, as a function of temperature. In Figs. 2a and b the ZFC-FC magnetization curves for the samples synthesized with $C_F = 10\%$ and $C_F = 0.5\%$ are shown, correspondingly. For both samples the ZFC-FC curves reveal the typical features of an ensemble of ferromagnetic particles with different interaction forces between them, which, in turn, depend on their concentration [6].
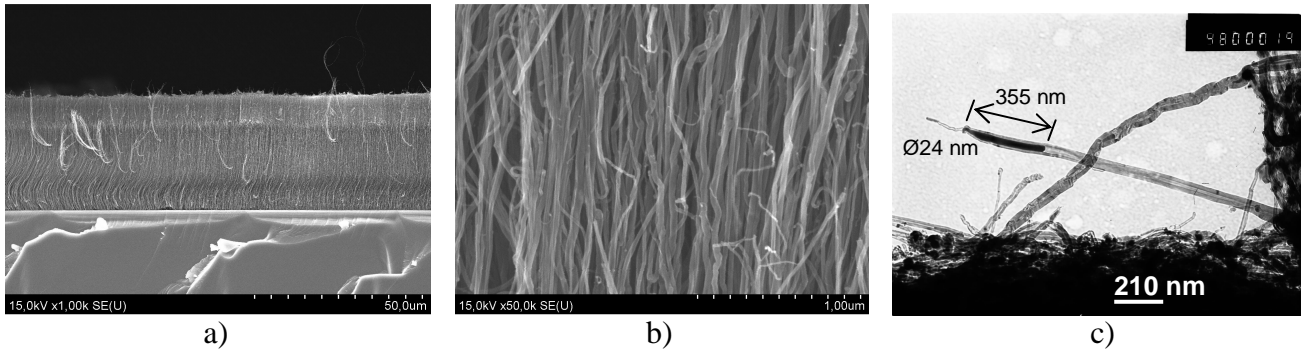
Figure 1 – SEM (a,b) and TEM (c) images of aligned CNT arrays for $C_F = 10\%$.

In Fig. 2a, it is clearly seen that the curves only coincide at the highest measured temperature (300K for the parallel and 350K for the perpendicular orientation). Therefore, the blocking temperature (T_B) is above these values. The behavior of the ZCF curve for $C_F = 10\%$ is identical for both parallel and perpendicular field orientations, and its increase with temperature indicates the strong dipolar coupling between particles. The behavior of the FC curve, on the contrary, depends on the magnetic field orientation. For parallel orientation, a horizontal FC curve indicates strong demagnetizing effect, while for the perpendicular orientation FC curve decreases with temperature. This behavior indicates strong coupling of nanoparticles along the CNT axis (mainly situated inside CNT) and less coupling between particles belonging to different CNT. It is reasonable to associate the observed effect with the influence of CNTs on the magnetic coupling in different directions.

In Fig. 2b, the behavior of ZFC and FC curves is identical for both orientations which is explained by much lower concentration of nanoparticles in the $C_F = 10\%$ sample.
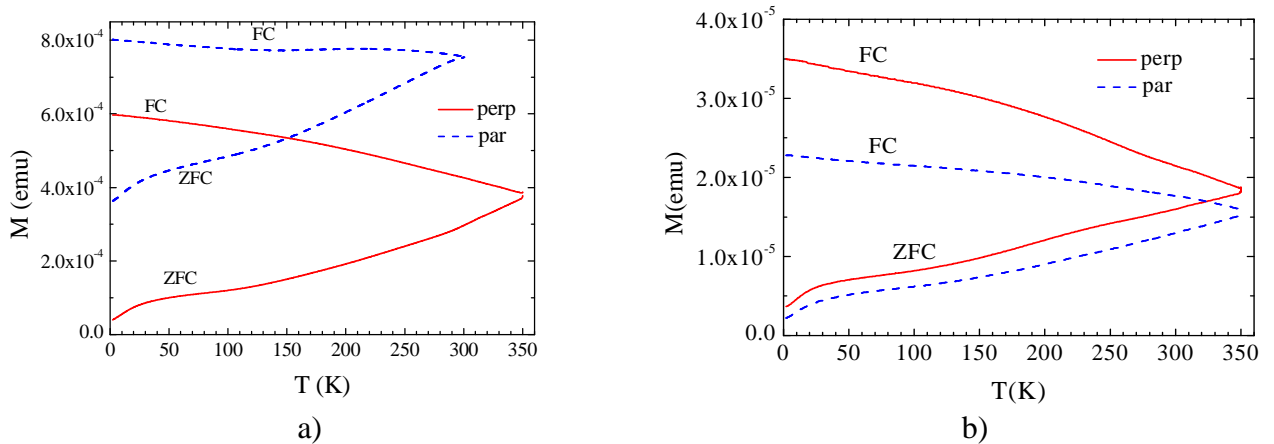
Figure 2 – ZFC-FC curves as a function of temperature for perpendicular (solid lines) and parallel (dashed lines) orientation of the magnetic field of 75 Oe: (a) $C_F = 10\%$; (b) $C_F = 0.5\%$.

Next, magnetic hysteresis loops, $M(H)$, were measured using a Superconducting Quantum Interference Device (SQUID) magnetometer The magnetic field was varied in the range $-8T\ldots+8T$ and was also applied both in parallel and perpendicular to the CNT axis directions.

The $M(H)$ curves recorded for the $C_F = 10\%$ sample at 2K and different orientations of the magnetic field, are presented in Fig. 3a. Both curves are very similar to each other what corresponds to the almost isotropic behavior. In Fig. 3b the squareness (M_{rem}/M_{sat}) versus C_F at different temperatures and H_c versus C_F at 300K (in the inset) are plotted. Analysis of these data indicates that for $C_F = 10\%$ the squareness at 300K becomes much lower than for the $C_F = 1\%$ sample, while at other temperatures it almost does not change between $C_F = 1\%$ and 10%; and for $C_F = 0.5\%$ it is always the smallest. This indicates that the sample synthesized at $C_F = 0.5\%$ is more isotropic and consist of small scattered non-interacting nanoparticles, which is in agreement with the results of ZFC-FC. The decrease of squareness as temperature goes down could be caused by thermal fluctuations. The coercive field value extracted from $M(H)$ curves measured at room temperature appeared to increase with C_F.

a)   b)

Figure 3 – (a) $M(H)$ curves measured at T=2 K for CNT arrays obtained at C_F=10%.
Magnetic field was applied in parallel (filled squares) and perpendicular (hollow squares)
to CNT axis. (b) Squareness vs. C_F at different temperatures. Inset: Coercivity vs. C_F at T = 300K.
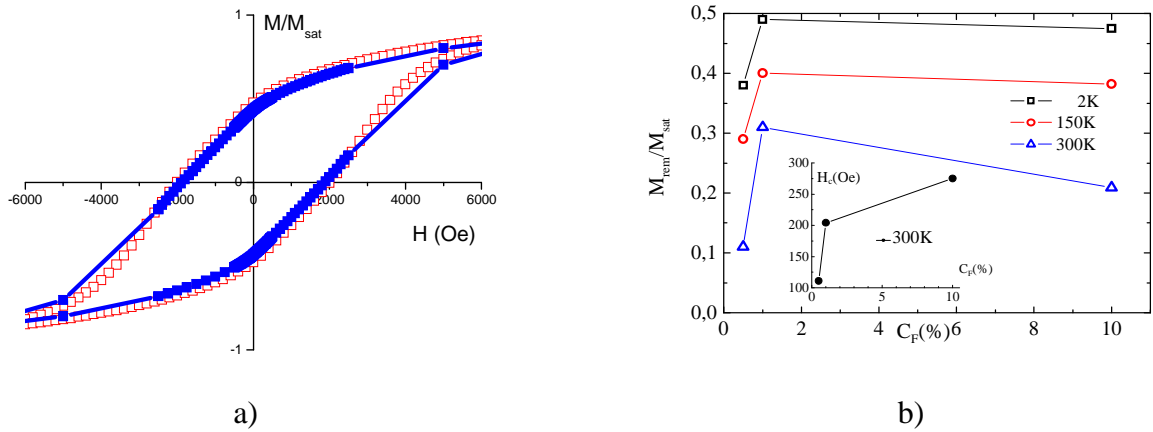Data refer to the perpendicular magnetic field.

III. CONCLUSIONS

In conclusion, the magnetic properties of CNT array with the iron phases nanoparticles obtained by the floating catalyst CVD have been studied. The main ferromagnetic phases were determined (Fe_3C). The overall content of magnetic phase, as well as the particle size can be easily controlled by changing C_F during synthesis. All the hysteresis loops measured on different samples were symmetric. Both the squareness and coercivity dependences on the C_F indicates the smallest inter particle interactions for the C_F = 0.5% sample with the lowest nanoparticles content and diameters.

REFERENCES

[1] Y. H. Gao, and Y. Bando, "Carbon nanothermometer containing gallium," *Nature*, 415(6872) 599, 2002.

[2] A. Winkler, T. Mühl, S. Menzel, et al. "Magnetic force microscopy sensors using iron-filled carbon nanotubes," *J. Appl. Phys.*; 99(10), pp.104905-1-5, 2006.

[3] I. Mönch, A. Leonhardt, A. Meye, et al. "Synthesis and characteristics of Fe-filled multi-walled carbon nanotubes for biomedical applications," J. *Phys.*: *Conf. Ser.*; pp. 61820, 2007.

[4] X.X. Zhang, G.H. Wen, S. Huang, et al. "Magnetic properties of Fe nanoparticles trapped at the tips of the aligned carbon nanotubes," *J. Magn. Magn. Mater.*, 231(1) pp. L9-L12, 2001.

[5] V.A. Labunov, B.G. Shulitski, E.L. Prudnikava, K.I. Yanushkevich, "Structure, composition and magnetic properties of carbon nanotubes doped by Fe during the growth process," *J. Phys.*: *Conf. Ser.* 100, pp. 052095, 2008

[6] J.L. Dormann, D. Fiorani, E. Tronc, "Magnetic relaxation in fine-particle systems," *Adv. Chem. Phys.*,98, pp. 283-494, 1997.

A PROBABLE MECHANISM OF FORMATION
OF DETONATION NANODIAMONDS

V. Dolmatov, K. Rudometkin

Special Construction-Technological Bureau «Technolog», St. Petersburg, Russia

Abstract – In the given work we suggest a new mechanism of formation of nanodiamond crystallites during detonation synthesis. The basis of process is formation of nanodiamond nuclei – ionized adamantane molecules from a radical-like dimer C_2 in the plasma of a chemical reaction zone and further growth of the crystallites due to multiple attack of a growing nanodiamond particle by the dimer C_2.

A theory of the resulting in formation of detonation diamond particles (DND) has a discussion type up to now. Analysis of own and other authors' results on blasting of hydrogen-free benzotrifuroxane (BTF) and alloy of TNT/RDX composition (~50/50) allows to approach an understanding the mechanism of formation of DND step-by-step.

Decomposition of explosive molecules provides rather high concentration of «free» carbon in the time limited ($0,5 \cdot 10^{-6}$ sec) and volume limited chemical reaction zone (its extension – tens of micron). Density of the medium («plasma») is ~2,3 g/cm^3.

Bond breakage in TNT-molecule is accompanied by separation of a methyl-group to give an active methyl radical and, partially, nitro-group; by fragmentation of a benzene ring in the «plasma» of chemical peak to form radicals C_2, C, C_3, CN, CH_x, respective ions and hydrogen (Fig.1). Bond breakage in RDX-molecule goes along C-N-bonds to give also C_2, C, CN. Formation of C_2 is possible from C-radical as in RDX there are no C-C-bonds.
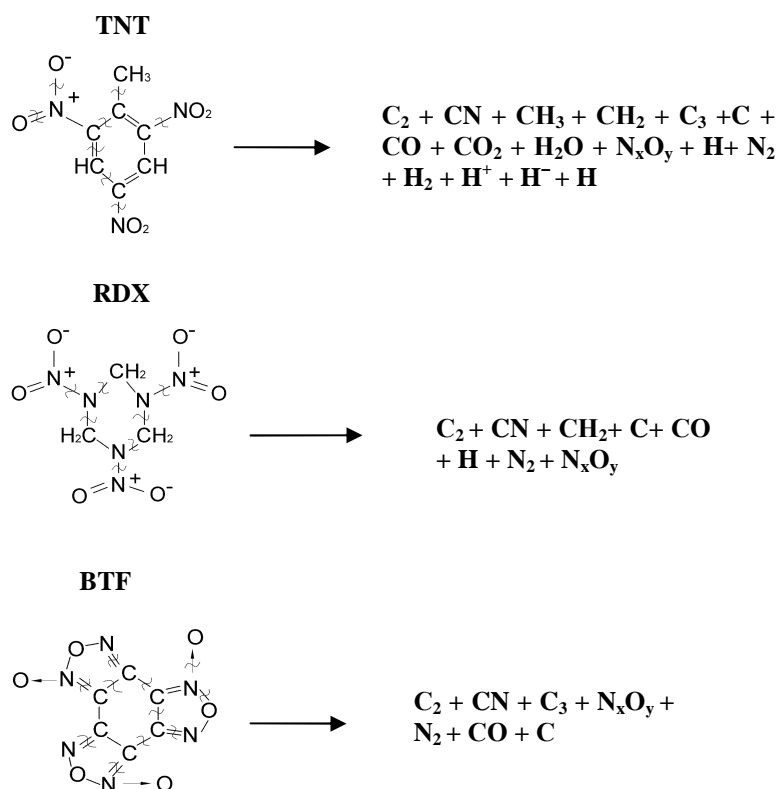
Figure 1 – A supposed disintegration of explosive molecules in the chemical
reaction zone. DND are formed from ~95 wt.% carbon of TNT and ~5 wt.% carbon
of RDX at detonation of TNT-RDX mixture

Decomposition of hydrogen-free BTF proceeds to yield C_2, C_3, CN, N_xO_y, CO.
Formation of primary fragments of the future nanodiamonds begins from the middle to the end of chemical reaction zone (to the Chapman-Jouguet plane) from carbon radicals. At that cyclohexane (more energy-profitable), not benzene ring is formed. Some drops of liquid carbon formed by liquid-

drop coalescence mechanism are amorphized at the first stage of expansion of gaseous detonation products.

A primary «block» is most likely a radical C_2 interring into chemical interaction with the same particles to form cyclohexane or at once adamantane molecules. Possible formation of adamantine in the chemical peak zone was first noted in [1]. Nitrogen gets to a DND-crystallite in the result of C-N-radical bonding.

An adamantane molecule consists of three cyclohexane fragments being in conformation «armchair». Spatial arrangement of carbon atoms in the adamantane molecule replicates arrangement of atoms in the diamond crystal lattice. An adamantane molecule has high symmetry and thermostability.

Growth of a DND-particle goes on the diffusion mechanism through chemical reactions proceedings on their surface at adsorption of free carbon and/or hydrocarbon radicals. During of diamond particle growing its surface is constantly covered with these radicals.

Growth of a DND-particle is stopped because of action of two factors: 1) defect accumulation of the structure when growing the particle and discontinuation of transition of sp^2–hybridized carbon into sp^3– hybridized «diamond» carbon; 2) depletion of carbon radicals.

So, in authors' opinion, one of the probable mechanisms of formation of detonation nanodiamond is possible enough: decomposition of explosives in the chemical reaction zone into radicals $C_2^{\bullet}$, formation of cyclohexane from $C_2^{\bullet}$ which is then isomerized into adamantane as a result of catalytic action of ionized aluminium; adamantane is a diamond-like nucleus of the future DND-particle. Further growth of nanodiamond arises from interaction with carbon radicals.

REFERENCES

1. Tolochko B.P., Titov V.M., Chernyshev A.P., Ten K.A., Pruuel E.R., Zhogin P.I., Zubkov P.I., Lyakhov N.Z., Lukyanchikov L.A., and Sheromov M.A. Diamond and Related Materials (2007), 16, No 12, P. 2014-2017.

RADIOACTIVE NANODIAMONDS

V. Dolmatov[1], E. Gorbunov[2], K. Rudometkin[1]
[1]Special Construction-Technological Bureau «Technolog», St. Petersburg, Russia
[2] Leningrad AES, t. Sosnoviy bor, Russia

Abstract *– In the given work a possibility of obtaining radioactive nanodiamonds was shown. The possibility is stipulated by not production of radioactive isotopes of carbon but by obtaining of radionuclides from non-removable, basically, metal-containing impurities during irradiation in an industrial nuclear reactor.*

Purpose of the present work is obtaining the radioactive nanodiamonds (R-ND) necessary for diagnostics of their allocation in a living organism (medicine), in polymer chemistry (additional polymer cross-linking, in different composites).

As carbon in diamond is practically impossible to transform into radioactive one having an acceptable half-life [1], then to give radioactivity to nanodiamonds (ND) we have tried to create radioactive zones in ND by transformation of non-removable metal-containing impurities into radionuclides.

Detonation nanodiamonds (DND) contain from ~0,05 to 2,5 wt.% metal-containing impurities, static synthesis ND (ND-ASM) contain also up to 2,5 wt. % [2].

Ampoules with DND-powder were irradiated in an industrial reactor of the 4th energetic block of AES, t.Sosnoviy bor, Russia in a special cooling channel.

Nanodiamonds were placed into glass ampoules and bombarded by neutrons in an industrial nuclear reactor with neutron fluence of $1\text{-}2 \cdot 10^{19}$ cm^{-2}. Average power in the immediate surroundings of an irradiating channel was 2,35 MW.

The obtained R-ND have radioactivity with a dose rate of γ-radiation no more than 180,0 µSv/h and a dose rate of γ+β-radiation no more than 720,0 µSv/h.

TABLE 1 – A dose rate of radiation

Diamond kind and its producer	Incombustible impurities, wt. %	A dose rate of γ-radiation, µSv/h (average)	% of γ-radiation of sum γ+β–radiation	A dose rate of γ+β–radiation, µSv/h (average)
19 days storage after radiation termination				
DND, FGUP «SCTB Technolog» (Russia)	0,07	13,68	43	31,86
DND, JSC «ALIT» (Ukraine)	0,34	14,22	38	37,08
DND, produced by Prof. E.Osawa (Japan)	0,79	124,2	30	410,4
ND-ASM (0,1/0), company «SAKID» (Russia)	0,85	160,2	35	459,0
117 days storage after radiation termination				
DND, FGUP «SCTB Technolog» (Russia)	0,07	3,24	72	4,50
DND, JSC «ALIT» (Ukraine)	0,34	4,68	76,5	6,12
DND, produced by Prof. E.Osawa (Japan)	0,79	30,24	64,6	40,68
ND-ASM (0,1/0), company «SAKID» (Russia)	0,85	32,4	54	60,12
227 days storage after radiation termination				
DND, FGUP «SCTB Technolog» (Russia)	0,07	0,61	70,8	0,86
DND, JSC «ALIT» (Ukraine)	0,34	1,22	73,0	1,66
DND, produced by Prof. E.Osawa (Japan)	0,79	7,74	74,1	10,44
ND-ASM (0,1/0), company «SAKID» (Russia)	0,85	11,20	64,8	17,28

Spectroscopic study of ampoules with DND-powders (production of "Elektrokhimpribor") on the 13th day after two-day irradiation showed that there is Cr-51 (basic radionuclide), Hf-181 (detected with high confidence), and - Sb-122, Sb-124, Zr-95 (detected with 50% probability).

An source of formation of a Cr-51- radionuclide is a Cr-50-isotope (content of 4,35 % in elemental Chrome); for Hf-181-radionuclide – a stable Hf-180-isotope (content of 35,10 % in elemental Hafnium, being a chemical analogue of Titanium); as well the rest of chemical impurities - Iron, Titanium, Aluminium can form long-lived radionuclide such as Fe-59, Sc-46, Co-60.

Date for samples R-DND and R-ND-ASM are presented in Table 1.

Arising radioactivity of DND and ND-ASM after irradiation by neutrons can be related to radionuclides formed from Na, Ca, Ti, Fe, Al, W, V, Cu.

Radioactive ND can turn out an convenient instrument for studying their behaviour in different objects and composites.

REFERENCES

[1] Pat. No 2203068, Russian Federation. *Biologically active ultradispersed detonation synthesis diamonds*/ V.Yu.Dolmatov, prior. 12.04.2001, publ. 27.04.2003, Bul. No 12, 2003.
[2] V.Yu.Dolmatov. *Detonation nanodiamonds*. SPb: Publ.house NPO "Professional", 2011, 534 p.

NOVEL CARBON NANOSTRUCTURES: MOLECULAR AND COVALENT BOUND GRAPHENE-FULLERENE CRYSTALS

A. Artyukh, L. Chernozatonskii
Institute of biochemical physics, Moscow, Russia

***Abstract** –* Different models based on graphene and fullerens were proposed. Such structures can be obtained from material that was previously synthesized via external influence.

I. INTRODUCTION

Various graphene-fullerene compounds have been synthesized before [1-4].They are differ from each other by the presence of a covalent bond and the number of graphene layers. In all these works the properties of structure almost were not investigated.

II. SIMULATION METHOD

The mechanical properties of the studied structures were investigated by classical molecular dynamics (MD) method using GULP package [5]. The interaction between carbon atoms was described by Brenner many-body potential [6] which accurately describes the binding energies and elastic properties of wide range of carbon structures [7]. The conjugated gradient method was used for the atomic structure relaxation. For the behaviour investigation of the composite MD simulation method was applied by system at 240, 280 and 500 K during 10 ps with time step of 0.1 fs.

III. COMPOSITE STRUCTURE

As the fullerene monolayer was obtained lying on graphene [4]. We were investigated such model with two different fullerene C_{60} interposition: hexagonal (Fig. 1 a, c) and orthorhombic (Fig. 1 b, d) on graphene surface. The calculation cell is red.
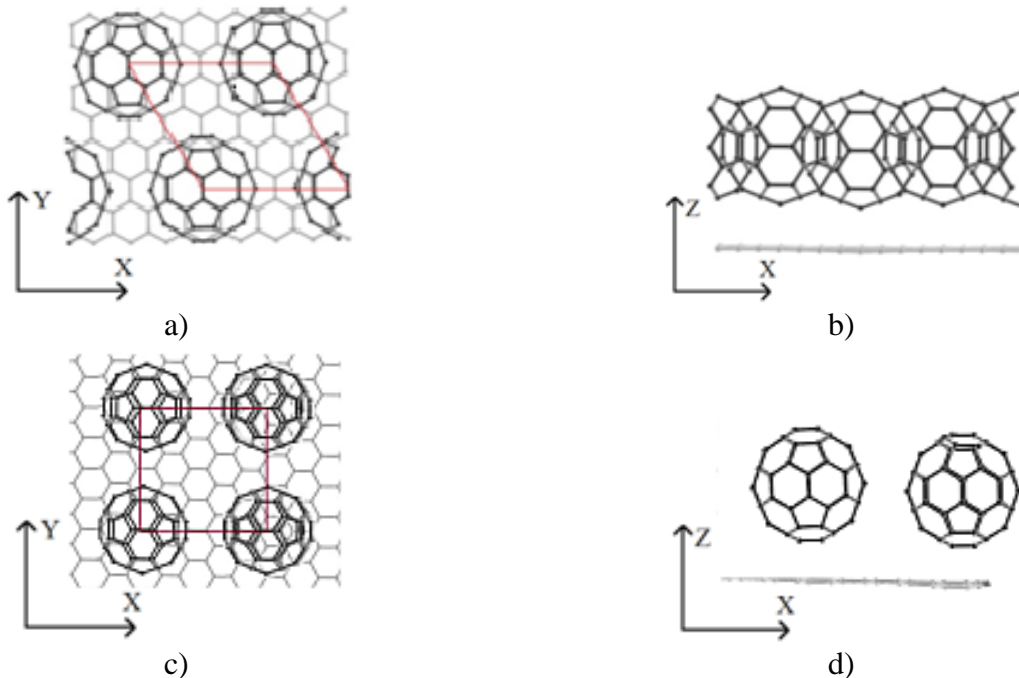

Figure 1 – Models of fullerene location: a, c – hexagonal, b, d – orthorhombic.

The binding energy was calculated for these structures using next formula:

$$\Delta E_f = (E_s - E_G - NE_f) / N,$$

where E_s- calculation cell energy, E_G – graphene energy, N – the number of fullerenes in calculation cell and E_f – energy of one fullerene.

For hexagonal case binding energy is equalled to -0.88 eV/C_{60}, for orthorhombic - 0.67 eV/C_{60}. It's mean that the composite formation from individual component is energy favourable. The thermal stability was investigated at 240, 280 and 500 K. Observed behavior is similar for fullerite crystal. With decreasing temperature (T <260 K) rotation of fullerene molecules stops. Structure is stable under 500 K.

It is well known that fullerenes is polymerized via [2+2] cycloaddition under temperature, pressure or UV effect [8]. That's why it was interesting to consider the fullerene polymer on graphene substrate and fullerene attached to graphene. The fullerene attaching to graphene is changing binding energy for hexagonal structure up to -11.90 eV/C_{60}, for orthorhombic up to – 11.70 eV/C_{60}.
Sheme of step-by-step connection was investigated for fullerene attached to graphene (Fig.2). On first step there was one pair bond between two fullerene molecules, on second step - two pairs, on third - three pairs, on last - the infinite chain of bonded fullerenes. With number of bond increasing the binding energy is growing. The polymerized state is more energy favorable. Thus we can propose a 3D crystal that is fully polymerized.
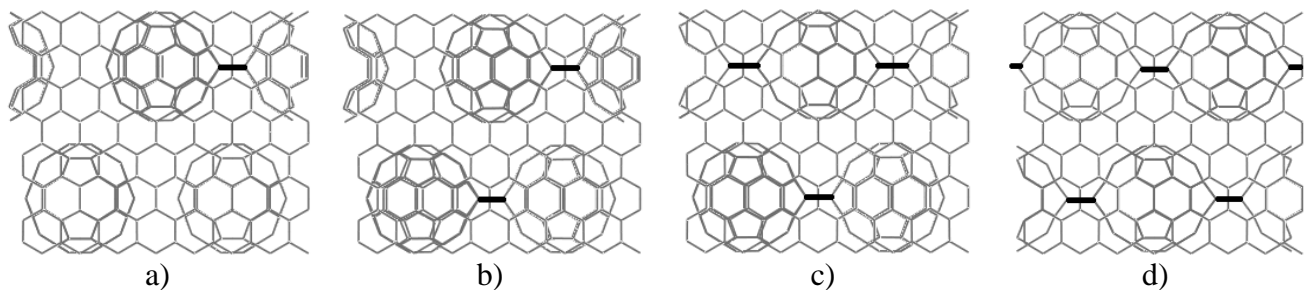

a)   b)   c)   d)

Figure 2 – Scheme of step-by-step connection.

Young's moduli of a 3D structure were calculated using next formula:

$$Y = \frac{F \cdot L}{S \cdot \Delta L},$$

where $F = 2\frac{\partial E}{\partial L}$ – is the force acted on structure.

Here E is the strain energy, L is the structure length and S is the cross-section area of structure. The calculated Young's modulus for XYZ axis are equalled to 0.17, 0.16 и 0.03 TPa. For comparison, Young's module of C_{60} deposited on silicon surface is 0.01 TPa.

IV. CONCLUSION

The new model of polymerized graphene-fullerene structure was considered. Such composite probably can be obtained from compounds [1-4] via exposure that fullerene polymerization promote. The 3D crystal is a stable material with high value of Young's modulus.

REFERENCES

[1] A. Hashimoto et al. / Diamond & Related Materials 18 (2009) 388–391
[2] Ishikawa, Journal of Nanomaterials, 2010, 13, 2010
[3] Zhang, J. Mater. Chem., 2011, 21, 5386–5391
[4] J. Cho, J. Smerdon, L. Gao, Ö.Süzer, J.R. Guest, N.P. Guisinger, Nano Letters 12,3018-3024,2012
[5] J.D. Gale and A.L. Rohl, Mol. Simul., 29, 291 (2003).
[6] Brenner, D. W., 1990, Phys. Rev. B, 42, 9458 (1990).
[7] Petukhov A.V. et.al, phys. stat. sol. (a), 181, 109 (2000).
[8] Fullerene polymers and fullerene polymer composites, eds. P. C. Eklund, A. M. Rao, Springer, Berlin, 2000.

DIMENSIONAL BOUNDARY BETWEEN THE NANO- AND VOLUME STATUS

V. Liopo, *A. Nikitin*, *V. Struk*, *Yu. Tarasevich*
Grodno State University, *Belarus*

Absteract – There is measured border between nano- and macrostate of substance. This fact is explained with the Debye model for the distribution of the frequencies of phonons in crystals. If the size of crystal such that a phonon with a wave-length bigger than the Debye's wave-length can not propagate, it acquires the properties of a substance different from the macroscopic properties of the crystal.

I. INTRODUCTION

When considering the atomic processes in solids often use the classical notions of condensed matter physics. An example is the description of the elementary act of diffusion, the calculation of the specific heat at temperatures close to normal, the calculation of the coefficient of elasticity, etc. The physical properties of the particles when their reduced dimensions remain unchanged until a certain value L_0. For particle sizes smaller than L_0, acquires the properties of a substance different from those of macroscopic size. The curves of the "property-size" for different properties have looks similar to the dependence of the ratio of Young's modulus of iron with grains sizes in the nano- range size to Young's modulus of iron with an ordinary grain size depending on the grain size [1].

II. THE TEMPERATURE EQUIVALENT OF THE PARTICLE SIZE.

To determine the boundary between the nano- and volume status we use a model of continuous Debye phonon spectrum [2]. The Debye frequency related to the energy, momentum, wavelength, and Debye temperature:

$$E_D = \hbar\omega_D; P_D = \hbar\omega_D / u; \lambda_D = 2\pi u / \omega_D; \theta = \hbar\omega_D$$

u- speed of propagation of phonons.

The Debye's temperature (θ) is the temperature bound between classical and quantum approximations. If $T > \theta$ then physical phenomena are described by classic physics otherwise it must take quantum methods. Side by side with Debye's energy $(E_D = k\theta)$ it is proposed to use Debye's momentum $\left(P_D = (2E_D m_e)^{1/2}\right)$ for electrons in the particles. Mechanical displacement of the nucleus leads to excitation of an electron and transfers it to the level exceeding on the main level with the value of the phonon energy. The mass in determining the Debye's momentum is taken equal to the mass of the electron.

Let L_0 is a size bound when mechanism of physical processes changes. If $L > L_0$ the size of particle does not exert an influence to mechanism of physical processes. When $L < L_0$ then the properties of particle different from ones in the bulk objects and the sizes of particles influence to their properties. For calculation of L_0 it must take the uncertainty relation $P_D L_0 = h$. Hence it follows

$$L_0 = h(2m_e k\theta)^{-1/2};$$

h – Plank constant, *k* –Boltzmann constant, *m* – mass of electron.

The L_n are maximum value for nan sizes and are different for matters. F. e. for diamond $L_n = 5nm \left(\theta = 1850K\right)$ but for lead $L_n = 24nm \left(\theta = 95K\right)$.

III. CONCLUSION

Currently, despite the intensive development of a number of industries who consider themselves to nanotechnology, the theory cannot explain the phenomenon of nanoparticles. There are serious objections against the very expressions that have the prefix "nano". If the experimental results obtained when the dispersion and heating (cooling) give the same result in the determination of physical properties, we can introduce the temperature equivalent particle size. Therefore the determination of the true place of nanoscale objects and systems in real industrial production is a multifaceted problem whose solution can be obtained only on the basis of a systematic approach and coordination of intellectual potential of the various participants in the life cycle of innovative products.

REFERENCES

[1] Charles Poole, Frank J. Owen, "Nanotechnology", Moscow, Technosfera, 2005 (russian).
[2] V. Liopo, V. Struk, *Phonon spectrum and the dimension of the boundary between the nano-and macrophase*, Grodno, Vestnik GrSU, V.1,pp 93-101, 2005 (russian).

ALGEBRAIC METHOD IN CALCULATIONS OF NANO-SCALED OBJECTS PROPERTIES

Yu. Tarasevich

Grodno State University, Belarus

Abstract – The quantum mechanical calculations by means of the algebraic formulation are considered for the nano-scaled objects. The one-dimensional chain of one-dimensional quantum oscillators is selected as a model object sufficient for a range of solid state applications. In the calculations, well known algebraic formulation entities are used, such as the one-dimensional Morse quantum oscillator and the U(2) Lie algebra. The relative importance of the surface effects in the nano-scaled object is represented by considering both the radiation mechanisms and the difference in the behaviour of the quantum oscillator subchains having different lengths. The automation method for dealing with the numerically undetermined coupling parameters is suggested.

I. INTRODUCTION

The algebraic method is considered to be the major methodology in quantum mechanical calculations, besides the (traditional) potential and empirical methodologies. It is rooted in the Heisenberg formulation, and its emergence is usually dated to the late 1970s [1]. The main idea of the method is to represent the energy spectrum of the object with the irreducible representation of the Lie algebra being isomorphic with the object states, and then to manipulate the algebra [2, 3].

The main benefits of the method are: (1) reduction of the volume of computations (the method doesn't require solving the Schroedinger's equation directly and the mathematical manipulations employed in method are considered comparatively "cheap"); (2) in-built provision for anharmonical effects (with the appropriate choice of potential function); (3) possibility to calculate wave functions and thus observables other than energies [1,2,4,5].

The problem of the appropriate algebra and representation choice and construction by now is considered solved, in general. There are some variants to consider here, mainly pertaining to the subsequent organisation of computation. The important implementation steps are: (1) to determine the number of dimensions r sufficient to describe the problem; (2) to determine the part of the spectrum requiring representation (bound, continuous, or both); (3) to select the potential function appropriate for the problem. The primary output of the method's aplication is the energy spectrum, so the principal areas benefitting from the method application are the molecular, nuclear and particle physics.

II. APPLICATION OF ALGEBRAIC METHOD

The application of the algebraic method to the real-world system (molecule, cluster etc.) usually starts with substitution of inter-atomic bonds with the quantum oscillators in one of the well-known potentials. The inherently anharmonic potential functions proposed by Morse and Poeschl-Teller are considered to be an especially good candidates for that. If the problem is limited to r dimensions ($r = 1,2,3$), the algebra U(r+1) for each bond is built. Next, Hamiltonian for the system is formed. The typical Hamiltonian for the system of n bonds (treated as a system of n coupled quantum oscillators) in algebraic formulation is [4,5]

$$H = \sum_{i}^{n} {}_{0i} + \sum_{i}^{n} A_i C_i + \sum_{j}^{n} \sum_{i<j} A_{ij} C_{ij} + \sum_{j}^{n} \sum_{i<j} \lambda_{ij} M_{ij} \tag{1}$$

where ${}_{0\alpha}$ are zero level energies of oscillators labelled α, C_α are Casimir (invariant) operators for the algebras corresponding to oscillators labelled α, $C_{\alpha\beta}$ are invariants describing anharmonicities involving oscillators labelled α and β, $M_{\alpha\beta}$ are Majorana operators describing oscillators (bonds) couplings. The coefficients A and λ depend on object's composition. These might be subsequently fitted to the experimental data. Then, the observables might be calculated etc.

The important point here is that the complete three-dimensional numerical treatment of systems even of relatively modest size ($10 - 10^2$ atoms), even in algebraic formulation, is still involving a very significant volume of computations.

III. Nanofilm and Its Related Model Object

It is well known that the size effects in the nano-objects are direction-related [6]. Nano-scaled objects (nano-objects) are classified, e.g., by the number of object's dimensions which lie in nano-size range ($\approx$1—100 nm). One of the important types of the nano-objects is nanofilm — one-dimensional nano-object. Typically, such object would be placed either on a (massive) layer or between two (massive) layers. The energy (heat) flow in practically interesting setups of this kind is directed more or less along the axis of nano-dimension of the object. Considering the relation of lengths of layers and film along the film's nano-dimension axis, the object might be considered as being effected by plain wave with wavevector directed perpendicularly to the film's macro-plane ("side"). Furthering this assumption, the lateral energy flux in film might be considered negligible (non-existent) and so the problem might be reduced to the problem of longitudal energy flow in manifold of one-dimensional chains, and further, to the problem of energy flow in the one-dimensional chain of atoms.
The one-dimensional (linear) chain of quantum oscillators (harmonic or anharmonic), to which the one-dimensional chain of atoms is reduced, is the basic and well-researched example of the algebraic method application. The algebras involved for every bond are U(2) for the bound states-only problem.

IV. Scaling and Symbolic Computation

Not every nano-object would lend itself to the far-going simplification like discussed in Section III. Extending the calculation to two or three dimensions would generally require more complicated algebras — U(3) and U(4) per oscillator for bound states-only problems, — and the types of Lie algebras involved consist of $O(n^2)$ operators each. Considering more complex systems, like molecular crystals or nano-composites, would raise the complexity even more. Finally, the values of the series coefficients often are unknown. However, in many cases it's possible to reduce This suggests trying for solving in the symbolic form, which might already give a useful results. However, the sheer volume and complexity of such calculations even for systems of 10–10^2 atoms necessitates using the software automation, specifically, a symbolic calculations software package. To this end, we primarily consider two open-source high-end mathematical software packages, MAXIMA and SAGE. As the method requires dealing principally with series and aggregates, even the middle-end packages (like MPFR, CLN, GMP etc.) might do, in certain circumstances.

V. Conclusion

We consider the application of algebraic method to the calculation of physical properties of nano-scaled objects. The method, while offering certain benefits, especially with regard to the volume of computations, requires careful application and would scale satisfactorily only in well-organised environment.

References

[1] F. Iachello, R. D. Levine. *Algebraic Theory of Molecules*. New York, Oxford : Oxford University Press, 1995.
[2] S. Oss, "Algebraic Models in Molecular Spectroscopy", in *Advances in Chemical Physics*: *New Methods in Computational Quantum Mechanics*, vol. 93, pp. 455–649, Wiley, 1996.
[3] И. А. Малкин, В. И. Манько, *Динамические симметрии и когерентные состояния квантовых систем*, Москва : Наука, 1979.
[4] F. Iachello, S. Oss, *Phys. Rev. Lett.* 66:2976–2979, 1991.
[5] S. Oss, *J. Mol. Struct.* 780:87–97, 2006.
[6] A. I. Rusanov, *Surf. Sci. Rep.* 58:111–239, 2005.

NUMERICAL SIMULATION OF METAMATERIALS WITH ACTIVE AND NONLINEAR ELECTROMAGNETIC PROPERTIES

S. Maly

Belarusian State University, Minsk, Belarus

Abstract – The techniques for calculating electromagnetic parameters of metamaterials containing components with non-linear and active properties are considered. The techniques are based on the method of minimum autonomous blocks. The results of computational experiments are presented.

I. NUMERICAL MODELLING OF COMPOSITES AND METAMATERIALS ON THE BASIS OF THE METHOD OF MINIMUM AUTONOMOUS BLOCKS

The design procedure of electromagnetic properties of composites and metamaterials based on a the method of minimum autonomous blocks was developed (MAB) [1]. The MAB method is based on the description of the electromagnetic parameters of subdomains using the apparatus of the scattering matrix. This method has been successfully used for the simulation of electromagnetic processes in structurally inhomogeneous media and to describe their electromagnetic properties [2,3]. Algorithms of realisation of the MAB method are considered. Models of absorbing boundary conditions for external electrodynamic problems are described. Models of local and remote sources are presented. It is established that the techniques developed on the basis of the MAB method provide a full cycle of modeling: including an estimation of average electromagnetic parameters of metamaterials and calculation of optical and microwave systems.

Features of modeling of interaction of electromagnetic radiation with the metamaterials possessing active, nonlinear and combined properties are considered. For calculation of electromagnetic properties of active metamaterials, especially as a part of resonant systems, it is appropriate to use the recomposition algorithm of realisation of the MAB method.

Nonlinear metamaterials are modeled by use of iterative algorithm of the MAB method allowing on each iteration to spend correction of effective electromagnetic parameters depending on amplitudes of channel waves, exciting blocks. Methods of increase of iterative process stability, including use of secondary decomposition of MABs and hybrid algorithms are considered. The models for describe the effects of harmonic generation using a system of related decomposition schemes are proposed.

II. THE ELECTRODYNAMIC ANALYSIS OF THE METAMATERIAL FROM CUBIC DIELECTRIC ELEMENTS

Efficiency of the developed techniques is illustrated by results of calculation of interaction of the plane linearly polarized electromagnetic wave with a flat layer of the metamaterial consisting of cubic elements, located in knots of a square periodic lattice.

The size of the block is 10 mm and the distance between the faces of the neighboring blocks is 4 mm. Plane wave is normally incident on the layer of metamaterial as is shown in Fig. 1. Frequency dependences of reflection and transmission coefficients were presented for the three-layer lattice in Fig. 2 (active metamaterial), and in Fig. 3 (nonlinear metamaterial).
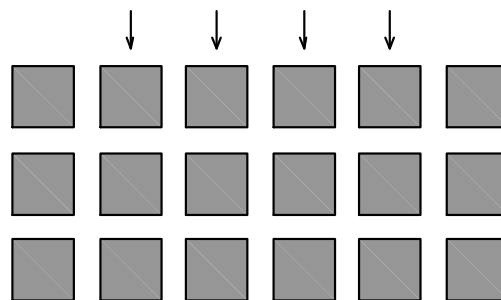

Figure 1 – Flat layer of the metamaterial containing cubic dielectric elements.

To set the active properties of the metamaterial the following values of permittivity and permeability of the material filling cubic elements were used: $\varepsilon = 25 + j2.5$, $\mu = 1 + j0$. Nonlinear material properties were specified as follows: $\varepsilon^m(i,j,k) = \varepsilon_1(i,j,k) + \alpha \max_n(|C_p^m(i,j,k,n)|^2)$;

where (i, j, k) – coordinates of the block in the decomposing scheme; n – channel number; m – iteration number; $\varepsilon_1 = 25$ – stationary part of dielectric permeability; α – nonlinearity factor; $C_p^m(i,j,k,n)$ – complex amplitude of the wave falling on the block in the channel n on iteration with number m.
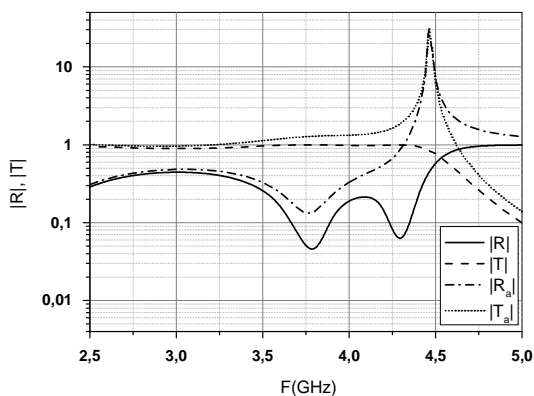

Figure 2 – The frequency dependence of reflection and transmission coefficients for the layer of active metamaterial
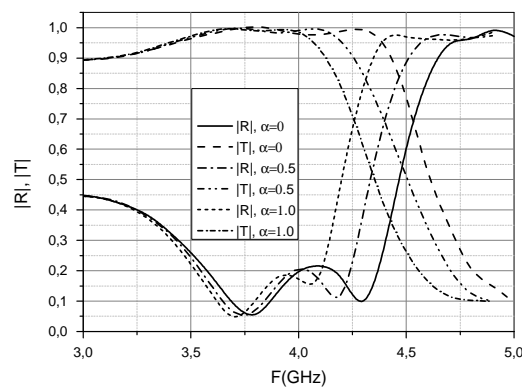

Figure 3 – The frequency dependence of reflection and transmission coefficients for the layer of nonlinear metamaterial

Analysis of simulation results show that the maximum amplitudes of the transmitted and reflected fields correspond to the own resonant frequency of cubic elements. The presence of non-linearity leads to a frequency shift of the curves, with the greatest influence on the reflection and transmission coefficients of the nonlinear properties of materials cubic elements provides at the same resonant frequencies.

III. CONCLUSION

Techniques for electrodynamic analysis of interaction of electromagnetic radiation with metamaterials are developed. Techniques allow to consider active and nonlinear properties of metamaterials. Results of modelling of a metamaterial with cubic elements confirms adequacy and computing efficiency of the developed techniques.

REFERENCES

[1] Nikolskii V.V., Nikolskaya T.I. Decompositional approach to problems of electrodynamics. Moscow, "Nauka", 1983 [in Russian].
[2] Maly S. V. Homogenization of metamaterials on the basis of average scattering matrixes // Abstracts on International conference «Days on diffraction'2010». Saint Petersburg, June 8 – 11, 2010.- P.114.
[3] Maly S. V. The electrodynamic analysis of composites and metamaterials on the basis of the method of minimal autonomous blocks // Abstracts of the International conference "Days on diffraction'2011". – Russia, Saint Petersburg, May 30 – June 3, 2011. - P. 145.

EFFECT OF PULSED ELECTRIC CURRENT TO DEFORMATION OF AMORPHOUS AND NANOCRYSTALLINE METALLIC ALLOYS, AGED IN ACIDIC ENVIRONMENTS

V. Feodorov, T. Pluzhnikova, S. Sidorov, A. Yakovlev
Tambov State University, Russia

Abstract – The influence of aggressive media (20 % solutions H_2SO_4 and HNO_3) intermittent discharge on the strain-based amorphous alloys and cobalt nanocrystalline iron-based alloy, which occurs depending on the σ-ε by passing electrical current pulses. Fitted values depending stress relief in the material density of the pulsed electric current. Investigated the structural and morphological state of the alloy surface after exposure to aggressive media of different concentrations.

I. INTRODUCTION

Expanding the range of application of amorphous and nanocrystalline alloys sets targets for the study of the structure and properties of these materials after various influences. This may be both stationary and non-stationary thermal field pulse and static electric and magnetic fields, and different environment leading to oxidation and corrosion. With its high levels of corrosion resistance, metallic glasses show a significant sensitivity to the effects of hydrogen and corrosive environments, resulting in embrittlement of these materials [1]. The transmission pulse electric current at a high density metallic glass deformation accompanied by a reduction of mechanical stress diagrams fixed on σ(ε) [2]. The purpose of this paper is to study the deformation of amorphous and nanocrystalline metallic alloys by pulsed electric current after exposure to corrosive environments.

II. RESULTS AND DISCUSSION

The object of the study were chosen amorphous metal alloys based on cobalt (AMAG - 172 AMAG - 180) and nanocrystalline alloys based on Fe (AMAG - 200) obtained by spinning. Sample sizes: ~ 3,5 × 0,02 × 40 mm. Corrosive environment is a 20% solution of sulfuric and nitric acids. Samples were preincubated for 40 minutes. Then the samples produced by uniaxial stretching tensile testing machine Instron-5565 with a speed of 0.1 grippers mm / min while a pulsed electric current duration τ = 5 ms, and the current density $j = 10^8$-10^9 A/m^2.

Deformation of the AMC while passing an electric current pulse on the charts load accompanied by the phenomenon similar electroplastic effect, the well-studied for crystalline structures [3-4]. At the time of the current pulse in the diagrams σ-ε there is a short (~ 1.1 s), the decline of stress Δσ followed by complete recovery of stroke depending on σ-ε.

The experimentally observed that after soaking in 20% sulfuric acid in amorphous alloys, Co-base, the reset value of the mechanical stresses caused by passing a pulsed current is reduced by Δσ ≈ 20 % in comparison with the amount of discharge of the samples in the initial state (Fig. 1 a, b). A delay of 20 % nitric acid solution reduces the amount of stress relief by 30 % compared with the effects of sulfuric acid and 50% as compared with resetting. Effects on the acidic environment nanocrystalline Fe-based alloy does not affect the release of mechanical stress.

Decrease in the discharge of stress may be due to surface phenomena occurring. In Fig. 2b is a view of the surface of the sample after exposure to an acidic environment. It is seen that the exposure to the acid environment of amorphous materials leads to surface oxide formation, the study confirmed that the element composition. It was found that almost the entire area of the specimen surface covered sulfate formations thickness around 3 microns.

The formed oxide film on the surface reduces the metal section of the sample which leads to an increase in resistance and decrease in current acting on the sample. This accordingly causes less heating of the sample, whereby the amount of discharge decreases mechanical stress caused by passing a pulsed current.

Cobalt metal is capable of absorbing large amounts of hydrogen [5], not forming a compound of constant composition. Therefore, hydrogen is apparently not evaporate and remains in the surface layer of the material, causing embrittlement is observed experimentally.

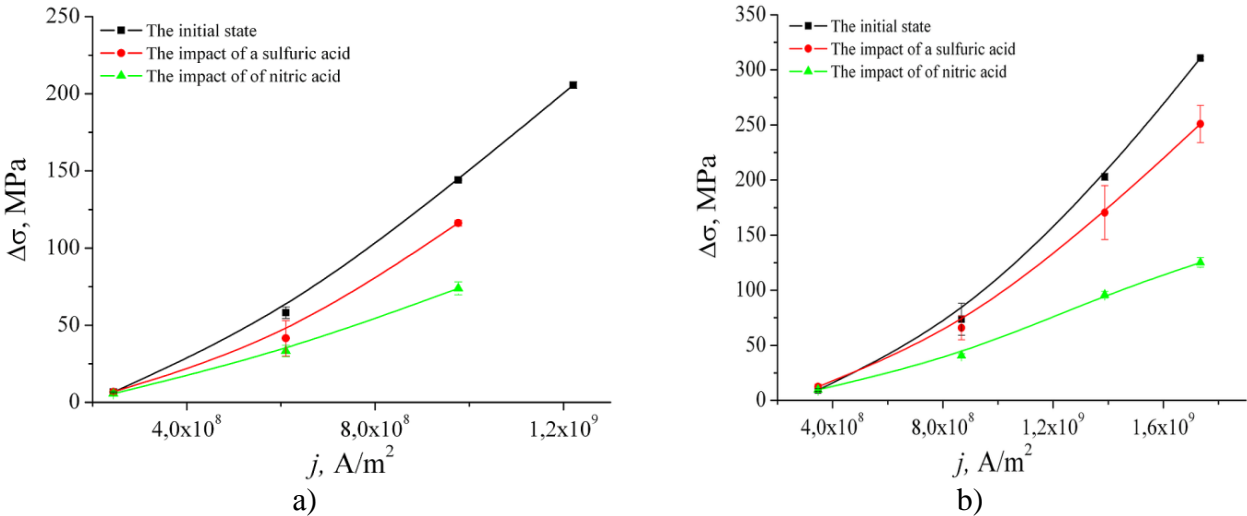a)   b)

Figure 1 –The dependence of the strain relief of the current density in the alloy:
after exposure to a 20% solution of sulfuric and nitric acids: a) AMAG-172 b) AMAG-180

Soak nanocrystal alloy on the basis of iron in the solutions of sulfuric acid leads to the formation of pitting corrosion (Fig. 2). The characteristic size of pitting of the basins is 300 - 350 nm depth $\approx$ 40 nm. When this takes place decrease the value of the tensile strength of the alloy. So ,for example, after the impact of solution of sulfuric acid and 4 of the current pulse density of $2\times10^8 - 2\times10^9$ A/m2 tensile strength is reduced by 20%.

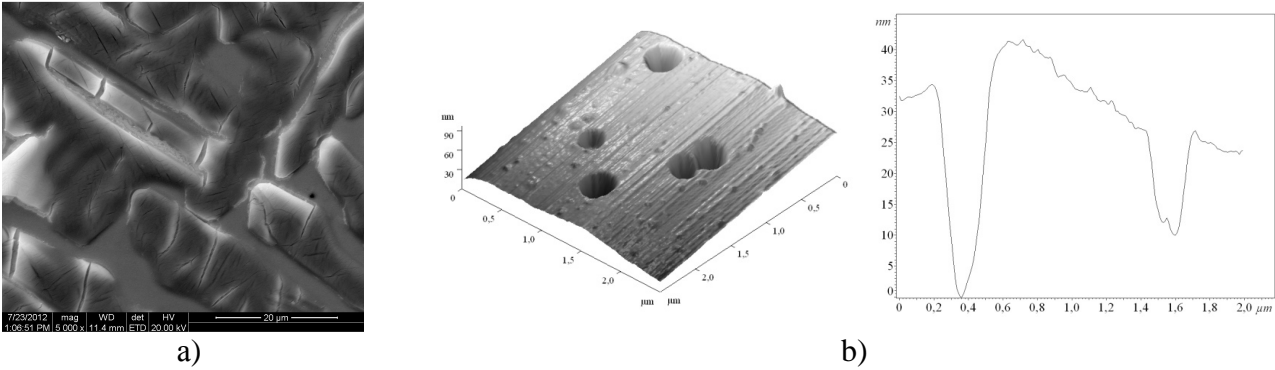a)   b)

Figure 2 – Sulphate formation on the surface of the AMAG-180 after the impact of the 20% solution
of sulfuric acid (a); pitting corrosion on the surface of the nanocrystal alloy AMAG-200 (b)

III. CONCLUSIONS

The acid environment forms sulfate compounds on the surface of amorphous alloys, leading to a considerable reduction in the metal section of the sample, which causes an increase in the resistance of the material, reducing the force of the current, and consequently, leads to lower heating of the sample, therefore, decreases the value of the reset of the mechanical load.

In nanocrystalline alloys, in spite of pitting corrosion, stored value reset mechanical stress by passing a pulse of electrical current.

Change of discharge of the mechanical stress caused by pulse current, in the investigated alloys after soaking in aggressive environments due only to the change of the heating alloys.

REFERENCES

[1] A. M. Glazer, I. E. Permjakova, V. E.Gromov, V. V. Kovalenko *Mechanical behavior of amorphous alloys*, Novokuznetsk. SibGIU Publishing, 2006.

[2] S. A. Sidorov, V. A. Fedorov, T. N. Pluzhnikova, A. M. Kirillov, A. V. Yakovlev, A. A. Chernikova, "Investigation of the processes of deformation of amorphous alloys in a pulsed electric current", *Bulletin of the University of Tambov. Series: Natural and technical science*, Vol. 17, Issue. 1, 2012, pp. 135-138.

[3] V. I. Spitcyn, O. A. Troitckii *Elektroplasticheskaia deformatciia metallov*. M. Science, 1985.

[4] I. L. Bataronov, "Mechanisms elektroplastichnosti", *Soros Educational Journal*. № 10. 1999. pp. 93-99

[5] K. A. Bolshakov *Chemistry and Technology of cobalt*. M. MITHT, 1981.

STRUCTURE OF ZnO THIN FILMS DOPED
WITH RARE EARTH COMPOUNDS

V. Koleshko, A. Gulay, A. Shevchenok, T. Kuznetsova, V. Gulay
Belarusian National Technical University, Minsk, Belarus

Zinc oxide thin films doped with rare earth compounds (rare earth oxides and fluorides) up to the 1–4 mass % concentration were produced by the ion-beam sputtering of the ceramic targets of the stoichiometric composition. The thin film surface morphology of the nanometer scale thickness was studied by the atomic force microscopy (AFM) with the use of the NT-206 microscope (Microtestmashiny Co., Belarus) equipped with MicroMasch Co. (Russia) standard silicon probes. The probe edge radius is 10 µm, the vertical resolution is 0.2 nm, and the horizontal resolution is 2 nm.

For the ZnO-YF$_3$ (1mass %) thin films deposited for 6–10 min, the surface roughness is 0.1 – 0.5 nm in the field of 1.5×1.5 µm. The AFM surface relief image made in the topographical mode contains noise interference in the form of parallel horizontal breakups and bands placed diagonally at regular intervals as seen in Fig. 1. Distinguished grain boundaries are not observed at that because the grain structure has no time to be formed at this stage of the thin film growth. Dark rounded islands consisted of 20 nm sized clusters against a light background substrate can be revealed in the image made in the "Torsion" mode.

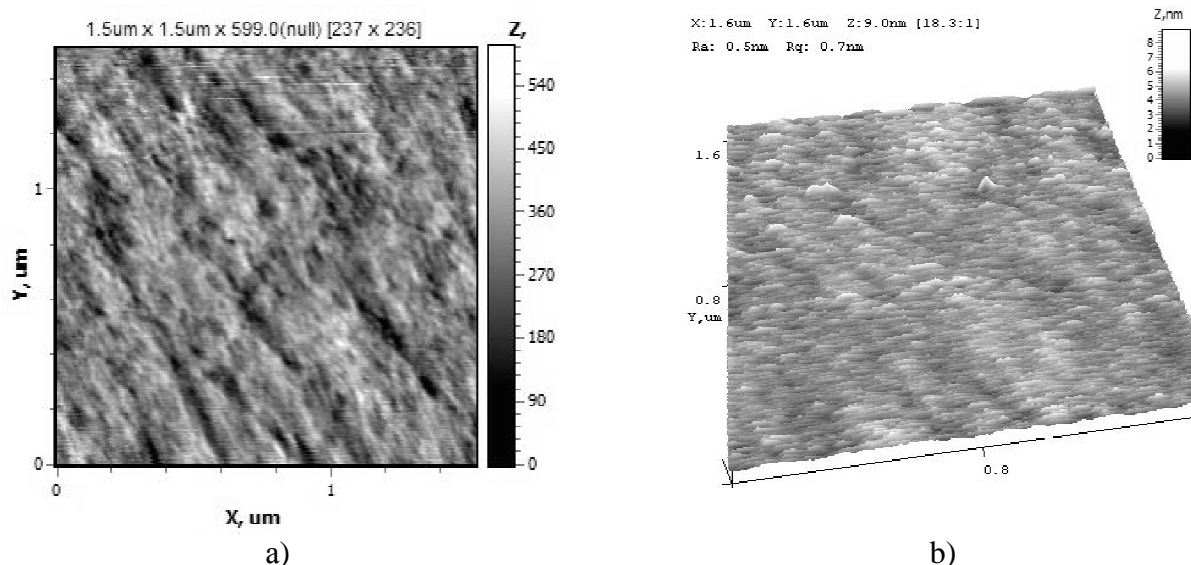a)   b)

Figure 1 – The AFM surface image of the thin film deposited for 6 min at right angles:
(a) 2D image made in the tapping mode, scan field is 5×5 µm;
(b) 3D image made in the topographical mode, scan field is 1.5×1.5 µm.

An increase of the deposition time to 60 min results in the formation of a thin polycrystalline film with the obvious grain structure. The film surface roughness is 1.3 nm in the field of 1.3×1.3 µm as shown in Fig. 2. A two-phase structure is revealed in the tapping mode, i.e. dark rounded grains 20 nm in diameter and light grains about 50 nm in diameter are observed. Light grain boundaries are clearly defined, grains are round shaped. Dark grains are located, at a rule, in the triple nodes of the light grain boundaries, i.e. in the cavities. Their quantitative content, area distribution and contrast against the rest of surface allow us to assume in the grain yttrium containing phase.
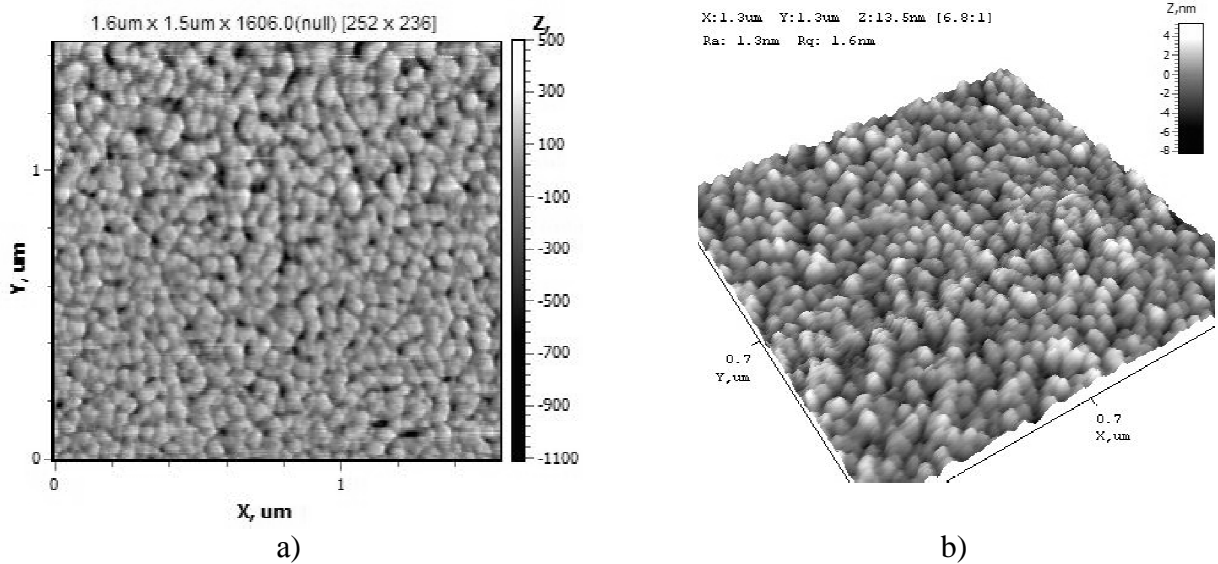
a)   b)

Figure 2 – The AFM surface image of the thin film deposited for 60 min at right angles:
(a) 2D image made in the tapping mode, scan field is 1.6×1.6 µm;
(b) 3D image made in the topographical mode, scan field is 1.3×1.3 µm.

A thin film crystallite development degree depends on both the deposition time and the angle between the flow of material deposited and the substrate surface. So, the thin film surface roughness is nearly halved (from 1.3 nm to 0.6 nm in the 1.3×1.3 µm field) if the deposition angle decreases from 90º to 30º. Grains of the light phase are observed in the image made in the "Torsion" mode as shown in Fig. 3. The grain length is twice as much as the grain width. In the image made in the topographical mode grain boundaries have no clear outline.
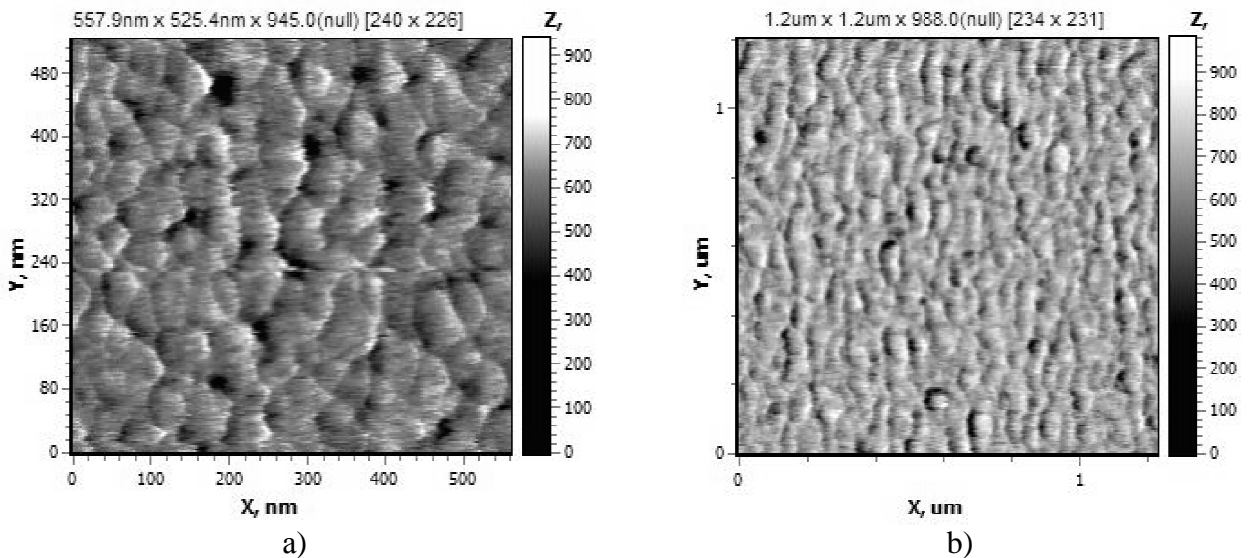

a)   b)

Figure 3 – The AFM surface image of the thin film deposited for 60 min in the tapping mode:
(a) at right deposition angles, scan field is 0.5×0.5 µm;
(b) the deposition angle is 30º, scan field is 1.2×1.2 µm.

The film texture can be revealed when the texture axis is placed diagonally against the AFM scan direction as shown in Fig. 4. The grain elongation direction is defined by the sequential surface scanning in concurrent orthogonal directions. At the scanning along the texture direction, grain boundaries are reveals only in the topographical mode while at the scanning across the texture direction, grain boundaries are reveals in the AFM "Torsion" mode to be in agreement with the operation principle of lateral forces in this mode.

X:1.2um Y:1.2um Z:6.6nm [14.9:1]
Ra: 0.7nm Rq: 0.9nm

801.5nm x 801.5nm x 1949.0(null) [256 x 256]

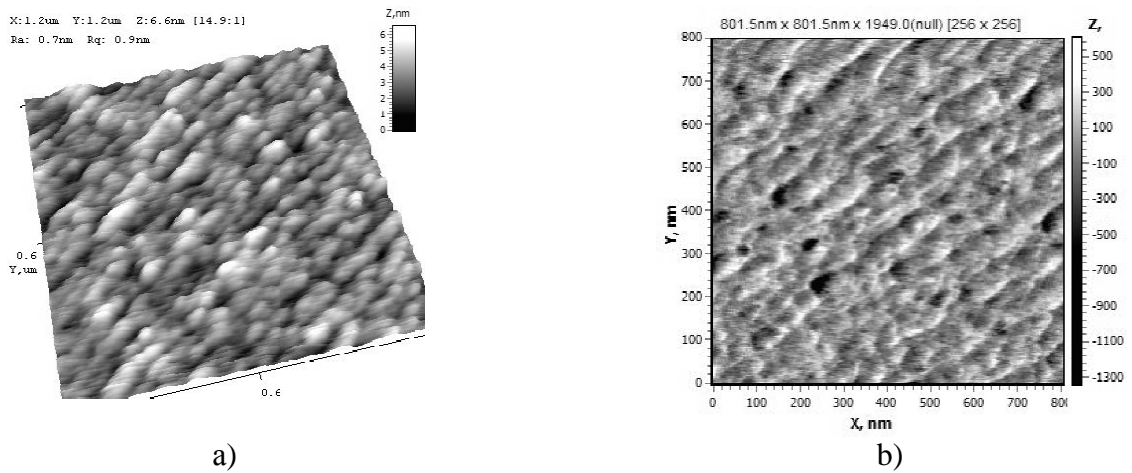a)   b)

Figure 4 – The AFM surface image of the thin film deposited for 60 min at right angles:
(a) 3D image made in the topographical mode, scan field is 1.2×1.2 µm;
(b) 2D image made in the tapping mode, scan field is 0.8×0.8 µm,
texture is placed at an angle of 45º to the scan direction.

Comparing a surface morphology of thin films obtained at different deposition times, the following can be noted. Rounded dark islands ("Torsion" mode) are observed in all films equal in nearly equal amounts to be nearly equal in size at that. Apparently, this is a containing rare-earth element phase which is the first to be crystallized on the substrate. But number of yttrium-containing islands distributed over the surface differs insignificantly for the 1 mass % and 4 mass % YF_3 concentration. Rare earth compounds may be assumed to serve as additional zinc oxide crystallization centers at the thin film formation.

The research into the structure of zinc oxide thin films is of a considerable interest for the fabrication of sensors of various physical parameters, specifically gas concentration sensors. Adsorption and diffusion rate is dependent on the grain size and grain boundary development in the thin film to define finally operation behavior of gas sensors based on zinc oxide thin films.

GENERAL GROWTH PATTERN OF ANODIC ALUMINUM OXIDES

V. Sokol, V. Yakovtseva

Belarusian State University of Informatics and Radioelectronics, Minsk, Belarus

Abstract – One of the effective methods for the formation of coatings with required functional properties on the aluminum surface is the anodization. Usually anodic aluminum oxides are divided into dense (barrier) and porous. This work shows that such the division is very conditional. In any electrolyte, the alumina film origin and growth is defined by two factors. These are the rate of Al→Al$_2$O$_3$ transformation at the aluminum/alumina interface (V_0) and the rate of the alumina dissolution at the alumina/electrolyte interface (V_d). In all cases $V_0 \gg V_d$. When $V_d \to 0$, a preferential growth of dense alumina takes place. However, V_d is never equal to zero, even in water. It depends on the electrolyte composition, concentration and temperature and ion current density (J_i). With specified electrolyte, temperature and anodization voltage, only the anodization time defines either dense or porous alumina will be formed.

I. INTRODUCTION

Anodization is one of the effective methods for the formation of alumina films with required functional properties on the aluminum surface. Note the following advantages of this method [1]. Firstly, the film is grown directly from the metal body instead of outer deposition, so the adhesion problems stand no longer. Secondly, the quality of the alumina film grown can be controlled by the variation of the electrolyte nature and quantitative composition as well as varying the conditions and electrical parameters of the anodization process. To work in practice the method advantages in full, a comprehensive study into the mechanism and formation conditions of desired alumina films is needed. The research in this field can open new potentialities in the formation of coatings with a specified set of functional properties.

II. RESULTS AND DISCUSSION

Usually anodic aluminum oxides are divided into dense (barrier) and porous. But such the division is very conditional. When aluminum is anodized in any electrolyte, the alumina film origin and growth is defined by two factors. These are the rate of Al→Al$_2$O$_3$ transformation at the aluminum/alumina interface (V_0) and the rate of the alumina dissolution at the alumina/electrolyte interface (V_d). In all cases $V_0 \gg V_d$. At $V_d \to 0$, a preferential dense alumina growth takes place. However, V_d is never equal to zero, even in water. It depends on the electrolyte composition and concentration, temperature and ion current density (J_i). With the specified electrolyte, temperature and anodization voltage, only the anodization time defines either dense or porous alumina will be formed.

It should be noted that the anodic alumina formation is possible only in the presence of ion current due to which an oxygen ion delivery to the aluminum/alumina interface is provided. When voltage is applied between the anode and cathode, a common current through the alumina film is equal to sum of ion (J_i) and electron (J_e) currents. The electron current does not participate in the oxide formation and is defined only by the oxide structure characteristics (lattice damages, ion inclusions, etc.). Its value is much less than the ion current value. So, in the presence of J_i, the electron current is neglected.

Definite rates V_0 and V_d are characteristic for any definite electrolyte. And with the electrolyte, temperature and anodization voltage specified, only the anodization time defines either dense or porous alumina will be formed. So, if the anodization time is so short that the thickness of the anodic film dissolving at the alumina/electrolyte interface is negligible, dense alumina may be said to be formed. Denote this time by t_{dense}. Of course, this time is defined by the ratio of the growing film thickness h_0 to the thickness of the film part dissolved h_d, i.e. by any factor $k_0 = h_d/h_0$. in ideal case, $k_0 = 0$. So, permissible anodization time can be determined by specifying k_0. When the anodization time is longer than t_{dense}, porous alumina may be said to be formed.

It is known that the porous alumina growth rate is defined by the dissolution rate at the pore bottom, which depends on the ion current density - other things being equal. When the ion current density increases, the dissolution rate $V_d \to V_0$. When $V_d \approx V_0$, a well-known aluminum polishing process takes place.

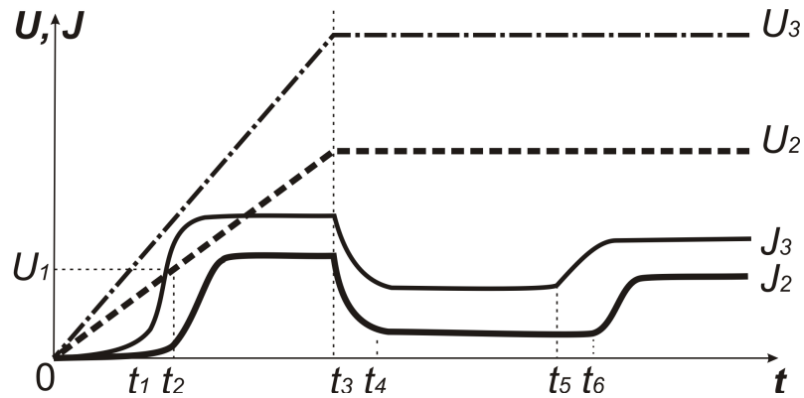Fig. 1 shows the growth kinetics of dense anodic alumina.

Figure 1 – Growth kinetics of dense anodic alumina in the range of low oxide dissolution rates

Because 5 – 7 nm thick dense native oxide is at the aluminum surface, only the electron current flows through the oxide at the initial anodization stage to t_1 and t_2. When the anodization voltage increases up to U_1, the electrochemical breakdown of the native oxide film begins and the ion current appears which increases sharply at $t > t_1$ or $t > t_2$. A value U_1 is evaluated as $U_1 = h_{initial}/k_0$, where $h_{initial}$ is a thickness of the initial native alumina (nm) and k_0 is a well-known anodization constant equal to 1.4 nm/V. The ion current is constant up to the moment t_3 and higher is voltage scan rate, higher is a value of this current.

At the moment t_3 the voltage $U_2 = $ const and the ion current falls. Some increase of the oxide effective thickness is observed during the current fall time. After t_4 only the electron current takes place and the alumina films stops growing. It is considered that this electron current is less than 0.1 from the current at t_3. A period $\Delta t = t_4 - t_3$ is about 10 min. The current is practically constant for a long time up to t_5 (or t_6). However, the alumina film undergoes a certain change associated with its electrochemical dissolution at that. Practically, the oxide surface is not ideal, i.e. defect regions (crystal lattice damages, ion inclusions, etc.) are observed. As a rule, the dissolution rate is higher in these regions, so they are considered as pore nuclei. With time, pores grow deep into the oxide film and its diameter increases. At some moment walls of neighboring pores come to the contact and pores start grow only into the oxide depth.

Up to this moment all processes take place without the participation of the ion current. But the moment comes when the pore growth into the oxide depth results in such the oxide thickness at the pore bottoms that the electrochemical breakdown happens and the ion current appears within the pores, i.e. a classical growth of porous alumina begins. This corresponds to the t_5 and t_6 moments in Fig. 1. The alumina dissolution rate at the pore bottoms is very low in the electrolytes for the dense anodization, so the growth rate of porous alumina in such electrolytes is very low.

Fig. 2 shows the growth kinetics of porous anodic alumina in the range of high oxide dissolution rates.
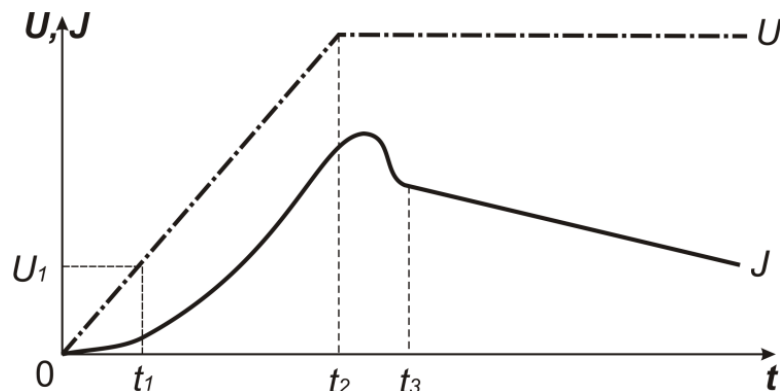

Figure 2 – Growth kinetics of porous anodic alumina in the range of high oxide dissolution rates

Only the electron current flows through the oxide to the moment t_1 as in the case shown in Fig. 1. When the anodization voltage increases up to the electrochemical breakdown voltage of the native oxide film at the aluminum surface U_1, the ion current appears which increases. In contrast to the case in Fig. 1, this current increases steadily up to the moment t_2 when the constant anodization voltage is observed. At this time ($t \geq t_1$) the pores nucleation takes place. In the time of $t_1 \rightarrow t_2$ the pore restructuring happens. Number of pores decreases with the anodization voltage in compliance with the well-known fact that the pore diameter and cell size are proportional to the anodization voltage. In the $t_2 - t_3$ time range a fixed amount of pores per the aluminum unit surface area is established. At $t \geq t_3$, pores grow into the oxide depth and the current decreases due to the voltage drop in the pore channels.

The growth kinetics form shown in Fig. 2 is independent of the electrolyte (sulfuric, oxalic, phosphoric and other acids) though quantitative values of the parameters at various time moments are different.

III. Conclusion

Thus, the division of anodic alumina film into dense and porous is very conditional. In any electrolyte, the alumina film origin and growth is defined by two factors. These are the rate of Al$\rightarrow$Al$_2$O$_3$ transformation at the aluminum/alumina interface and the rate of the alumina dissolution at the alumina/electrolyte interface. When the dissolution rate tends to zero, a preferential growth of dense alumina takes place. It depends on the electrolyte composition and concentration, temperature and ion current density. With the specified electrolyte, temperature and anodization voltage, only the anodization time defines either dense or porous alumina will be formed.

References

[1] V. A. Sokol, *Anodic alumina*. Minsk, Belarus: Bestprint, 2011, 431 p.

PLASMA-MECHANICAL OSCILLATIONS IN CARBON NANOTUBES ARRAY

A. Danilyuk, *D. Podryabinkin*
Belarusian State University of Informatics and Radioelectronics, *Minsk*, *Belarus*

Abstract – The results of the simulation of plasma-mechanical oscillations in carbon multiwalled nanotubes array under electromagnetic radiation are presented considering thermal fluctuations, internal stress, static load and the ponderomotive forces between the nanotubes.

I. INTRODUCTION

Recently a great interest in the study of the interaction between the electromagnetic radiation (EMR) with the frequency range from 1 GHz to 1 THz and the carbon nanotubes (CNTs) arrays has grown up. Despite the large number of existing works on measurements and modeling of these processes, many things still remain unclear. The cases of interaction of the EMR with individual single-walled CNTs are mainly considered in the theoretical works, while the known phenomenological models developed for composites containing nanoparticles are used in the experimental works for the interpretation of the data obtained.

The aim of the work is to simulate the plasma-mechanical oscillations in a multi-walled carbon nanotubes array under the influence of electromagnetic radiation taking into the account the ponderomotive forces between the nanotubes, thermal fluctuations, stress and static load.

II. PLASMA-MECHANICAL OSCILLATIONS

The real arrays of aligned CNTs are far from perfect, they are characterized by heterogeneity, the presence of branches, intersections, curves, bridges, contacts between the tubes and the inclusion of magnetic nanoparticles. The characteristic dimensions of the free fragments of CNTs between the points of attachment, contact, or bending are tens or hundreds of nanometers.

Free fragments of CNTs in the array, having high elasticity, undergo mechanical vibrations. Such fluctuations are caused both by external (mechanical stress, heat, electric and magnetic fields, currents) and inner (thermal fluctuations, magnetoelastic effects, residual strains and stresses) factors. The free CNT fragments are characterized by natural frequencies of mechanical oscillations, the values of which are determined, additionally to the CNTs radii, the elastic moduli and the lengths of these areas, by the presence of fixtures and strains.

The charge fluctuations are determined by the characteristic frequencies of plasma oscillations, which are excited by passing a current through a nanotube, and external radiation. EMR generates eddy currents in the conductive CNTs with characteristic frequencies depending on the CNTs size, their conductivity, and the Fermi velocity, which values lie in the range of 50 GHz and above.

Multi-walled CNTs with a diameter of 30-50 nm and a length of 300-500 nm oscillate with a natural frequency of the mechanical vibrations of 1-2 GHz and have a quality factor of 1000 at room temperature [1].

III. RESULTS AND DISCUSSION

The calculations performed have shown that the mechanical vibrations of CNTs may be excited both by the presence of the original CNT bending under the static load, and due to the charge oscillations of neighboring CNTs. In the first case, in the absence of repulsive forces between the CNTs the vibrations are damped with a time determined by the damping constant γ. In the second case, the oscillations are forced.

The results obtained for the case of a relatively small external force are shown in Fig. 1 for center of CNT corresponding to the center of the free CNT fragment.
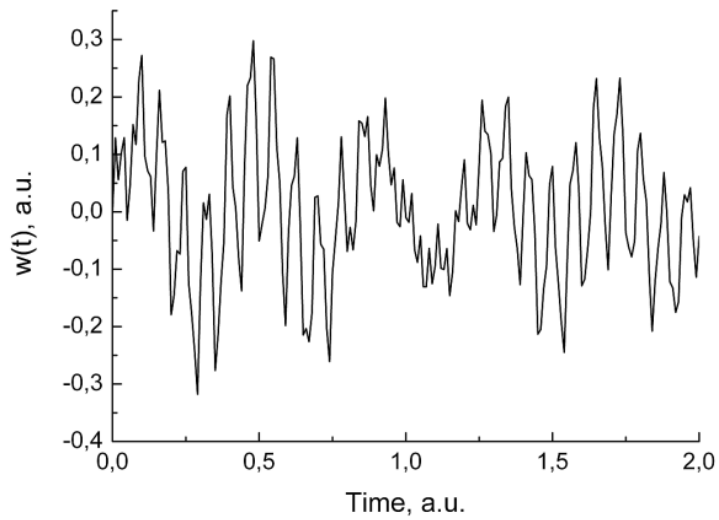
Figure 1 - The CNT fluctuations in the case of relatively small repulsion force between the CNTs.

IV. Conclusion

With the growth of the repulsive force at a frequency of about 80 times greater than CNTs natural frequency, the amplitude-modulated periodic oscillations appeared with two characteristic frequencies.

The preliminary results of the calculations have shown that the presence of the noise component of force leads to stochastic fluctuations.

References

[1] D. Dragoman, M. Dragoman. Electromagnetic wave propagation in dense carbon nanotube arrays// J. Appl. Phys. – 2006. – Vol.99, – P.076106 (3 pages).

SECTION 2. APPLICATIONS OF NANOMATERIALS (ELECTRONICS, MECHANICS, BIOLOGY etc.)

PROTON-CONDUCTING MEMBRANE WITH SPATIALLY HETEROGENEOUS STRUCTURE BASED ON POLYMER-SILICA NANOCOMPOSITES

E. Trofimchuk[1], N. Nikonorova[1], I. Meshkov[2], A. Muzafarov[2], M. Gallyamov[1], D. Kondratenko[1], N Bakeev[1, 2]
[1]*Moscow State University, Russia*
[2]*Institute of Synthetic Polymeric Materials RAS, Russia, Moscow*

Abstract – An original approach for the preparation of ternary proton-conducting membranes consisting of high density polyethylene (PE), silicon dioxide, and phosphoric acid for the intermediate temperature (140-180 ^{o}C) fuel cell is presented. The base of this method is a template synthesis of silica phase using hyperbranched polyethoxysiloxane as a precursor by hydrolytic condensation reaction within the volume of the nanoporous polymer matrix with pore's diameter of about 10 nm obtained via the mechanism of delocalized solvent-crazing. The received polymer-silica nanocomposites containing up to 40 wt.% of SiO_2 were characterized by a structure of two interpenetrating networks, and silicon dioxide formed a rigid three-dimensional framework. Loading of composites by phosphoric acid was carried out by their heating in an environment of H_3PO_4 at 160 ^{o}C that was above the melting point of PE. In this case, the polyethylene melt migrated from inner volume to surfaces of the composite while emerged pores were filled with acid. The amount of introduced acid increased linearly with a growth of silica phase in the composite and maximum content of H_3PO_4 equaled to 50 wt.%. The proton-conducting membranes obtained are characterized by conductivity of 0.03 S/cm and the best performance of 0.4 V at current densities of 0.4 A/cm^2 at 160 ^{o}C.

I. INTRODUCTION

Today polymeric materials characterized by the high proton conductivity (10^{-3}-10^{-1} S/cm) attract the considerable interest because they are prospective as the proton-conducting membranes for fuel cells (FC). FCs are well known as a promising alternative power sources due to their high efficiency of energy conversion and low pollutant emission [1]. Conductive channels in the similar polymer membranes are usually formed via the microphase separation of the hydrophobic and hydrophilic regions as in Nafion, or via loading of a large amount of the conductive component (about 5 molecules of the filler per monomer unit) as in polybenzimidazoles.

In this paper the conductive channels are proposed to form using crazing mechanism, i.e. in the process of uniaxial stretching of polymer films in the liquid medium. It is known [2] that solvent-crazing allows to create a system of highly dispersed interpenetrating pores in the solid amorphous and semi-crystalline polymers, as well as filling the polymer matrices by substances of different nature, including thermodynamically incompatible with it (metal, oxides, salts, etc.).

The aim of this work is the development of an approach for the preparation of proton-conducting membranes based on high density polyethylene (HDPE) and phosphoric acid (PA) using a process of solvent-crazing.

II. RESULTS AND DISCUSSION

The matrices characterized by the open nanoporous structure were obtained on a base of the commercial film of high density polyethylene (M_w=2×10^5, degree of crystallinity 70%, T_{melt}=130°C, thickness 75 μm) via the mechanism of delocalized crazing [1]. In order to give HDPE the proton conductivity, porous films were saturated by 85% solution of PA. These materials possessed relatively high proton conductivity of about 1×10^{-4} S/cm (Fig. 1, curve 2), but they were not stable over time due to the exudation of a hydrophilic acid at the surface of hydrophobic HDPE.

To prevent migration of the proton-conducting compound and to increase the stability of membranes, the phase of silica that is formed a hydrophilic backbone was synthesized within the

polymer films. Hyperbranched polyethoxysiloxane, HPEOS ($M_w=3\times10^4$, density 1.17 g/cm^3, viscosity 18.8 cP, effective diameter of molecule 2-5 nm) was used as the precursor of SiO_2. HPEOS was introduced into the polymer matrix via crazing and then it was transformed into silicon dioxide directly in the pores' volume by hydrolytic condensation process (catalyst – 10% water solution of HCl). The obtained silica-containing composite was loaded with concentrated PA at the room temperature. Although in this case the content of acid in the membranes did not exceed the 10 wt%, it is allowed to receive materials with a comparable level of conductivity (Fig. 1, curve 4) and significantly increase their stability in time (the conductivity of the membranes after a year of their storage under room conditions decreased by one order).

It should be noted that the level of conductivity of 10^{-5} S/cm is insufficient to obtain a proton-conducting membrane characterized by good performance. To increase the acid content, the polymer-silica composites were heated at 160-170°C, which is above the melting point of the polymer matrix, in the environment of PA during 0.5-2 hrs. After similar a thermal treatment, the content of acid in the samples was found to greatly rise and the amount of PA increased linearly with the growth of SiO_2 content as shown in Fig. 2.

By scanning electron microscopy, it was found that the surface of a composite was coated with islands of polyethylene film thickness of 3 μm after the heat treatment (Fig. 3a). Moreover, maps of the distribution of elements (C, Si and P), obtained by energy dispersion spectrometry, showed that carbon as part of a polymer was concentrated on the surface of a sample (Figs. 3b,d), silicon as part of silica and phosphorus as part of acid almost uniformly distributed over the whole volume (Fig. 3e). One can assume that a polymer melts and migrates from the bulk of the composite at the surface during the heating. Simultaneously, PA, which is well compatible with SiO_2, flows into a volume of a composite and fills the formed voids.
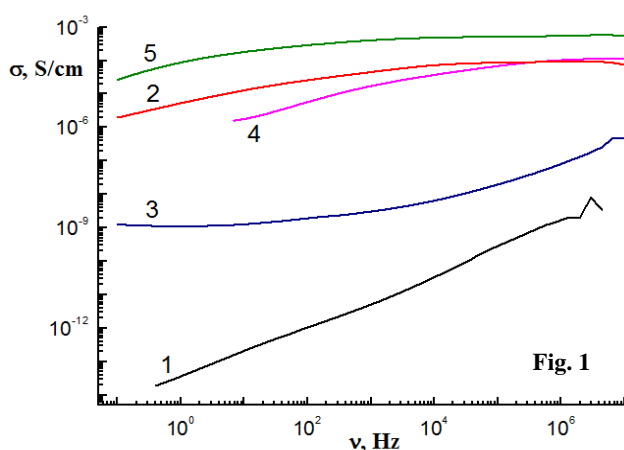

Figure 1 – Dependence of the conductivity of samples from frequency: (1) initial porous HDPE film, (2) HDPE-H$_3$PO$_4$, (3) HDPE-SiO$_2$, (4) HDPE-SiO$_2$-H$_3$PO$_4$, (5) HDPE-SiO$_2$-H$_3$PO$_4$ after heat treatment
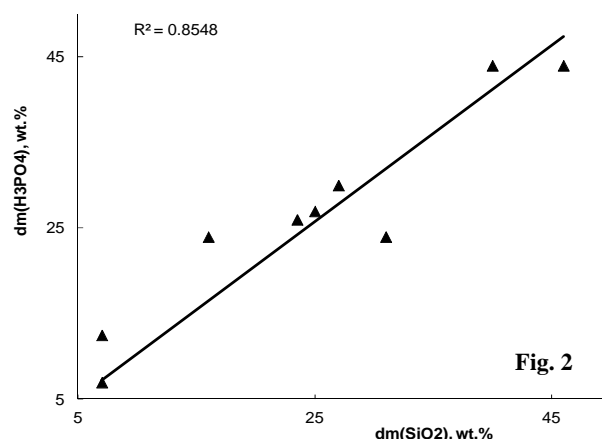
Figure 2 – Dependence of the amount of introduced acid from the content of SiO_2 in the composite

The obtained materials HDPE-SiO$_2$-H$_3$PO$_4$ were tested in a membrane-electrode assembly as proton-conducting membranes. Hydrogen as a fuel and air as an oxidant were supplied without excessive pressure and without humidification. It was found that these membranes at 160°C have a conductivity of about 3×10^{-2} S/cm and the performance of 0.4 V at current density of 0.4 A/cm^2.

III. CONCLUSION

Thus, the proton-conducting membranes based on silica-containing polyethylene and phosphoric acid can compete with commercial membranes. The combination of sufficiently good electrical conductivity, performance, mechanical properties at a relatively low price makes these materials economically attractive.
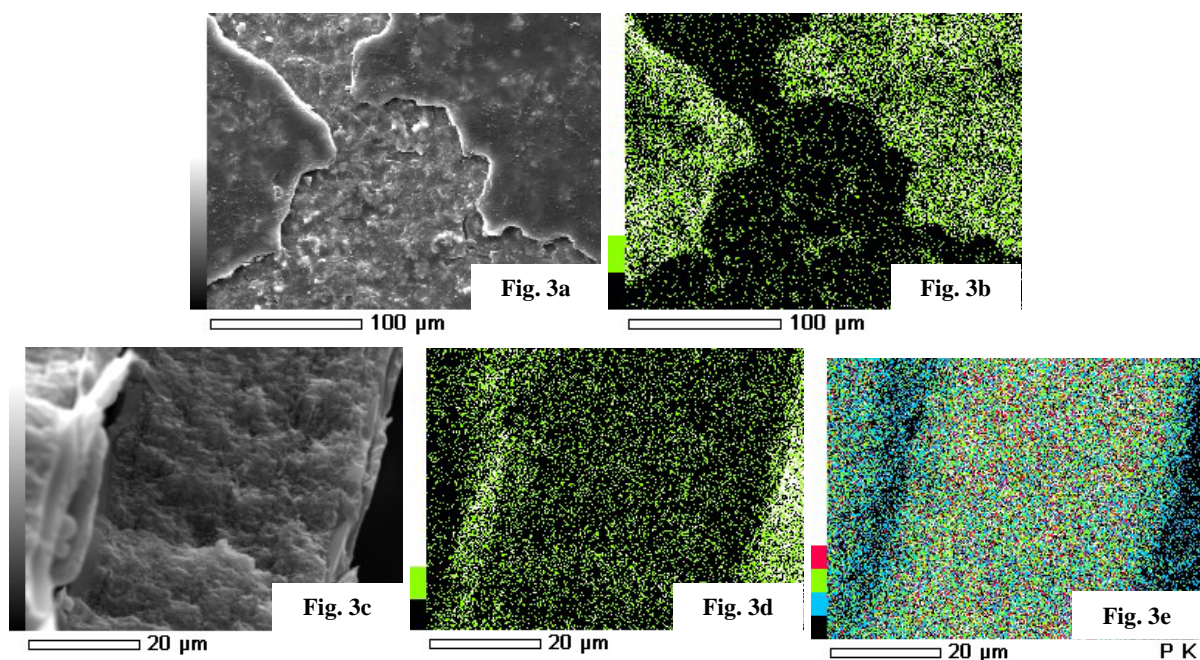
Figure 3 – SEM-micrographs of HDPE-SiO$_2$- H$_3$PO$_4$ after heat treatment.

REFERENCES

[1] Y. Wang, K. S. Chen, J. Mishler, S. C. Cho, and X. C. Adroher, "A review of polymer electrolyte membrane fuel cells: technology, applications, and needs on fundamental research," *Appl. Energy*, vol. 88, pp. 981-1007, 2011.

[2] A. L. Volynskii, and N. F. Bakeev, *Solvent crazing of polymers*. Amsterdam: Elsevier, 1995.

[3] E. S. Trofimchuk, E. A. Nesterova, I. B. Meshkov, N. I. Nikonorova, A. M. Muzafarov, and N. Ph. Bakeev, "Polypropylene/silicate composites on the basis of crazed polymer and hyperbranched polyethoxysiloxane," *Macromolecules*, vol. 40, pp. 9111-9115, 2007.

[4] A. S. Gruzd, E. S. Trofimchuk, N. I. Nikonorova, E. A. Nesterova, I. B. Meshkov, M. O. Gallyamov, and A. R. Khokhlov, "Novel polyolefin/silicon dioxide/H3PO4 composite membranes with spatially heterogeneous structure for phosphoric acid fuel cell," *Int. J. of Hydrogen Energy*, vol. 38, pp. 4132-4143, 2013.

FULLERENE-BASED SYSTEMS AS COMPONENTS OF NANOELECTRONIC DEVICES

M. Britch[1], *K. Dobrego*[1], *L. Krasovskaya*[2]
[1] *Heat and Mass Transfer Institute, NASB, Minsk, Belarus*
[2] *Belarusian State Technological University, Minsk, Belarus*

Abstract –The electric conduction of a single fullerene molecule and chains of fullerenes placed between two metal electrodes was simulated. The electric current was calculated as a function of the bias voltage using the Landauer approach, which connects charge transport with the transmission of electrons. To obtain the transmission function, the supplementary problem of the electron tunneling coupled with its scattering by the fullerenes was solved. It has been shown that the current - voltage characteristics of such structures can have negative-conductance regions that makes it possible to use them as active components of nanoelectronic devices. As an example, the operation of the oscillator including the single fullerene-based component has been demonstrated. The interpretation of the phenomenon has been discussed.

The current–voltage characteristics of systems including fullerenes (the single fullerene molecule or small clusters of fullerenes placed in a gap between two metal electrodes), as it has been shown in [1], have negative-conductance regions. This makes it possible to use them as active components for nanoelectronic devices.

We extend this study to consider similar problem for chains of fullerenes and the influence of the electrode material on the phenomenon. Distances between fullerenes and between a fullerene and an electrode surface were taken to be equal to 0.3 nm, which approximately corresponds to configurations stabilized by week van der Waals interactions. The molecular dynamics simulation confirms the stability of such chains. Due to polarization of fullerenes, the stability of the chains increases when an electric field is applied.

The electric current as a function of the bias voltage was calculated using the Landauer approach, which connects charge transport with the transmission of electrons [2]:

$$I = (q/h) \int_{-\infty}^{\infty} \overline{T}(E)[f_0(E - \mu_1) - f_0(E - \mu_2)]dE, \qquad (1)$$

where $f_0(E) = (\exp(E/k_B T) + 1)^{-1}$ is Fermi function, μ_1 and μ_2 are the electrochemical potentials of the electrodes, $(\mu_2 - \mu_1) = -qV$, q is the absolute value of the electron's charge, V is the bias voltage. A gap between electrodes is considered as a tunneling barrier that separates two reservoirs of electrons on each side of it, at different electrochemical potentials μ_1 and μ_2. To obtain the transmission function $\overline{T}(E)$, a supplementary problem of the electron tunneling coupled with its scattering by the fullerenes was considered based on the solution of Schrödinger equation with appropriate Hamiltonian [1]. The results of calculations show that in all the cases the current–voltage characteristics demonstrate nonmonotonic behavior and exhibit sharp jump of current followed by a region of negative differential resistance (Figs. 1 and 2).

The reason of such a behavior is that the transmission function $\overline{T}(E)$ has a peak, the position of which correlates with the energy level of the fullerene, working as a quantum dot (the resonance phenomenon). When V is increased, the peak in the $\overline{T}(E)$ is shifted to the lower values of energy because of the lowering of the resonance energy level in accordance with the lowering of the potential at the center of fullerene. The sharp jump in $I(V)$ occurs when the peak of $\overline{T}(E)$ enters the "window" of the electron's energy with nonzero contribution to the total current (as follows from formula (1)). Further increase of V leads to the decrease of the peak in $\overline{T}(E)$, because it shifts to the more low values of energy of the electron, and hence to the low probability for tunneling. That leads to the decrease in I with the increase in V.

In a case of fullerene chains this region is shifted to the higher values of the bias voltage when a chain length is increased.

Due to the specific current–voltage characteristics revealed, the fullerene-based systems, similar to the tunnel diode, can be used as active components for electronic devices.
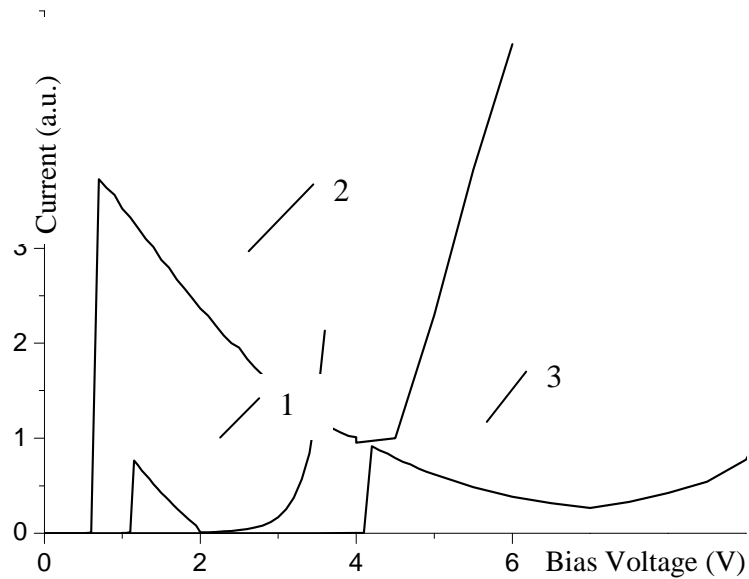

Figure 1 – Current–voltage characteristics corresponding to the different materials of the electrodes: (1) caesium, (2) magnesium, (3) chromium.
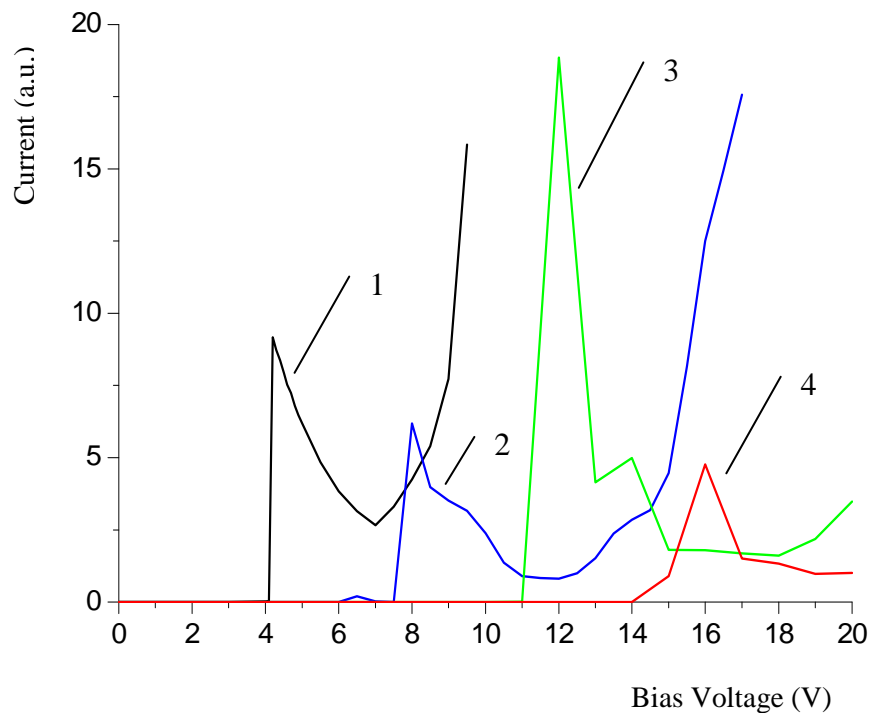

Figure 2 – (1) to (4): current–voltage characteristics corresponding to the fullerene chains consisting of 1 to 4 molecules.

REFERENCES

[1] M.A. Britch, K.V. Dobrego, L.I. Krasovskaya, "Numerical analysis of the electrical conduction in carbon nanostructures", *J. Nanophotonics*, vol. 7, 073098, Jan. 2013.
[2] S. Datta, *Quantum Transport*: *Atom to Transistor*. Cambridge University Press, Cambridge, 2005.

FEATURES CRATER MORPHOLOGY AFTER THE ACTION
OF LASER RADIATION ON THE METAL SURFACE

P. Kuznetsov, V. Feodorov
Tambov State University, Russian

Abstract – Used plates of the alloy Fe-Si. Specimens irradiating by a laser source. When a pulse of radiation during at the surface formed crater with wavy-like relief. The appearance of a periodic wavy relief on the surface of the crater is connected, and thermocapillar phenomena that arise from the dependence of surface tension on temperature.

I. INTRODUCTION

Laser treatment of various details of metal commonly used in the industry (welding, cutting, and surface marking, etc.). For example, in laser marking process of stainless steel, the corrugated surface of the workpiece becomes. Reduction such kind surface defect is not yet unsolved problem.
The aim of this work was to study the morphology features of the surface characteristics of steel 40×13 when exposed by laser radiation of varying intensity.

II. EXPERIMENTAL TECHNIQUE

We used stainless steel plate 40X13 [1] with the dimensions 30×15×0,9 mm [2]. Samples were irradiated with a laser with an active element of YAG:Nd (1,064 mkm) (free generation). The pulse energy and time influence is 3 ± 0,1 J and 3 ms, respectively. The study was carried out using noncontact optical profilometer Wyko NT 9080 (Bruker AXS, USA). All experiments were performed at room temperature with a mixture of target blowing ambient air and argon (flow rate of 5 l/min.)
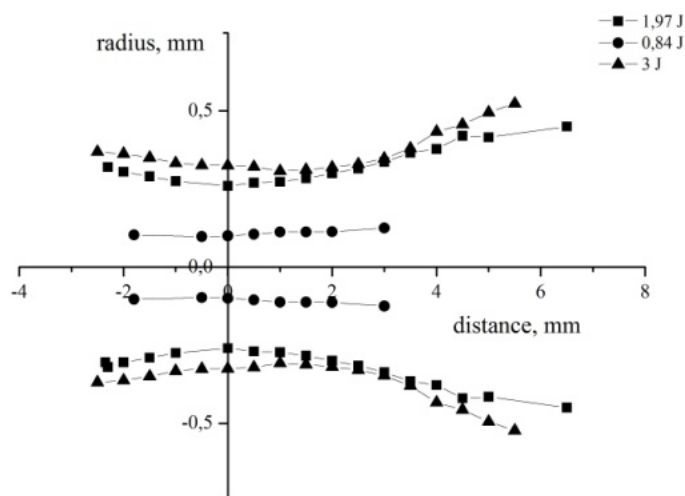

Figure 1 – Form caustics for different energies of the focused laser beam (t = 3 ms).

Calculation of power density (J) produced by the formula:

$$J = \frac{W}{\tau S},$$

where W – energy per pulse, τ – time of exposure and S – the area of the beam spot on the surface (the shape – a circle).

To vary the power density without changing the exposure time and energy radiation used caustic spatial laser beam (Fig. 1) by movement along which the radius incident beam solely changes, and hence power density (intensity) of the incident laser radiation. We used a caustic for energy 3 J.

III. RESULTS

The results are presented in Fig. 2. It is seen that by irradiating the surface with an intensity of $1,30 \cdot 10^5$ W·cm^{-2} (Fig. 2a) occurs slight melting. Besides, wavy-like relief not appears, that intensity may be regarded as a threshold for the formation of an wavy-like relief, while the crater diameter is 0,72 mm. When driving along the caustic (in the direction of reducing the diameter of the laser beam), with an increase in intensity is increased degree of fusion surface with simultaneous formation of a wavy-like relief, which is formed as a result of thermocapillary instability [2, 5]. Increased intensity above ~ $3,30 \cdot 10^5$ W·cm^{-2} leads to decrease amplitude of wavy-like relief in center by intensive removal of material target (though increase in the depth of the crater) at burning iron [2] and actions of vapors impact.

As one of characteristics of morphology of the crater was the degree of curvature surface on which can be qualitatively traced measure recoil effects of oxidation products at the surface of the molten iron during combustion. The degree of curvature of the surface varies with increasing power density. Practically all the craters (except Fig. 2a and b) the surface has a convex shape. At low intensities has a flat horizontal surface form (Fig. 2a), high - conical shape (Fig. 2g). It is also associated with the growing influence of the impact of oxidation products of the combustion of the metal.

Since, in this case, is the instability of thermocapillary convection [4], the other as a characteristic parameter of the crater morphology was spatial instability growth rate. This parameter allows us to characterize the degree of manifestation of this instability, depending on the laser power density (Fig. 3).

a)

b)

c)

d)
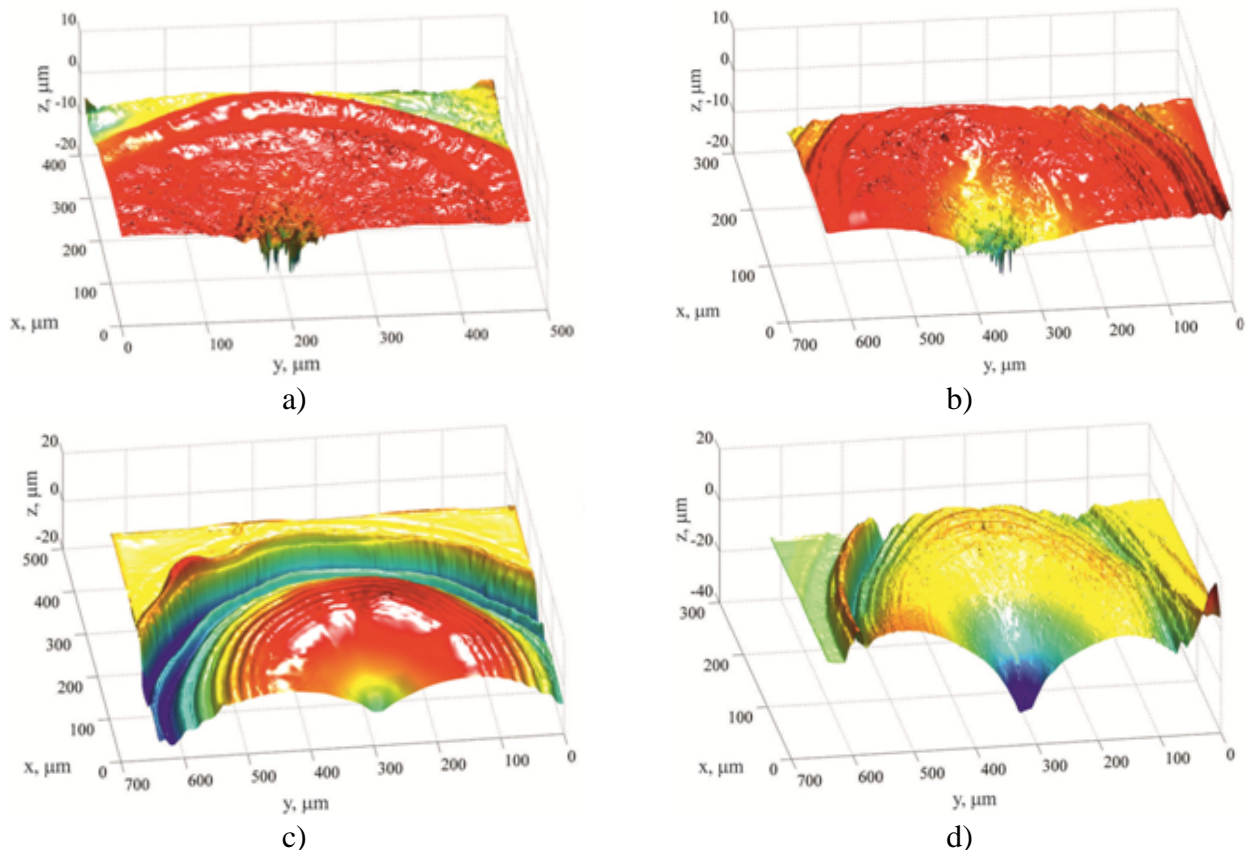
Figure 2 – View of the crater after laser irradiation with different power density on the surface of stainless steel:
a) $1,30 \cdot 10^5$ W·cm^{-2}; b) $1,70 \cdot 10^5$ W·cm^{-2}; c) $2,64 \cdot 10^5$ W·cm^{-2}; d) $3,37 \cdot 10^5$ W·cm^{-2}
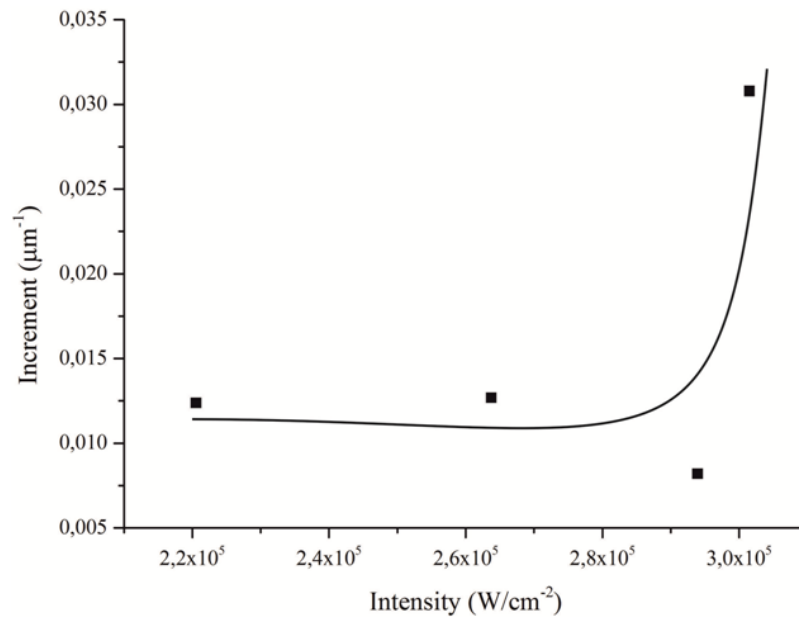
Figure 3 – The dependence of the spatial growth rate of the power density of laser radiation

As can be seen from Fig. 3 in the range of intensities of $< \sim 3 \cdot 10^5$ W·cm^{-2} spatial growth rate is nearly constant, with a small excess of the specified intensity of a sharp increase in the spatial growth rate to $\sim 0,03$ m^{-1}. Growth spatial increment occurs mainly at the periphery of the crater which yet forming a wavy-like relief (Fig. 2g). Growth spatial increment, probably, by occurs due to an increase of mass transfer from the central portion to the peripheral crater under the pressure by combustion products at a target laser irradiation.

IV. CONCLUSION

Thus, at low intensities $(1,30 \cdot 10^5$ W cm$^{-2})$ forming the wave-like relief occurs. Abrupt growth increment associated with increased mass transfer of a central crater in the peripheral portion by the pressure of the vapor impulse. Thus there is an increase in the depth of the crater, as well as the change of curvature of the convex shape on a plane inclined.

REFERENCES

[1] Steel and alloys. Database. Ed. Sorokin V. M.: Ingermet Engineering. 2001. 608 p.
[2] V.A. Fedorov, P.M. Kuznetsov, A.V. Yakovlev Formation of a relief on the surface of the alloy Fe - Si in the action of laser radiation // Chemistry and Physics of Materials Processing 2013, №1, C. 24 – 28
[3] L. Han, F.W. Liou Numerical investigation of the influence of laser beam mode on melt pool // International Journal of Heat and Mass Transfer, 47, 2004, p. 4385 – 4402
[4] Encyclopedia of Physics. Volume 3. Ed. Prokhorov A.M. M.: "Soviet encyclopedia", 1988, P. 347 – 349.
[5] Laser Materials Processing Technologies: Current Problems of basic research and applied research. Ed. Panchenko V.Y. M.: Fizmatlit, 2009, 664 p.

VISUALIZATION OF THE INTERACTION
OF NANOPARTICLES WITH BIOLOGICAL CELLS BY AFM

E. Drozd[1], M. Sudas[1], A. Salem[2], S. Chizhik[1]
[1]Heat and Mass Transfer Institute of NASBelarus, Minsk, Belarus
[2]Belarusian National Technical University, Minsk, Belarus

Abstract – In the last decade, the interest to the interaction of nanoparticles with biological cells is increased. The most promising and little studied area of nanoparticles application is medicine. Due to the unique properties nanoparticles of silver, zinc, copper and others are used against certain viruses, for the treatment of burns, destruction of tumor cells, as a part of the drugs delivering system to some organ. It is known that nanoparticles can have an impact on the functional state of the cells. One method that can be used to assess the state of the cells is an atomic force microscopy (AFM). ACM can not only visualize, but to assess the changes in the mechanical characteristics of the objects. There are many modern techniques for the visualization of biological microorganisms. Atomic force microscopy was chosen because it allows you to get a true three-dimensional surface topography and does not require complex sample preparation. Further investigation using the dynamic mode AFM allows to obtain sample microtomography. This mode allows you to automatically obtain a set of bundle AFM images of the same area at different values of the load applied to the scanning process. This study demonstrated approach for visualizing the interaction of nanoparticles with the cell and its internal structure by micromechanical destructive impact.

I. INTRODUCTION

Due to the nanomaterial's application in various fields of human activity it is necessary to study the biological effects of various nanoparticles and nanomaterials, especially their action on the human and animals organisms. The actual task is to determine the degree of nanoparticles toxicity for humans and, therefore, the potential risk of nanoparticles and medicines on their basis. For the last decade, the data about positive (therapeutic effect) and about negative (stimulation of various diseases) effects of metal nanoparticles on living organisms are accumulated. One of the most popular objects of investigation is silver nanoparticles. Mainly research works are connected with the determination of the antimicrobial activity of nanoparticles [1 – 3]. The data on the effects of silver nanoparticles (Ag) at the higher organisms are not numerous. Investigation of nanosilver toxicity, showed that cell's vitality after interaction with Ag nanoparticles depends on the cell's type, on nanoparticles size, and their concentration [4].

The purpose of this work was to visualize the nanoparticles on the cellular membrane surface. This task can be solved by the method of atomic force microscopy (AFM). This method allows to visualize the cell surface, and also to determine the way of interaction of nanoparticles with biological cells: by means of linkng of nanoparticles with a surface of the cellular membrane or by means of nanoparticles penetration into the cell – endocytosis.

II. MATERIALS AND METHODS

In this research we used the atomic force microscope "NT-206" ("MikroTestMashines" Belarus). The CSC 38 probe («MicroMash») with the curvature radius of 30 nm and console rigidity of 0.03 N/m was used in the static mode and the NSC 11 probe with the curvature radius of 30 nm and console rigidity of 3 N/m - in dynamic mode. The object of investigation is the culture cell line MDBK (bovine kidney cells), and silver nitrate nanoparticles ($AgNO_3$).

III. RESULTS

Static mode of AFM allows to visualize the surface of cell membranes and can be used as a control method of binding of the nanoparticles with the cell surface. The dynamic mode allows to reveal the objects in case of their penetration into the cell. Figure shows the cell surface with nanoparticles (Fig. 1a) scanning in contact mode and cell's surface after the cells incubation with nanoparticles (Fig. 1b).
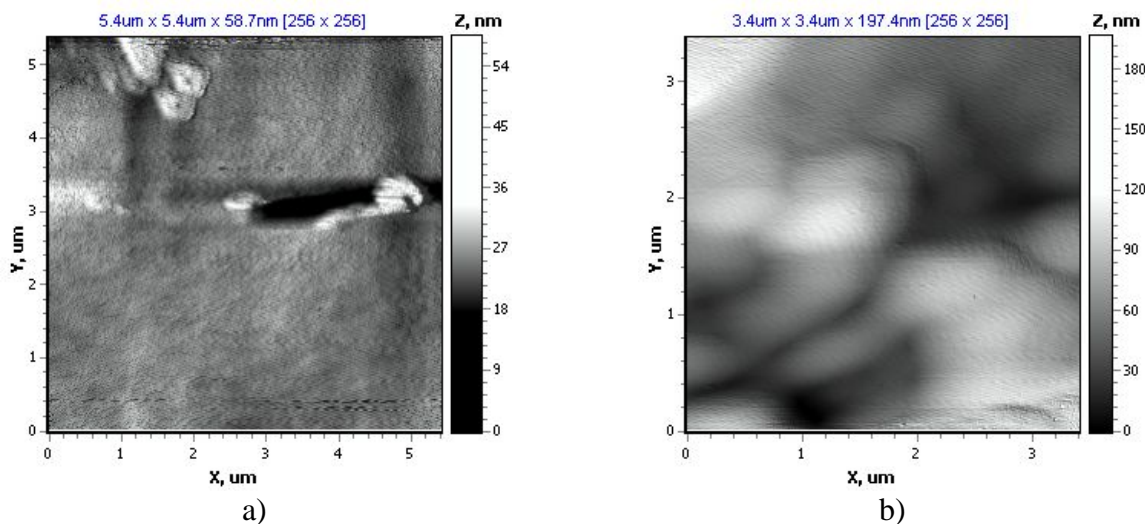
a)   b)

Figure 1 – AFM images of the surface area of the MDBK cell:
a – nanoparticles on cell's membrane – scanning area 5,4×5,4 µm;
b – cell's membrane after the cells incubation with nanoparticles – scanning area 3,4×3,4 µm

The investigations in dynamic mode were made also at different load (from 30 till 90 %). The task was to visualize the internal structure of the cell. It is established that when the load increases to 70 % of the microstructure of the cell membrane is visible more distinctly (Fig. 2 c, d).

a)   b)

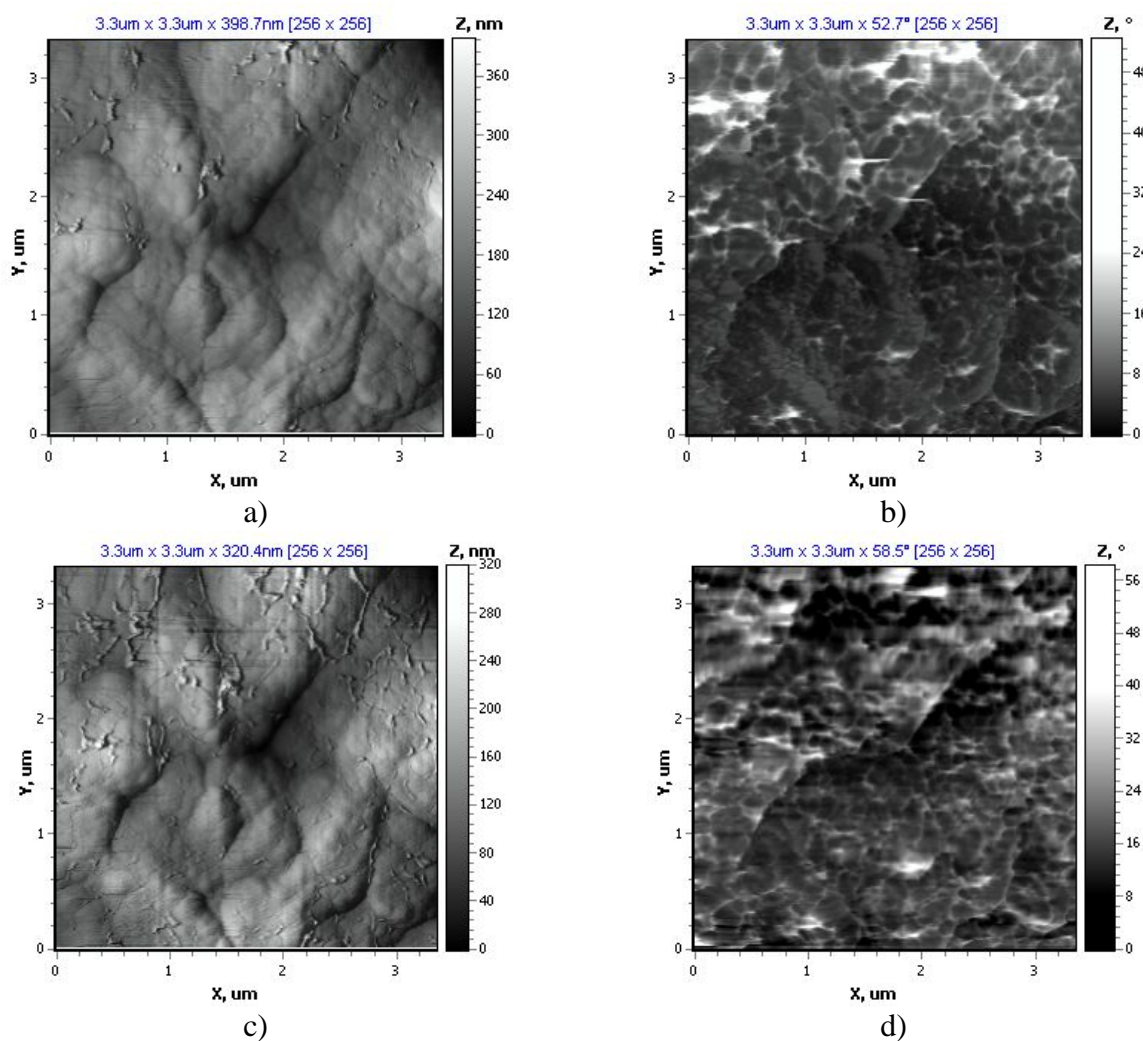c)   d)

Figure 2 – AFM images of the cell's surface: a, b – at 40% load; c, d – at 70% load;
a, c – topography of the cell surface, c, d – phase contrast image; scanning area 3,3x3,3 µm

IV. Conclusions

Thus, it is established that it is possible to define a way of interaction of nanoparticles with biological cells by atomic force microscope. Changing the load applied during the scanning proses it is possible to obtain the images of the internal structure of the cell.

References

[1] Nguyen, H.Ch. Some results in manufacturing of nanosilver and investigation of its application for disinfection / Nguyen Hoai Chau, Le Anh Bang, Ngo Quoc Buu, Tran Thi Ngoc Dung Huynh Thi Ha, Dang Viet Quang. J. Advanced // Sci. & Tech. – 2008. – C. 73-78.

[2] Oka, M. Metal-Based Drugs / M. Oka, T. Tomioka, K. Tomita et al. // Langmuir. – 1994. – № 1. – P. 511.

[3] Tran Thi Ngoc Dung Studies on manufacturing of topical wound dressings based on nanosilver producted by aqueous molecular solution method / Tran Thi Ngoc Dung, Ngo Quoc Buu, Nguyen Hoai Chau, Huynh Thi Ha et. all // J. Nanopart Res. – 208. – №7 (5). – P. 1243–1245.

[4] Thomas, J. Webster Safety of Nanoparticles / J. Thomas // Springer. – 2009. – 239 c.

ELECTROCHEMICAL CODEPOSITION OF NANOSTRUCTURED MATERIALS FOR HIGHLY RELIABLE SYSTEMS

Yu. Timoshkov[1], V. Kurmashev[2], V. Timoshkov[1], A. Sakova[1]
[1]Belarusian State University of Informatics and Radioelectronics, Minsk, Belarus
[2]Minsk Institute of Management, Belarus

Abstract – This paper describes one of the approaches to solve the problem of wear and friction of mechanically moving and load carrying elements of micro and nano dimensions. The electrochemical electroplating technology of metals and alloys with inert hard nanoparticles is presented. Codeposition model of nanocomposite plating is developed. The influence of process parameters on the mechanical properties of particle-reinforced coatings is described. The use of nanocomposite materials to improve the mechanical properties of micro and nano components in modern integrated systems is investigated. The outlook of these materials and technologies for advanced micro- and nanoelectromechanical systems of high reliability and their application is considered. A method for manufacturing of holographic films with high runability for roll-to-roll technology is described.

I. INTRODUCTION

Micro and nanosystems have become the integral part of human being. Such modern complex advanced systems and their production technologies require new types of material to be developed. These materials should be structured by shape and properties in nano and micro scale for fulfillment of requirements and further incorporation into the systems.

One of the approaches to solve the problem of wear and friction of mechanically moving and load carrying elements of micro and nano dimensions is the use of nanocomposite materials; in particular, codeposited metal and alloy with inert hard nanoparticles by electrochemical or electroless processes. The most exciting applications of plated nanostructured materials are microelectromechanical systems (MEMS), roll-to-roll and nanoimprint technologies.

II. NANOCOMPOSITE PLATING PROCESS

Nanocomposite coatings containing ultra-fine particles were plated. Soft magnetic (NiFe, CoFeP, CoP) and hard magnetic (CoNiP, CoW, CoP) alloys as well as conductive matrixes of Cu and Ni were investigated. The thickness of the investigated deposits was up to 200 µm. Concentration of ultra-fine particles was varied from 0 to 10 g•dm^{-3} (dry substance). Diamond, alumina and aluminium monohydrate ultra-fine particles and boron nitride microparticles were used. Average size of nanodiamond particles was 7 nm, alumina – 47 nm, aluminium monohydrate - 20 nm and boron nitride – 1 µm. Codeposition process was carried out in the electrolytic cell of flow type (Fig. 1).
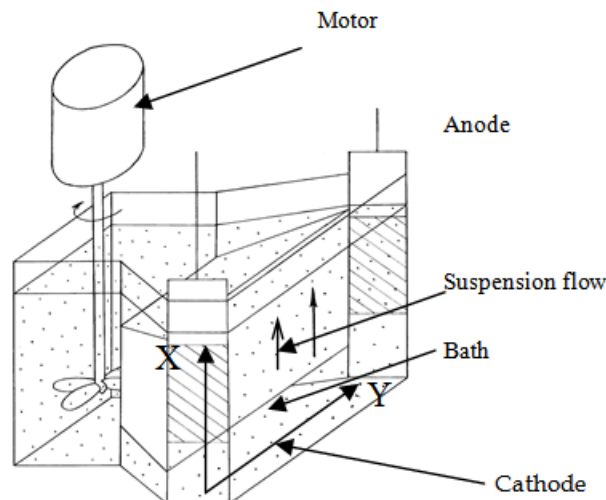

Figure 1 – Electrolytic cell for codeposition process

III. Codeposition Model of Nanocomposite Plating

During the electrolytic codeposition, the suspended inert particles interact with the surface of the growing film due to hydrodynamic, molecular and electrostatic forces [1]. This complex process results in the formation of composite coatings.

Based on the experimental data [2], the qualitative codeposition model of the composite coatings with the ultra-fine particles was suggested. The peculiarities of the ultra-fine particles behavior are considered in the model. The model worked out is based on the assumption the codeposition of ultra-fine particles proceeds through the following stages:

1. Coagulation of ultra-fine particles in plating solution;
2. Formation of quasi-stable aggregates and therefore change of system dispersion constitution;
3. Transport of the aggregates to the cathode surface by convection, migration and diffusion;
4. Disintegration of the aggregates in the near-cathode surface;
5. Weak adsorption of ultra-fine particles and aggregate fragments onto the cathode surface;
6. Strong adsorption of dispersion fraction (embedment).

Behavior of dispersed systems is described by DLVO theory. Stability or coagulation rate of suspensions depends on sign and magnitude of overall potential energy of interaction between the particles. Structural investigations confirm proposed model of heterogeneous nanocomposite coating formation. Cross-sections show that ultra-fine particles are effectively incorporated into the meal matrix (Fig.2). These nanoparticles are distributed in the matrix volume uniformly. Small fragments of aggregates and separate nanoparticles form heterogeneous structure of nanocomposite.
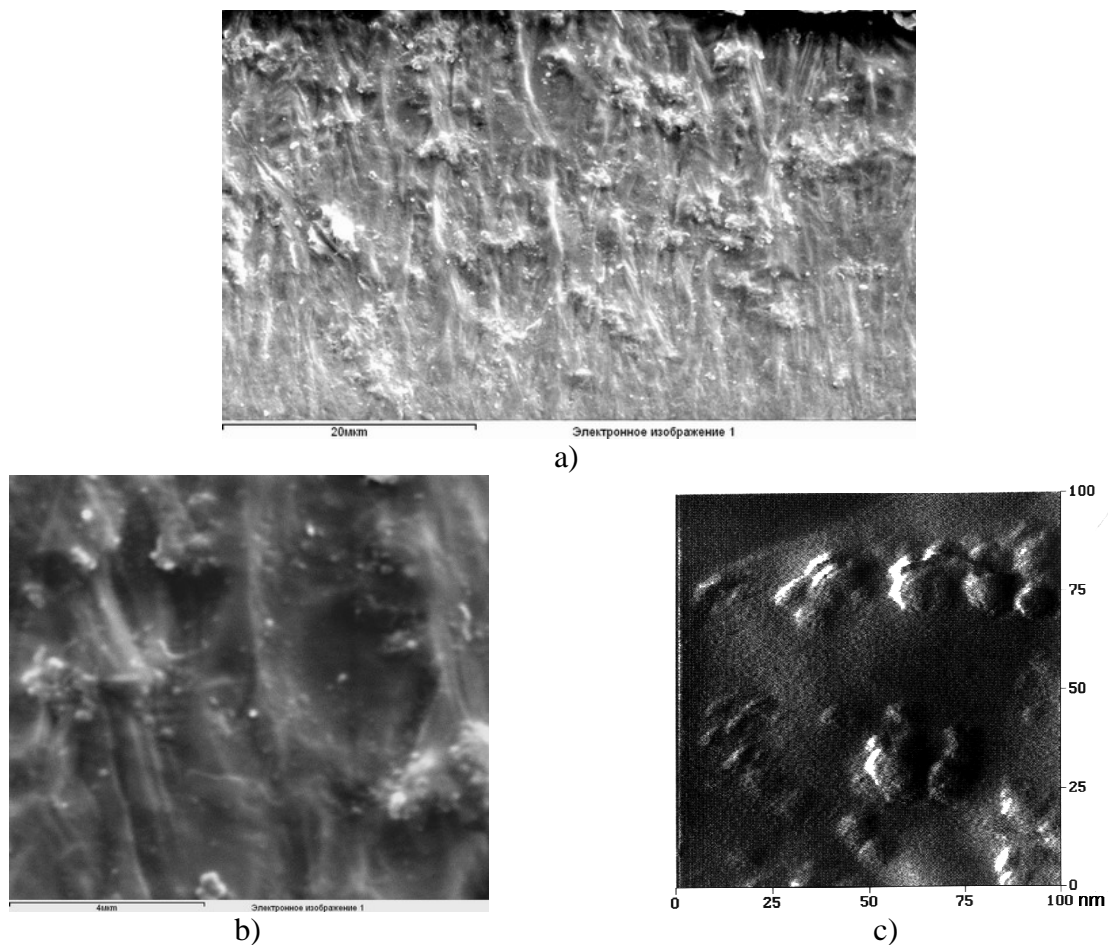
a)

b)   c)

Figure 2 – SEM cross sectional images of Ni-Al$_2$O$_3$ nanocomposite film (a, b),
AFM surface image of Ni-nanodiamond (c)

IV. NANOCOMPOSITES FOR HIGHLY RELIABLE APPLICATIONS

Micro and nanosystems are the completed devices that combine into one sensor, electronic, and mechanical parts. Mechanical interaction between nano-, micro-, and macro world is the limiting factor for such a complex system. Three dimensional moveable structures should be integrated in micro and nanosystems from design and technology perspective. Moreover, in general reliability of the systems is determined by the reliability of the mechanical part.

Friction, wear and corrosion are the key problems for MEMS with real mechanically moveable elements. Codeposition processes allow getting nanocomposite elements with high operate reliability: wear resistance increased in 2-2.5 times, microhardness increased in 2 times, coefficient of friction and corrosion current were reduced factor 1.5 and 1.6 respectively. Developed technologies were tested on prototypes of the electromagnetic and pneumatic micromotors (Fig. 3).
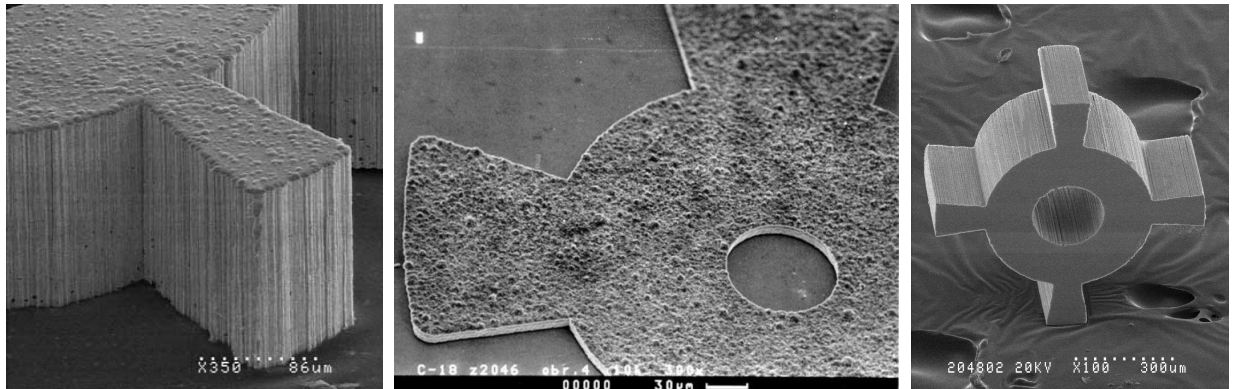

Figure 3 – Nanocomposite MEMS elements

Codeposition of thin composite coatings to improve the tribological properties of the contacting surfaces during roll-to-roll processing and nanoimprint lithography (NIL) is one of the most effective ways to achieve higher performance characteristics of devices. Another way is fully composite electrochemical foils with the one-side matrix profile to enhance the runability of working holographic matrixes.

Working nanocomposite nickel matrix was developed, as well as composite chromium protective coating deposited with nanodiamond particles on top of pure nickel matrix (Fig. 4).
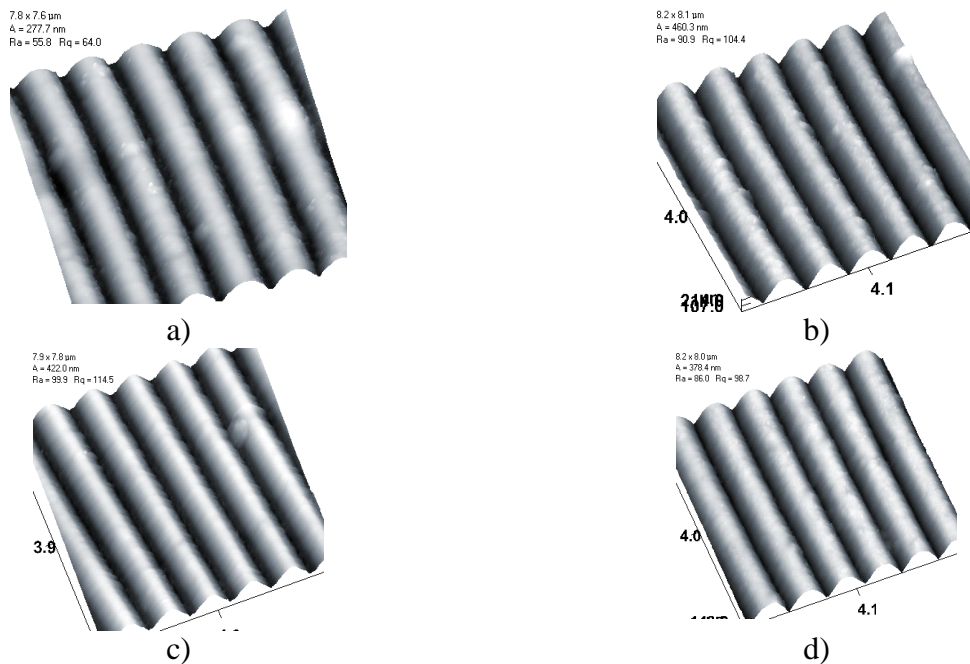

Figure 4 – AFM images of test nanocomposite samples of copies:
a – pure Ni, b – Ni with Al$_2$O$_3$, c – Ni with diamond particles, d – Ni with aluminum monohydrate

Test results show the increase of holographic matrixes runability on 60-400% with improved printed image quality.

Application of composite materials in NIL and roll-to-roll process is the right way to solve issues and improve reliability of templates and whole technology at all.

V. Conclusion

This paper describes positive consequences of introduction of the nanocomposites in the advanced technologies. Application of nanocomposites in MEMS, NEMS, NIL and roll-to-roll technologies makes it possible to improve quality and reliability of these processes and end products. Nanocomposite technology may be integrated in the systems technology by replacement of homogeneous pure materials by heterogeneous nanocomposites. This allows to improve set of physical mechanical properties, such as wear resistance, microhardness, corrosion resistance and friction coefficient. Nanocrystalline structure of nanocomposites enables to resolve sub-100nm features in MEMS, NEMS, NIL, and other advanced applications.

References

[1] Fransaer, J.; Celis, J-P. and Roos, J.R. Analysis of the electrolytic codeposition of non-Brownian particles with metals, *Journal of The Electrochemical Society*, 139 (2), 1992, pp. 413 -425.

[2] Timoshkov, Yu.; Gubarevich, T.; Orekhovskaya, T.; Molchan, I. and Kurmashev V. Properties of Ni-composite coating with different type of ultra-dispersed diamond particles, *Galvanotechnique and surface technologies*, v.7, 2, 1999, pp. 20-26, Russia.

SIMULATION OF IMPACT IONIZATION PROCESS
IN DEEP SUBMICRON N-CHANNEL MOSFETS

V. Borzdov, A. Borzdov, D. Speransky, D. Pozdnyakov
Belarusian State University, Minsk, Belarus

Abstract – The ensemble Monte Carlo simulation of deep submicron silicon MOSFET with 50 nm channel length is performed. The effective threshold energy of impact ionization process in the MOSFET is calculated in the framework of Keldysh model.

I. INTRODUCTION

It is known that in numerical simulations of integrated circuit elements with the reduction of their dimensions, particularly deep submicron MOSFETs, an account of impact ionization process is essential. The latter is caused by the fact that the rate of impact ionization in such elements can be comparable or even greater than the rates of other considered scattering processes as a result of the presence of high electric field strengths [1, 2]. The main purpose of this study is the estimation of effective threshold energy in deep submicron silicon n-channel MOSFET with 50 nm channel length in the framework of Keldysh impact ionization model.

II. SIMULATION MODEL AND RESULTS

The considered MOSFET structure is presented in Fig. 1. The MOSFET dimensions are denoted in the same figure. Other parameters used in the simulation are the following: gate oxide thickness is 10 nm, acceptor doping levels of the channel and substrate are equal to $5 \cdot 10^{23}$ m^{-3} and 10^{24} m^{-3}, donor doping level of the source and drain regions is equal to 10^{25} m^{-3}. The calculations are performed for the temperature $T = 300$ K.
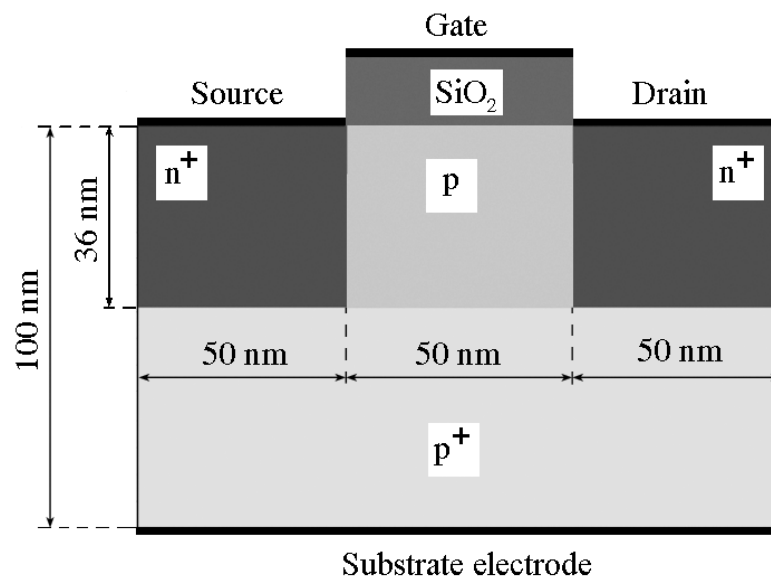

Figure 1 – The cross-section of the simulated silicon n-channel MOSFET

Electron transport simulation in silicon conduction band is performed in the framework of the effective mass approximation and includes X and L valleys with account of nonparabolicity of the dispersion relation. Electron scattering processes are intravalley and intervalley phonon scattering, ionized impurity scattering, plasmon scattering and impact ionization process [1–4]. Hole transport in valence band is simulated in the effective mass approximation in heavy, light and split-off bands. Scattering mechanisms for holes are phonon and ionized impurity scatterings. Nonparabolicity and anisotropy are taken into account [5–7]. The electrostatic potential and electric field strength are found via the solution of a corresponding two-dimensional Poisson equation which is self-consistently

incorporated into the Monte Carlo transport simulation. Source, drain and substrate electrodes are modeled as ideal ohmic contacts and metal gate is supposed to be aluminum.

To calculate the effective threshold energy of impact ionization process in the n-channel MOSFET the process was included into Monte-Carlo simulation as additional scattering mechanism. In the framework of Keldysh impact ionization model its scattering rate $W_{II}(E)$ is expressed by so-called Keldysh formula with given threshold energy E_{th} [8]

$$W_{II}\left(E\right) = A W_{ph}\left(E_{th}\right)\left(\frac{E - E_{th}}{E_{th}}\right)^2 , \qquad (1)$$

where E is electron energy, A is a fitting parameter, $W_{ph}(E_{th})$ is the total electron-phonon scattering rate at the energy equal to E_{th}. Thus the model has two fitting parameters A and E_{th} with $E_{th} = 1.2$ eV for "soft" and $E_{th} = 1.8$ eV for "hard" thresholds.

The effect of impact ionization process on some characteristics of a deep submicron MOSFET for both "soft" and "hard" threshold models was studied, particularly, in [9] but holes were treated in quasi-equilibrium approximation. In present simulation we used a "soft" threshold model with $A = 0.38$ [10].

The dependence of the effective threshold energy E_{theff} versus the drain voltage V_D for several gate biases V_G for the simulated MOSFET are presented in Fig. 2. As it can be seen, it is possible to conclude that the effective threshold voltage has nearly linear dependence on the drain voltage for gate biases in the range from 1 to 1,4 V. The dependence can be approximated as

$$E_{theff} = 0,22 V_D + 0,98 \quad [eV]. \qquad (2)$$

At rather high drain biases ($V_D > 3$ V) when high electric field ($> 5 \cdot 10^7$ V/m) exists in the transistor channel, the effective threshold energy for "soft" threshold model saturates at approximately 1,7 eV [9]. The obtained results are in a reasonable agreement with the results of [11] where the effective threshold energy was calculated in bulk silicon for uniform electric field with the strength of $5 \cdot 10^7$ V/m.
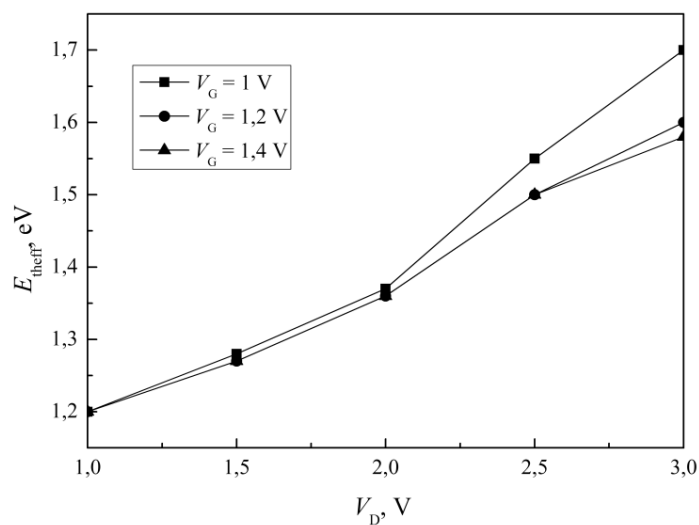

Figure 2 – The effective threshold energy in the channel of the MOSFET

III. CONCLUSION

In this paper the effective threshold energy of impact ionization process in deep submicron n-channel MOSFET was calculated in the framework of Keldysh "soft" threshold model. The results of

the simulation show the possibility of the use of one fitting parameter *A* in the description of impact ionization process. Threshold energy is *a priory* known and can be approximated by linear dependence versus the drain voltage.

REFERENCES

[1] J. Y. Tang, K. Hess, "Impact ionization of electrons in silicon (steady state)," *J. Appl. Phys.*, vol. 54, pp.5139-5144, 1983.

[2] V. Borzdov, F. Komarov, O. Zhevnyak, V. Galenchik, D. Pozdnyakov, A. Borzdov, "Calculation of secondary charge carrier current in submicron channel MOSFETs at stress regimes of operation," *Proc SPIE*, vol. 6260, pp.62601E-1-62601E-8, 2006.

[3] C. Jacoboni and P. Lugly, *The Monte Carlo Method for Semiconductor Device Simulation.* Wien–New York: Springer-Verlag, 1989.

[4] E. Pop, R. W. Dutton, K. Goodson, "Analytic band Monte Carlo model for electron transport in Si including acoustic and optical phonon dispersion," *J. Appl. Phys.*, vol. 96, pp.4998-5005, 2004.

[5] S. Rodrigues-Bolivar, F. M. Gomez-Campos, J. E. Carceller, "Simple analytical valence band structure including warping and non-parabolicity to investigate hole transport in Si and Ge," *Semicond. Sci. Technol.*, vol. 20, pp.16-22, 2005.

[6] S. Rodrigues-Bolivar, F. M. Gomez-Campos, F. Gamiz, J. E. Carceller, "Implications of nonparabolicity, warping, and inelastic phonon scattering on hole transport in pure Si and Ge within the effective mass framework // *J. Appl. Phys.*, vol. 97, pp.013702-1-013702-10, 2005.

[7] F. M. Gomez-Campos, S. Rodrigues-Bolivar, J. E. Carceller, "An efficient Monte Carlo procedure for studying hole transport in doped semiconductors," *J. Comp. Electron.*, vol. 3, pp.329-332, 2004.

[8] L. V. Keldysh, "Concerning the Theory of Impact Ionization in Semiconductors," *Soviet Physics JETP*, vol. 21, pp. 1135-1144, 1965.

[9] D. Speransky, A. Borzdov, V. Borzdov, "Impact ionization process in deep submicron MOSFET," *Int. J. of Microelectronics and Computer Science*, vol. 3, pp.21-24, 2012.

[10] [B. K. Ridley. "Soft-threshold lucky drift theory of impact ionization in semiconductors," *Semicond. Sci. Technol.*, vol. 2, pp.116-122, 1987.

[11] N. Sano, M. Tomizawa, A. Yoshii, "Monte Carlo analysis of ionization threshold in Si," *Appl. Phys. Lett.*, vol. 56, pp.653-655, 1990.

CONCEPT OF NEW COMPACT MODEL
OF DEEP-SUBMICRON MOSFET

V. Nelayev, *Tran Tuan Trung*
Belarusian State University of Informatics and Radioelectronics, *Minsk*, *Belarus*

Abstract – Concept of new compact model for the simulation of deep submicron (DSM), nanometer-scale MOFFET transistor characteristics is presented. The proposed model is based on the use of traditional "compact" submicron MOSFET device model. Parameters of this model are verified by means of fitting procedure to results obtained by use exact physical models taking into account quantum effects accompanying charge carriers transfer in DSM MOSFET.

I. INTRODUCTION

In microelectronic today, difficulties of integrated circuit and technology design are rising; integrated circuit complexity is increasing; die areas are also getting larger in order to incorporate the increasing of functionality… Integrated circuit design in micro- and nanoelectronics is based on the solution of complex problem of charge carriers transport simulation in the device structure. The problem is becoming even more acute in design of deep submicron (DSM), below 0.13 um, where quantum-mechanical effects and accompanying leakage currents have to be taking into account.

Obviously, how consistently the physical effects have described in a certain model will determine how adequate the object/process simulation results will be compared to their real behavior. But the more exact the physical model is, the more strict mathematical methods (mostly numerical) are used for its implementation, and the more sophisticated and bulky computer facilities will be required for calculation.

There is a well-proved approach in microelectronics to reduce the necessary computing resources without the need to sacrifice the essential simulation accuracy, especially SPICE-like package. The essence of this approach is in replacing exact physical models by so-called compact models [1]. The basic feature of the compact models, as usually, is the use of polynomials instead of integral-differential equations, describing the processes under study. The coefficients of the polynomial series are "extracted" using the response-surface methodology, RSM from a limited amount of computer calculations based on the exact physical models or from full-scale experiments, employing specific "design of experiments" (DOE methodology [2]).

In this work authors propose an approach for calculation the I-V characteristics of deep submicron, nanometer MOS transistors, based on use of generalized compact model. The proposed new compact model was proved by using the Silvaco package [3], intended for technology and device design of microelectronic products.

II. COMPACT MODEL FOR DEEP SUBMICRON MOS-FET. METHODOLOGY

The problem of parameter extraction of device models used in program complex Silvaco, can be reduced to the task of the conditional optimization. That procedure is in seeking of the minimum extent of discrepancy between the result calculated with exact physical model and compact model approach, where the model parameters appear as the appropriate factors.

The physical models of semiconductor devices are described by system of equations (1), which link the electrostatic potential ψ with the carriers density ρ

$$\left. \begin{array}{l} div(\varepsilon \nabla \psi) = -\rho, \\ \vec{E} = \nabla \psi, \\ \dfrac{\partial n}{\partial t} = \dfrac{1}{q} div(\vec{J}_n) + G_n - R_n, \\ \dfrac{\partial p}{\partial t} = \dfrac{1}{q} div(\vec{J}_p) + G_p - R_p, \end{array} \right\} . \tag{1}$$

To determine carrier density, the charge transport equations are use. The simplest charge transfer model for the calculation of I-V device characteristics is the drift-diffusion (DD) model, described by drift-diffusion equations (2):

$$\left.\begin{array}{l} \vec{J}_n = qn\mu_n\vec{E}_n + qD_n\nabla n \\ \vec{J}_p = qp\mu_p\vec{E}_p - qD_p\nabla p \end{array}\right\}.\tag{2}$$

Until recently, the drift-diffusion model was adequate for nearly all devices that were technologically feasible. The drift-diffusion approximation, however, becomes less accurate for smaller feature sizes. More advanced models taking into account quantum effects in deep submicron devices are needed. Such models were developed in the frame of Silvaco package. They are Energy Balance and Hydrodynamic models. Silvaco package supplies both drift-diffusion and advanced transport models. Beside Silvaco models more advanced models also support, which are accounting for quantum effects, to supply simulation of nanoscale devices, for example, Monte-Carlo methodology.

Differences between results of simulation in Silvaco DD model both Monte-Carlo calculations and experiment in sub-micron (0.25 μm) and deep sub-micron (0.1 μm) MOS transistor are shown in Fig. 1 [4].
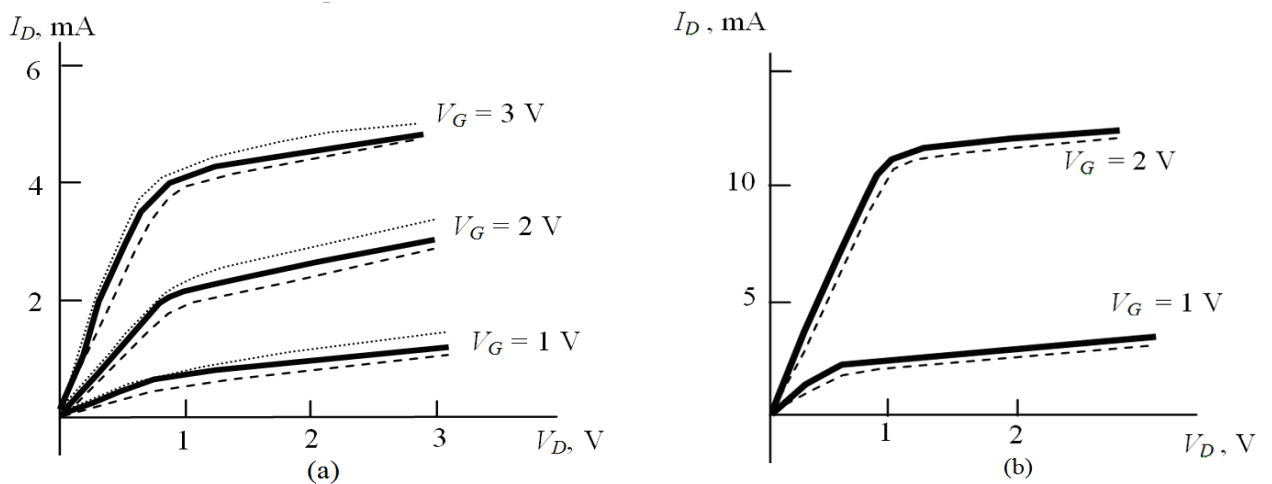

Figure 1 – The dependencies drain current - drain voltage (I_D vs V_D) of MOS transistor
(a) 250 nm and (b) 100 nm channel length: solid – experiment; dashed – Monte Carlo (MC) simulation; dotted – Silvaco simulation result

In DD models the carrier mobility is the main factor influenced on the transport process of the charge carriers in the MOSFET structure. We proved in the frame of the carrier mobility Darwish model [5] that only some parameters of the carrier mobility model affect on the I-V characteristics of MOS structures stronger in comparison with others. Such parameters (so called "significant" parameters) are calculated with use screening experiments by means of design of experiment methodology [6]. Our results, presented in Fig. 2, show a wide change of I-V characteristics MOSFET (~ 3.5 times) while parameters of mobility Darwish model are only varied 20% from their default values. That fact illustrates the possibility of proposeв compact model to describe I-V features of deep submicron MOS transistor.
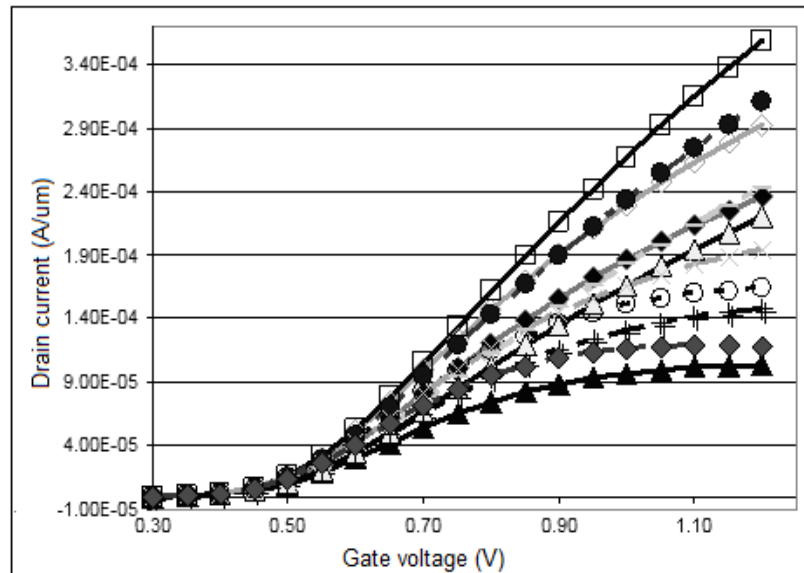
Figure 2 – I-V characteristics of 100nm MOSFET with various combinations
of parameters from Darwish mobility model

III. Conclusion

Concept of new compact model for simulation of deep submicron MOS I-V characteristics is described. The methodology is based on traditional ideology of compact models. The new model could apply into all device simulation frameworks which include traditional drift-diffusion model of charge carriers for DSM-device simulation.

Acknowledgment

References

[1] Denisenko V., *Compact MOS transistor models for SPICE in micro- and nanoelectronics* / Moscow, Fizmatlit, 2010. 407 p.

[2] Kouleshoff A., Malyshev V., Nelayev V., and Stempitsky V. "Statistical design and optimization of integrated circuits manufacturing", *Russian J. Microelectronics*, 2003. vol. 32. No. 31. pp. 47–61.

[3] http://www.Silvaco.com

[4] Belous A., Nelayev V., Shvedov S., Stempitsky V., Tuan Trung Tran, Turtsevich A., "Compact DSM MOSFET model and its parameters extraction," Proc. of the Int. Symposium East-West Design Testing (EWDTS'2011), Ukraine, 2011, pp. 230–232.

[5] Darwish M. "An improved electron and hole mobility model for genenal purpose device simulation," *IEEE Trans. on Electron. Dev.* 1997, vol. 44, № 09, pp.1529–1538.

[6] Stempitsky V. Verification of significant parameters in the deep-submicron MOS-FET simulation / Stempitsky V., Tran Tuan Trung, Borovik A. // Proc. of The XII Int. Conf. The Experience of Designing and Application of CAD Systems in Microelectronics (CADSM'2013), Ukraine.– 2013.– P. 351–354.

THE NEGATIVE DIFFERENTIAL RESISTANCE IN FERROMAGNET/ WIDE-GAP SEMICONDUCTOR/ FERROMAGNET NANOSTRUCTURE

T. Sidorova, A. Danilyuk

Belarusian State University of Informatics and Radioelectronics, Minsk, Belarus

Abstract – The model of charge carrier transport in ferromagnet/wide-gap semiconductor/ ferromagnet nanostructure based on two-band Franc-Keine model and phase function method was proposed. It is calculated, that tunneling barrier, formed by the wide-gap semiconductor band-gap, does not represent potential step, but the energy band-gap. Their upper border is the bottom of the conduction band E_C, and the bottom part is top of the valence band E_V. Inside this zone wave vector of the electron is an imaginary value. According to the dispersion law states located in the midgap sustain the largest attenuation. That is why when the Fermi level of the analyzed structure lies in the bottom part of the band-gap, bias voltage V shifts levels of the tunneling electrons to the low barrier area. This shifting is a reason of the tunneling current reduction and leads to the negative differential resistance effect. It is shown that areas of the negative differential resistance effect appears at the current-voltage bias dependence in case of $qV > E_F$. Here areas of negative differential resistance should be expected at the voltage values bigger than Fermi energy value of the emitting electrode for the electrons zone with the spin-up.

I. INTRODUCTION

Ferromagnet /wide-gap semiconductor/ ferromagnet nanostructures attract a great interest during the last decade regarding their prospects for creating information-processing devices, including spintronic devices. Previously, the tunneling magnetoresistance (TMR) in such nanostructures was calculated generally using one-band insulator model.

In this article the charge carrier transport model in the ferromagnet / wide-gap semiconductor/ feromagnet based on two-band Franc-Keine model and phase function model is proposed [1]. It is taken into account, than tunneling barrier with the width *d*, which was founded by the band gap, does not represent potential step, but the energy band-gap. Their upper border is the bottom of the conduction band E_C, and the bottom part is top of the valence band E_V. Inside this area the wave vector of the electron is an imaginary value. According to the Franc-Keine law it is defined as [2]

$$k_z^2 = \frac{2m_i}{h^2} \frac{(E - Ec)(E - E_V)}{E_G} - k_p^2, \tag{1}$$

where k_z, k_p – are wave vector components which are perpendicular and parallel to the barrier, correspondingly, E – is a full electron energy, m_i – the electron effective mass, E_G - is the band-gap width.

The current value is calculated taking into account the transverse component of the tuning electron energy based on the transport equation:

$$I(V) = \frac{4\pi \cdot m_i q}{h^3} \int_0^\infty dE[f_L(E) - f_R(E,V)] \int_0^{(m/m_i)E} dE_p P(E, E_p, V), \tag{2}$$

where E_p – is an electron energy component which is parallel to the tunneling barrier surface, m and m_i – are the electron effective masses in electrode and in the wide-gap semiconductor correspondingly, q – is an electron charge, h – is the Planck constant, $f_L(E)$, $f_S(E)$ – are the Fermi-Dirac distribution functions for left and right electrodes, $P(E, E_p, V)$ – tunnel transparency of the barrier.

II. MODEL

To find the transmission coefficients we develop a model on the basis of phase functions. The model accounts for the barrier parameters, the image force potential and allows include the potential relief at the interfaces and in the volume of the wide-gap semiconductor. The main feature of the phase function is possibility to obtain the transmission coefficients. For In the phase function method not a wave function, but only its changes as a result of potential actions are calculated.

To evaluate the spin dependent transmission coefficient we solve the Schrödinger equation for each spin component:

$$\left[-\frac{\hbar^2}{2m_\sigma^*}\frac{\partial^2}{\partial z^2}+\frac{\hbar^2 k_p^2}{2m_\sigma^*}+U_0-h_0\sigma-qV(z)-q\varphi(z)+V_{sc}(z)\right]\psi_\sigma(z)=E\psi_\sigma(z),$$

(3)

where z is a coordinate of the tunneling direction; σ – is the spin index (spin –up and spin-down); V_{sc} – is the scattering potential. Effective potential in this case is equal to:

$$U_{eff}=\left(2m_\sigma^*/\hbar^2\right)\left(U_0+k_\parallel^2-qV(z)-q\varphi(z)\pm V_{sc}(z)\right).$$

(4)

The tunneling transmission coefficient is:

$$T_\sigma=\exp\left[\frac{1}{k_\sigma}\int_0^d U_{eff}(z)\left[b_\sigma(z)\cos(2k_\sigma z)-a_\sigma(z)\sin(2k_\sigma z)\right]dz\right],$$

(5)

where a_σ and b_σ functions are defined by the equations based on the Phase function method:

$$\frac{da_\sigma(z)}{dz}=\frac{U_{eff}(z)}{2k_\sigma}\left[-\sin(2k_\sigma z)-2b_\sigma+(a_\sigma^2-b_\sigma^2)\sin(2k_\sigma z)-2a_\sigma b_\sigma\cos(2k_\sigma z)\right],$$

(6)

$$\frac{db_\sigma(z)}{dz}=\frac{U_{eff}(z)}{2k_\sigma}\left[\cos(2k_\sigma z)+2a_\sigma+(a_\sigma^2-b_\sigma^2)\cos(2k_\sigma z)-2a_\sigma b_\sigma\sin(2k_\sigma z)\right].$$

(7)

Using system of equations (2), (5), (6), (7) current-voltage characteristics are calculated in dependence from position of Fermi level. We considered the cases when Fermi level of nanostructure is located close to valence band maximum or conduction band minimum.

III. RESULTS AND DISCUSSIONS

The dependence of tunneling current on the voltage applied to the transition for the case when E_F is located above the midgap is expected to be monotonically increasing function (Fig.1). But when E_F is situated below the midgap an additional canal through the valence band of the wide-gap semiconductor can appear. Current density of the main canal monotonically increases (Fig.1). Current density of the additional canal (Fig.2) for the applied voltage of 0.1 V…3 V increases monotonically, but at the further increasing of the applied voltage up to the 5 V the maximum appears, after which the tunneling current decreases. It means that the region of the negative differential resistance is formed. The smaller is the thickness of the wide-gap semiconductor d, the larger is effect of the negative differential resistance.
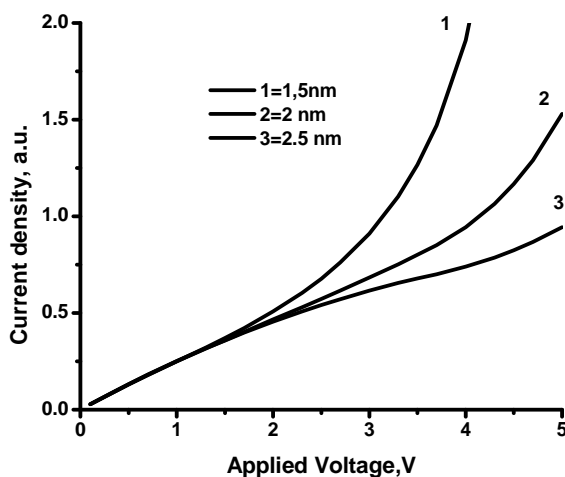

Figure 1 – Current –voltage characteristic
of the main canal in dependence of the thickness
of the wide-gap semiconductor for the case when E_F
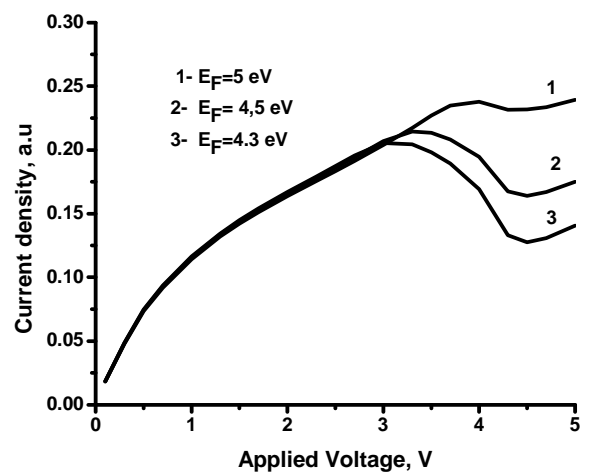is situated below the midgap.

Figure 2 – Current –voltage characteristic
of the additional canal in dependence
of the Fermi level position, for the case when E_F
is situated below the midgap

Thereby when Fermi level E_F of the nanostructure is situated below the midgap on the dependence of the tunneling current from the applied V for the case when $qV > E_F$, the regions of the negative differential resistance appear, that can be explained by the appearance of the additional canal of the charge carrier transport through the valence band. [2]. According to the dispersion law (1) states located in the midgap sustain the largest attenuation in the barrier. Therefore if Fermi level of the observed nanostructure is located near the bottom of the band-gap the bias voltage V shifts the levels of the tunneling electrons to the area of the lower barrier transparence. This shifting is a reason of the tunneling current decrease, which is the reason of the effect of the negative differential conductivity.

The tunneling magnetoresistance of the ferromagnet /wide-gap semiconductor/ ferromagnet nanostructures taking into account the appearance of the additional canal of the transport through the valence band of the wide-gap semiconductor was calculated. TMR of the main canal monotonically decrease from 0.15 up to 0.3 (Fig.3), but for the additional canal TMR changes insignificantly (Fig. 4).
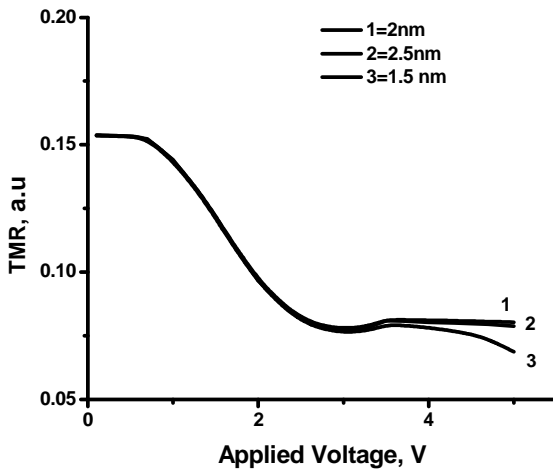

Figure 3: TMR of the main canal in dependence of the wide-gap semiconductor thickness for the case when E_F is situated above the midgap
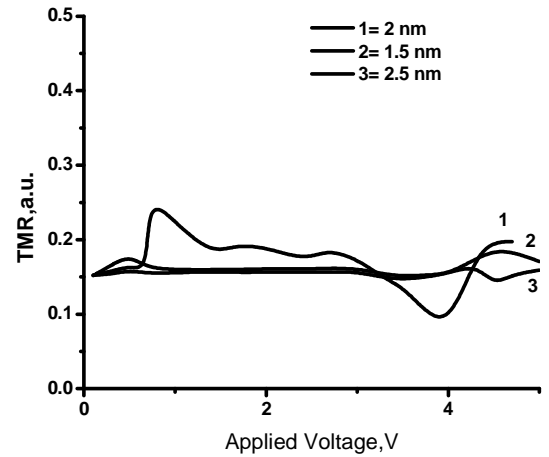
Figure 4. TMR of the additional canal in dependence of the wide-gap semiconductor thickness for the case when E_F is situated above the midgap

For the wide-gap semiconductor thickness equal to 1.5 nm and 2.5 nm the TMR of the additional canal is almost constant. For the intermediate thickness equal to 2 nm two extrema are observed at the TMR curve of the additional canal for the voltage bias equal to 1 V (0.25) and 4 V – 4.3 V (0.1). These extrema can be explained with the availability of the maximum correlation between minimal and maximal value on the current-voltage characteristic in the region of the negative differential resistance at this considered thickness.

<div style="text-align:center">REFERENCES</div>

[1] V. V. Babikov. Phase Function Method in the Quantum Mechanics (Nauka, Moscow, 1976) - in Russian.
[2] T. A. Kchachaturova, A. I. Kchachaturov, The negative differential resistance of metal/ insulator/ metal structure, JETF, 2008

ELECTROCHEMICAL ALUMINA TECHNOLOGY FOR HIGH-BRIGHTNESS LED APPLICATIONS

V. Sokol, G. Litvinovich, V. Yakovtseva
Belarusian State University of Informatics and Radioelectronics, Minsk, Belarus

Abstract – High temperatures near light-emitting regions are common for high-brightness LED systems. The cooling problem for these devices can be solved only by effective heat sink from the light-emitting region to the cooler environment. We propose the most effective heat sink for the high-brightness LED systems fabricated on the anodized aluminum substrates. 30 – 50 µm thick nanostructured alumina layer formed by the electrochemical alumina technology offers good electrical isolation and excellent thermal transfer. Copper conductors are applied to the alumina layer and light-emitting diodes are mounted directly on the surface. This approach allows the most important heat resistance component, i.e. a dielectric substrate, to be excluded. As a result, the record low heat resistance is reached and the heat sink is more efficient. So, the electrochemical alumina technology allows the heat sink problems that were considered as an insurmountable obstacle to be solved.

I. INTRODUCTION

Recently light-emitting diodes (LED) progressively replace incandescent lamps. High brightness and long life are characteristic of modern LED illuminating equipment. Today leading companies produce commercially LED lights. They find an application for street lighting, signaling and transport illumination engineering. If take into consideration a spread of automated bonding technologies, high-brightness LEDs fabricated for the surface mounting (surface-mountable devices – SMD) are the most promising.

High temperatures near light-emitting regions are common for high-brightness LED systems. Heating from external source including direct sun rays is added to the heat dissipated by high-brightness LEDs themselves. As is well known, LED radiation intensity falls sharply as temperature increases and is halved when temperature increases to 70 – 90ºC relative to the room temperature. Saying by the language of solid-state physics, a role of nonradiative carrier recombination increases, and Saying by the language of engineering, a coefficient of efficiency decreases. In addition, high temperature results in the LED quick degradation. Until recent times this problem was not solved in full measure. Evident advantages of LED systems in comparison with incandescent lamps force producers to limit LED temperature requirements up to 85°C. However, real-life environment may be much more severe. For example, if LED is placed in the closed passenger compartment and affected with direct sun rays, temperature near the light-emitting region may be as high as 100 – 120°C.

II. RESULTS AND DISCUSSION

The LED cooling problem may be solved only by the effective heat sink from the light-emitting region to the cooler environment. The substrate utilized is a key component of the power and thermal management scheme. The current study focused on the electrochemical alumina technology (ELAT) for the substrate fabrication [1-2] to provide the most effective heat sink. The technology includes in succession the following basic operations: (i) aluminum surface finish, (ii) aluminum anodization, (iii) metal deposition, (iv) metal patterning, (v) LED mounting.

The 30 – 50 µm thick dielectric alumina layers are formed in the 10% aqueous solution of the oxalic acid by the high-speed porous anodization [2] at the constant current densities 100 – 150 mA/cm^2 at 20ºC. In this case the anodization rate is 5 – 10 µm/min to allow the alumina layer of the desired thickness to be grown for 5 – 10 min. Electrophysical parameters of the alumina films fabricated are: a breakdown voltage is more than 1 kV, a heat resistance of the 50 µm thick alumina layer is $6.25 \cdot 10^{-6}$ m$^2 \cdot$K/W.

One interesting characteristic of the ELAT technology is the capability of forming solderable conductors directly onto heat sinks thereby simplifying the assembly of power systems. A 1.5 µm thick nickel layer is deposited chemically on the dielectric alumina layer. Then the surface sensitizing is performed in the 5% solution of SnCl$_2$ in 5% HCl for 2 min at the room temperature with further surface activation in 1% solution of PdCl$_2$ in 5% HCl for 1 min at the room temperature. Next, the

activated substrate is cleaned and subjected to the electroless nickel plating in the aqueous solution consisted of boric acid (15 g/l), lactic acid (17 g/l), caustic soda (19 g/l), sodium hypophosphate (20 g/l), nickel sulfate (25 g/l),and thiourea (0.1 g/l). The process temperature is 95ºC, the deposition time is 10 min. the deposited film is heat treated at 200ºC for 1 hour.

A 30 µm thick conducting copper layer is formed on the nickel surface by the electrochemical deposition in the electrolyte consisted of copper sulfate (210 g/l), sulfuric acid (75 g/l), ethyl alcohol (10 g/l), urotropin (0.2 g/l) at the current density 20 mA/cm^2 at 23ºC.

Then the Ni-Cu metal layers are patterned by the conventional photolithography to form needed interconnection pattern. The layers are etched layer-by-layer. Copper is etched in the $FeCl_3 \cdot 6H_2O$ solution, nickel is etched in the $HNO_3:H_2O$ diluted solution.

At last, high-brightness LEDs are mounted directly on the substrate surface.

Fig. 1 shows a high-brightness LED system formed on the anodized aluminum heat sink. The 50 µm thick dielectric alumina layer is formed on the flat aluminum surface, 30 µm thick copper metallization is formed at the anodized surface, and 40 LEDs (1 W power, 32 V supply voltage, and 1.5 A maximum current) were mounted.

For the successful application of anodic alumina some problems should be solved. Among them are: (i) an assurance of the alumina thermal stability in the range from -60ºC to +300ºC taking into account that the linear expansion coefficient of aluminum is 4 times higher than that of alumina; (ii) removal of the pore influence on the breakdown voltage relative to the substrate, leakage currents and insulation resistance; (iii) an assurance of the time stability of these parameters.

Figure 1 – High-brightness LED system on the anodized aluminum heat sink

To improve the thermal stability, a cyclic anodization regime is proposed. The voltage or current in every next cycle is taken to be more or less by 10 – 20%. Such cycles should be more than two. In the last cycle the voltage is set to be maximum possible for the taken anodization conditions. Time of every cycle should be more than 3 min. A porous alumina reconfiguration takes place at such the anodization regime because it is well-known that number of pores per the surface unit and pore diameter is directly proportional to the anodization voltage. So, when the voltage of the next cycle increases or decreases relative to the previous cycle, the porous alumina reconfiguration happens and any transition spongy layer arises. Number of such layers is equal to number of cycles, resulting in the thermal stability improvement. The anodization process should be finished with the maximum possible anodization voltage because of stresses at the alumina/aluminum interface. A tension stress appears in the alumina film while a compression stress appears in the aluminum due to difference in the coefficients of thermal expansion. Aluminum becomes plastically deformed near the alumina/aluminum interface due to the dislocation movement from grain boundary into the aluminum grain. By the way, so the structure of porous alumina is independent of the aluminum grain size. The elastically deformed aluminum zone appears else after the plastically deformed aluminum zone. Width of these zones is directly proportional to the diameter of the alumina pores at the above interface. Wider zones are, higher the thermal stability of alumina is. Thus, the cyclic anodization regime allows providing the desired alumina thermal resistance in the above-mentioned temperature range.

There is no doubt that pores in the alumina layer should be effectively filled with dielectric either completely or partially to provide the time stability of alumina parameters. To close pores, we use the Al_2O_3 or SiO_2 vacuum deposition.

III. CONCLUSION

We offer the most effective heat sink for the high-brightness LED systems fabricated on the anodized aluminum substrates. ELAT substrates consist of a highly thermally conductive aluminum alloy substrate with the anodic aluminum oxide layer electrochemically grown on the aluminum core. This anodized layer shows good electrical isolation (breakdown voltage no less than 1 kV) and excellent thermal transfer.

Since no organic materials are used, there is no degradation of properties during operation at high temperatures. The completely inorganic construction results in substrate characteristics that maintain their properties even at high continuous operating temperatures.

One interesting characteristic of this technology is the capability of forming solderable conductors directly onto heat sinks, thereby simplifying the assembly of power systems. The 30 µm thick copper layer is deposited electrochemically onto the anodized substrate. Because conductors can be applied directly to heat sinks, a wide range of circuit configurations are possible.

Traditional methods of removing excess heat from components have centered on the use of heat sinks with thermal grease or polymer pads to thermally connect the device to the heat sink. With the ELAT substrates, the entire board becomes the heat sink with no extra hardware (clips, screws, etc) required. In addition, copper conductors allow direct wire bonding from dice to the conductors. So, the electrochemical alumina technology allows the heat sink problems that were considered as an insurmountable obstacle to be solved.

REFERENCES

[1] V. A. Sokol, *Anodic alumina*. Minsk, Belarus: Bestprint, 2011, 431 p.
[2] V. A. Sokol, "Extremal high-speed technique for the thick porous alumina film formation," *Doklady of the BSUIR*., No. 8, pp.84-88, 2010.

DEVICE AND TECHNOLOGY SIMULATION OF IGBT ON SOI STRUCTURE

I. Lovshenko[1], V. Nelayev[1], A. Belous[2], A. Turtsevich[2]
[1]*Belarusian State University of Informatics and Radioelectronics, Minsk, Belarus*
[2]*R&D Center "BelMicroSystems" of Joint Stock Company "Integral", Minsk, Belarus*

Abstract – Static and dynamics characteristics of the power IGBT device at "Silicon-On-Insulate" structure were simulated. Analysis of the characteristics of such structure in comparison with the IGBT at the bulk silicon are presented. Advantages of IGBT device at SOI are revealed.

I. INTRODUCTION

At present two base types of power electronics contemporary devices are dominant: field transistors (Metal Oxide Silicon Field Effect Transistor, MOSFET) and bipolar transistors with the isolated gate (Isolated Gate Bipolar Transistor, IGBT), as well as various integrated structures on their basis. The numerous requirements to the power electronic systems (low losses during switches, small voltage drop in the activated state, high resistance in the off-state, high efficiency, etc.) stimulate researches for the new design structures, fabrication technologies, materials of the structural elements of such devices and layouts. IGBT due to its exceptional functional features, combining the positive properties of power field and bipolar transistors, is a widely applied power device and finds a wide application in the devices of the electric thrust and AC motors, induction heating systems, radiological systems, power back-up sources, switching elements. Perfecting of the IGBT structures is oriented at enhancing the efficiency, limit commutating currents and voltages.

II. TECHNOLOGY «SILICON–ON-INSULATOR»

The technology «Silicon–On-Insulator» (SOI) was elaborated specifically to obtain the devices of the high temperature electronics and applications, requiring resistance to influence of the hard radioactive irradiation. In the structures "silicon-on-insulator" the working layer of silicon is separated from the substrate by means of the dielectric isolating layer of silicon oxide.
The SOI technology resolves a number of problems, emerging in the structures on the bulk silicon at high temperatures. The essence of technology is essentially in the complementary oxygen implantation into the silicon substrate with formation of the dielectric layer of silicon oxide inside the semiconductor.

The SOI structures are distinguished for their high radiation resistance and enhanced reliability at high temperatures. The short channel effects in the SOI devices can be suppressed by a mere reduction of the silicon layer thickness. The tilt of the above threshold characteristic of the SOI transistors is derived practically ideal. The high quality transistors are attained on the silicon films 8 nm thick.

For the SOI structures three methods of isolation are used: local silicon oxidation (LOCOS), isolation by means of shallow trenches (STI) and meza-isolation. The LOCOS – isolation is hard to use with the design rules of less than 0,25 µm due to the «bird's beak», which limits the potentialities of obtaining the small area isolating regions. The STI–isolation is a relatively expensive process.

III. SIMULATED STRUCTURE

Earlier there had been conducted researches devoted to investigation of the static and dynamic IGBT features dependence on the technology parameters at manufacturing of IGBT structure in bulk silicon. Thickness of the epitaxial layer of such structure was selected to be equal to 141 µm, and thickness of the p^+–collector layer – 17 µm, as in work [1].

From the entire variety of the possible IGBT structures on SOI, described in the literature [2-6] the IGBT structure was selected, represented in Figure 1, a.

The transistor base is essentially the silicon film, located on the isolation material. IGBT may possess any polarity: a bipolar transistor of the pnp-type with n-MOS transistor or a bipolar transistor

of the npn-type with a p-MOS transistor. A greater current density in the IGBT structures is attained by means of the formed n-well of the source, increasing the base current of the bipolar transistor in IGBT. The gates can control one or two channels of the MOS transistors. The vertical sizes of the n-type of the drift area are augmented to enhance the current density without growth of the voltage drop value in the n-drift region.

Simulation of the technology flow of the IGBT on SOI structure manufacturing was performed using the SILVACO package [7] in compliance with the last trends in the IGBT on SOI technology [8-9].
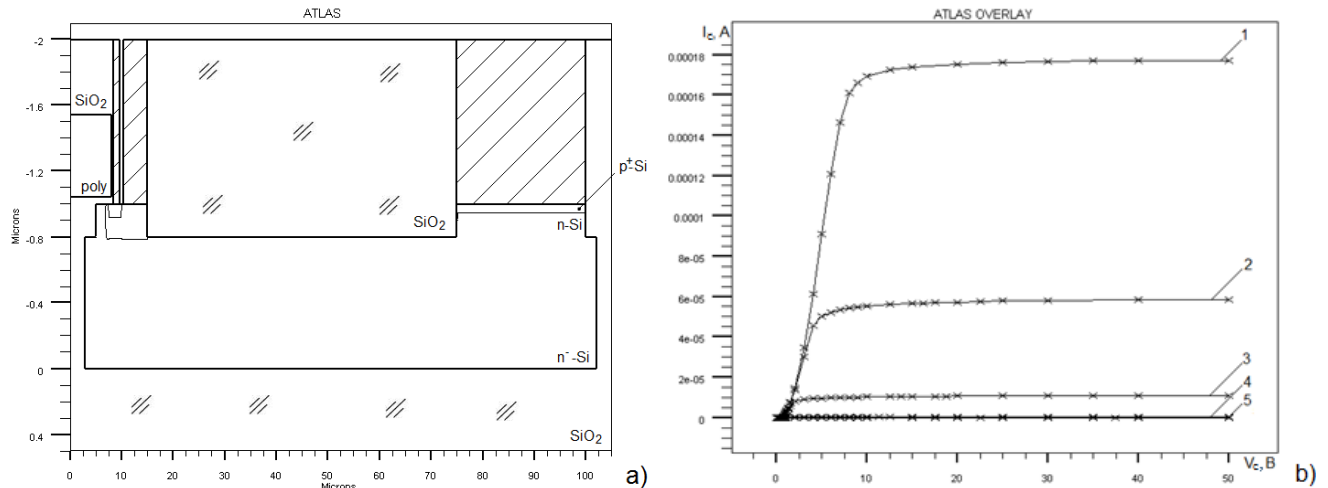

Figure 1 – Structure of the IGBT on the SOI (a) and Dependences of collector current I_c on collector voltage V_c for the structures with various h_{ox}: 1 – h_{ox}=30 nm; 2 – h_{ox}=40 nm; 3 – h_{ox}=50 nm; 4 – h_{ox}=60 nm; 5 – h_{ox}=70 nm

IV. RESULTS

The I-V features were obtained with the various thickness values of the gate h_{ox} (Figure 1, b). The thickness was varied within the limits from 30 to 70 nm.

Thickness of the gate oxide exerts a significant influence on the electric parameters of IGBT on SOI. With reduction of the oxide thickness from 40 nm down to 30 nm the bipolar transistor base current is increased and, thus, the saturation current value of the collector is increased (from ≈ 55 µA to ≈ 175 µA). Meanwhile, the switch-on time for the both IGBT structures stays equal to 25 ns, and the switch-off time rises from 55 ns for h_{ox}=40 nm to the value of 75 ns h_{ox}=30 nm.

The calculated values of the switch-on and switch -off durations are by an order smaller (25 ns and 75 ns for IGBT on SOI structure and 350 ns and 870 ns for the IGBT on the bulk silicon respectively), Withal the current value of the collector (30 µA) is greater by an order than for the vertical IGBT structure on the basis of the bulk silicon (4 µA).

V. CONCLUSION

Results of the technology design for the manufacturing of the bipolar transistor with the isolated gate (IGBT) at the "Silicon On Insulator" and at the bulk silicon structures [10] are presented. Comparisons of I-V features and dynamic characteristics (switch-on and switch-off durations) for both device constructions were carried out. on whose basis optimization was carried out of the design-process parameters on an example of such a parameter, as thickness of the gate oxide. It was shown, that thickness of the gate oxide exerts a substantial influence on the IGBT electric parameters. With reduction of the oxide thickness h_{ox} from 40 nm down to 30 nm the base current of the bipolar transistor increases and, thus, the saturation current value of the collector rises (from ≈ 55 µA to ≈ 175 µA). Meanwhile, the switch-on time for the both IGBT structures stays equal to 25 ns, and the switch-off time is increased from from 55 ns for h_{ox}=40 nm to the value of 75 ns for h_{ox}=30 nm.

REFERENCES

[1] Khanna V.K. The Insulated Gate Bipolar Transistor IGBT. Theory and Design / The Institute of Electrical and Electronics Engineers.– 2003.– 544 pp.

[2] United States Patent No. US 2010/0032713 A1. Lateral insulated gate bipolar transistor - Texas instruments inc. / Hideaki Kawahara, Philip Leland Hower: Texas instruments Inc. – Published date 11.02.2010.

[3] United States Patent No. 7,943,957 B2. Lateral SOI semiconductor devices and manufacturing method thereof / Masato Taki [et al.]: Toyota Jidosha Kabushiki Kaisha. – Published date 17.05.2011.

[4] United States Patent No.5,241,210. High breakdown voltage semiconductor device / Akio Nakagawa [et al.] : Kabushiki Kaisha Toshiba – No 2004/0207031; Prior publication date 21.10.2004; Published date 31.08.1993.

[5] Lu, L. Modeling of IGBT Resistive and Inductive Turn-On Behavior / L. Lu [et al.] // IEEE Industry Applications. - Hong Kong : Kowloon, 2008. - P. 904-914.

[6] Lu, L. Physical modeling of forward conduction in IGBTs and diodes / L. Lu [et al.] // IEEE Industry Applications. - Hong Kong : Kowloon, 2005. – P. 2635-2642.

[7] *http://silvaco.com*

[8] Pesic, I. Integrated Simulation Solution for Advanced Power Devices.

[9] Celler, G. Smart Cut. A guide to the technology, the process, the products / G. Celler, M. Wolf. - SOITEC, 2003.

[10] Belous A., Lovshenko I., Nelayev V., Shelibak I., Turtsevich A. High breakdown voltage and switching speed IGBT design. / Proc. 38th Euromicro Conference on Software Engineering Advanced Applications, SEEA'2012 and 15th Euromicro Conference on Digital System Design – Architectures, Methods and Tools, DSD'2012.- P. 19-20.

RELATIVE HUMIDITY SENSORS BASED ON FREE NANOSTRUCTURED AL$_2$O$_3$ MEMBRANES WITH OPEN-ENDED PORES

D. Shimanovich

Belarusian State University of Informatics and Radioelectronics, Minsk, Belarus

Abstract – Volumetric-surface variants of vertical direction capacitive MDM (metal-dielectric-metal) structures based on high-ordered matrices of free anodic porous alumina membranes for applications in relative humidity sensing elements were designed. The improved humidity sensitivity (4 pF/%), reduced response time and recovery time over a wide humidity range were obtained due to preparing of 30-70 μm thickness nanostructured alumina membranes with open-ended and widened pores (up to 90 nm) without the barrier layer. A special combined method composed of the smooth slow voltage drop at the final stage of the two-stage anodization with the cathode polarization and with the alumina chemical etching was developed to thin and remove the barrier layer. Such the technological approach allowed us to eliminate the effect of electrolyte anions embedded in pore walls of Al$_2$O$_3$ membranes for humidity sensing elements during the adsorption and desorption processes.

I. INTRODUCTION

Nanostructured anodic porous alumina can be used as an active humidity sensing element in the humidity sensors [1, 2] because the electrochemical process allows the capillary nanochannels to be formed and their geometrical parameters (diameter and length) to be varied. Anodic porous alumina membranes both with a dense alumina barrier layer at the pore bottoms and without this layer with open-ended pores [3] can be used as starting material to design various humidity sensors. The structural parameters determine sensitivity of nanoporous alumina to the humidity variation. These parameters are controlled by the electrolyte composition and electrical and temperature formation regimes. Conductive electrodes are possible to be formed either on one or both sides of the alumina membranes resulting in the fabrication of vertical or horizontal (interdigitated) capacitive relative humidity (RH) sensing structures.

II. RESULTS AND DISCUSSION

The test sensing elements designed for the humidity sensors based on nanoporous alumina membranes are the volumetric-surface variants of capacitive MDM (metal-dielectric-metal) structures of the vertical direction (Fig. 1). To improve humidity sensitivity, reduce response time and recovery time of the test sensing elements designed, we use free membranes based on the high-ordered matrices of anodic nanoporous alumina with open-ended pores without the barrier layer.
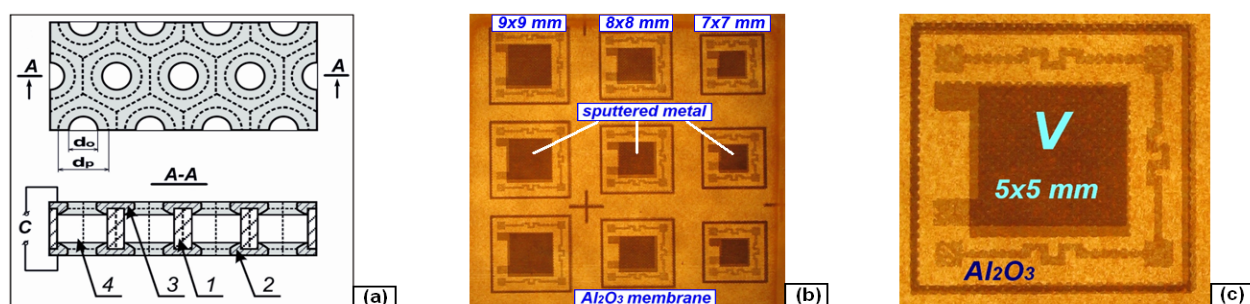

Figure 1 – Design of volumetric-surface capacitive MDM test structures of humidity sensing elements: (a) schematic explanation (d$_p$ is pore diameter; d$_o$ is a pore opening after the metal films sputtering; (1) is a free membrane based on anodic nanoporous alumina without the barrier layer; (2) and (3) are bottom and top permeable conducting plates not occluding pore entrances; (4) are open-ended pores); (b) image of test structures (9×9, 8×8, 7×7 mm) (alumina membrane thickness is 50 μm; pore diameters are 70 nm; V electrodes thickness is 100 nm); (c) image of a single element (V plates size is 5×5 mm)

Such membranes were formed by the two-stage electrochemical anodization in the 5% H$_2$C$_2$O$_4$ solution at the potentiostatic regime (45, 50, and 55 V) with the use of the barrier layer thinning

method by the slow voltage drop to 5 V at the final anodization stage combined with the cathode polarization either in the 0.5M $H_2C_2O_4$ or in the neutral 0.5M KCl solution at (-4) V for 21, 24, 27, 30, and 35 min for the alumina thicknesses of 30, 40, 50, 60, and 70 μm correspondingly and with the alumina chemical etching in 5% H_3PO_4 for 5-45 min at 25-30 °C. Such the technology allows obtaining high uniformity of pore sizes (50-90 nm) and eliminating the effect of electrolyte anions (O^{2-}, OH^-, and $C_2O_4^{2-}$) embedded in pore walls on the adsorption processes due to the decrease of the embedded anions concentration at the chemical etching.

Humidity permeable counter electrodes from the both sides of membranes formed by the metal (V, Ti, Ta, Mo) films sputtering 50-200 nm in thickness were used as the conducting electrodes of the MDM structures. The metal films thicknesses were shown by the simulation to be not more than 3-4 d_p to provide alumina matrices with open-ended pores.

Fig. 2 shows a dependence of sensing elements capacity on relative humidity (RH) at the RH increase from 10% to 90% and at the reverse RH decrease to the recovery of initial values (Fig. 2 (a)) and also a comparative analysis of the effect of the alumina structure parameters on the humidity sensors capacity at the RH variation (Fig. 2 (b)). Minimum values of the MDM nanostructures capacity are shown to be 22-35 pF at RH ~10% and amount to 370-390 pF at RH ~90%, i.e. the sensitivity of the humidity sensors is more than 4 pF per %. This indicates a high sensitivity index to allow signal digitizing at the electronic signal-conditioning circuit. Moreover, as Fig. 2 (a) shows, hysteresis value does not exceed 20 pF.
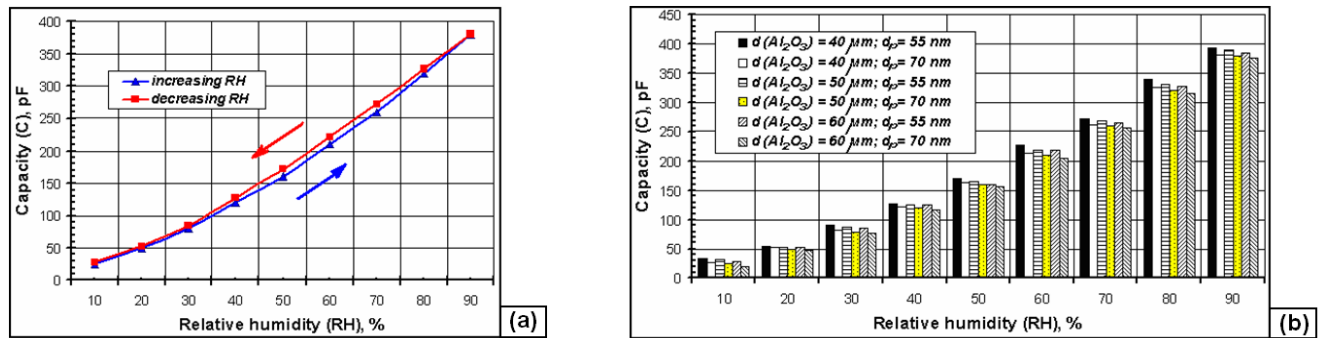

Figure 2 – Dependences of sensing elements capacity on relative humidity: (a) alumina film thickness is 50 μm; pore diameters are 70 nm; (b) a comparative analysis of the effect of the alumina structure parameters on the humidity sensors capacity at the RH variation

Fig. 3 (a) represents the comparative experimental values for the response (t_{res}) and recovery (t_{rec}) time during the adsorption process at the RH increase and the desorption process at the RH decrease for the sensing element (7×7 mm) based on the alumina free membrane 50 μm in thickness and 70 nm in pore diameters. Fig. 3 (b) shows a comparative analysis of kinetic dependences of sensing elements capacity during two cycles for different membranes thicknesses (60, 50, 40 μm). Humidity permeable counter electrodes from the both sides of membranes were formed by the Ti films sputtering 150 nm in thickness and Mo films sputtering 120 nm in thickness correspondingly. Kinetic testing procedures demonstrate that response time values are from 12 to 37 sec and recovery time data are from 3 to 8 sec during the RH increase from 10% to 30, 50, 60, 70, 90% and the RH decrease from 30, 50, 60, 70, 90% to 10% correspondingly (Fig. 3 (a)), and t_{res} are 41, 36, 32 sec and t_{rec} are 11, 9, 7 sec during the RH increase from 10 to 90% and the RH decrease from 90 to 10% for different membranes thicknesses correspondingly (Fig. 3 (b)). Observed recovery time values are much shorter than response time data.
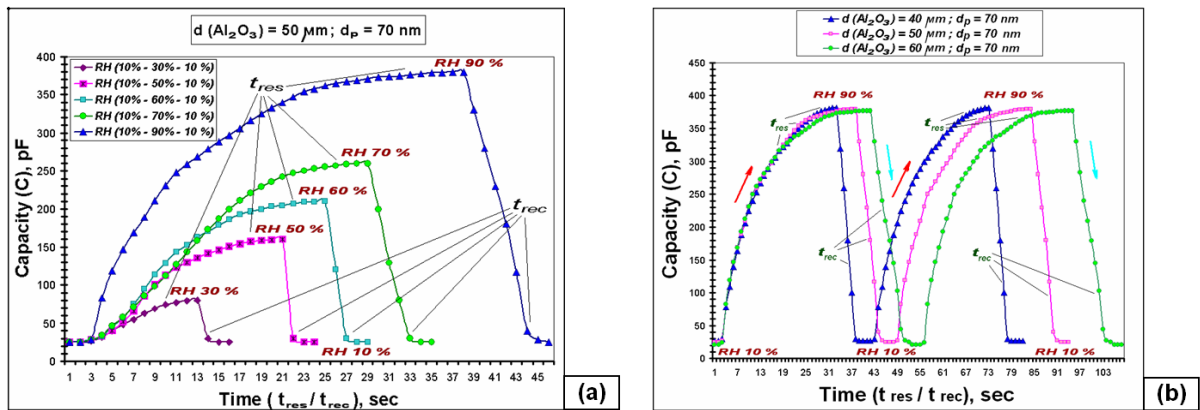
Figure 3 – Kinetic dependences of sensing elements capacity during the adsorption and desorption processes: (a) t_{res} is during the RH increase from 10% to 30, 50, 60, 70, 90%; t_{rec} is during the RH decrease from 30, 50, 60, 70, 90% to 10% (alumina free membrane thickness is 50 μm; pore diameters are 70 nm); (b) t_{res} is during the RH increase (two cycles) from 10 to 90%; t_{rec} is during the RH decrease (two cycles) from 90 to 10% (alumina free membranes thicknesses are 40, 50, 60 μm; pore diameters are 70 nm)

III. CONCLUSION

Thus, the improved humidity sensitivity, reduced response and recovery time over a wide humidity range were obtained due to preparing and using of alumina membranes of thicknesses from 30 to 70 μm without the barrier layer with open-ended and widened pores from 50 to 90 nm in diameters. Such technology allows to eliminate the effect of electrolyte anions (O^{2-}, OH^-, and $C_2O_4^{2-}$) embedded in pore walls on the adsorption and desorption processes in humidity sensing elements due to the decrease of the embedded anions concentration at the chemical etching and to improve the performance of humidity sensors.

REFERENCES

[1] L. Juhasz, J. Mizsei, "A simple humidity sensor with thin film porous alumina and integrated heating," *Procedia Engineering*, vol. 5, 2010, pp. 701-704.

[2] V. A. Sokol, V. A. Yakovtseva, and D. L. Shimanovich, "Application features of porous alumina," *Doklady BGUIR*, № 2 (64), 2012, pp. 21-27.

[3] V. A. Sokol, D. L. Shimanovich, V. A. Jakovceva, and D. I. Chushkova, "Electrochemical methods for free nanostructured films of anodic alumina with open-ended pores," in 3*rd Int. Scientific Conf. STRANN* 2012, Saint Petersburg, Russia, 10-12 Oct. 2012, pp. 118-120.

SCREENING DESIGN AND DEVICE/TECHNOLOGY DEEP-SUBMICRON MOSFET SIMULATION

Tran Tuan Trung, A. Borovik, V. Stempitsky
Belarusian State University of Informatics and Radioelectronics, Minsk, Belarus

Abstract – The problem concerned to the verification of the significant parameters of the compact deep-submicron MOS-FET model was investigated in the presented work. The screening experiments methodology is used for the extraction of the significant parameters from the entire set of the model parameters.

I. INTRODUCTION

Compact models intended for the simulation of the microelectronic devices features are the most popular now. Correspondence to the real structural and technological parameters is the main their peculiarity. Compact models with their corresponding Spice parameters are well developed today and provide adequate results for the experimental submicron (>0.13 µm) devices. However, for the deep submicron (< 0.13 µm) MOSFETs ordinary compact model based on the drift-diffusion approximation is not suitable because they do not take into account quantum confinement, ballistic or quasi-ballistic transport, gate tunneling current, etc. Thus it has become necessary to develop a new compact model for deep submicron devices and related devices with such adjustable parameters. The verification process is based on the methods of optimization of physical parameters of the device models derived from experimental data. Thus, the first stage of solving this problem is identification of the most significant parameters of the model. Presented work is devoted to the solution of this problem using screening computer experiment methodology.

II. METHODOLOGIES AND RESULTS

Among main modern simulation means, Silvaco software package is the modern and convenient tool for the physically adequate technology and device design in microelectronics. The presented results were obtained with use modules ATHENA, technology simulation, ATLAS [1], device simulation on the base of diffusion-drift approximations intended for submicron MOSFET, and QUANTUM, device simulation using various models and taking into account quantum effects during charge carriers transfer through the deep submicron device structure.

The problem of identify the most significant parameters of the transport model we solved using screening designs methodology. Screening designs are economical experimental plans that focus on determining the relative significance of many main effects. If design has more than 5 factors, fractional factorial or Plackett-Burman designs are used in order to reduce the number of experiments. As compared with fractional factor design, Placket-Burman (PB) design is more economical with the run number a multiple of four. PB designs are very efficient screening designs when only main effects are of interest [2]. The PB design in 36 runs, for example, may be used for an experiment containing up to 35 factors.

For screening experiments, all factors are varied between up and low level [3]. Those levels are chosen from desired consideration with concrete values. Design of experiments describes the combination of levels in experiments. Planning conditions of PB design are numbers of up and low levels in the each column must be equal, and sum of products of the elements belonging to the same experiment is equal to zero for any two columns.

After computer experiments were performed, results are handled to measure effect of the factors in responses. Main effect of a factor is the difference in the response when this factor is at its up level as opposed to its low level.

The parameters of Darwish model was investigated in this work. Darwish model is physically-based, semi-empirical, local model for transverse-field dependent electron and hole mobility. The model accounts for the functional dependence of surface roughness limited mobility on the inversion charge density, in addition to coulomb screening effects of impurities by charge carriers [4]. Darwish Model Number factors available for variation in Silvaco, equal 33.

TABLE 1 – The results of screening experiments

Channel length	The most significant parameters to influence the threshold voltage	The most significant parameters to influence the drain current
20 nm	AN.CVT, S1.KLA, MUMINN.KLA, ALPHA1N.KLA	AN.CVT, DN.CVT, ALPHA1N.KLA, MUMINN.KLA
40 nm	AN.CVT, S1.KLA, ALPHA1N.KLA, MUMINN.KLA	AN.CVT, DN.CVT, ALPHA1N.KLA, MUMINN.KLA
60 nm	AN.CVT, ALPHA1N.KLA, MUMINN.KLA, S1.KLA	AN.CVT, DN.CVT, ALPHA1N.KLA, EN.CVT
100 nm	AN.CVT, ALPHA1N.KLA, MUMINN.KLA, S1.KLA	AN.CVT, DN.CVT, EN.CVT, ALPHA1N.KLA
130 nm	AN.CVT, ALPHA1N.KLA, MUMINN.KLA, S1.KLA	AN.CVT, DN.CVT, EN.CVT, ALPHA1N.KLA

The purpose of the computer experiments is finding out parameters, which significantly affect to threshold voltage and drain current of the MOSFETs. Range of values from the nominal value is 20%. Studies on the significance carried out for MOSFETs with a channel length of 20 nm, 40 nm, 60 nm, 100 nm, 130 nm. I_D/V_G dependencies of this MOSFETs are shown in Fig. 1. The results of screening experiments are given in Table 1. Notations correspond to the factors used in the Silvaco.
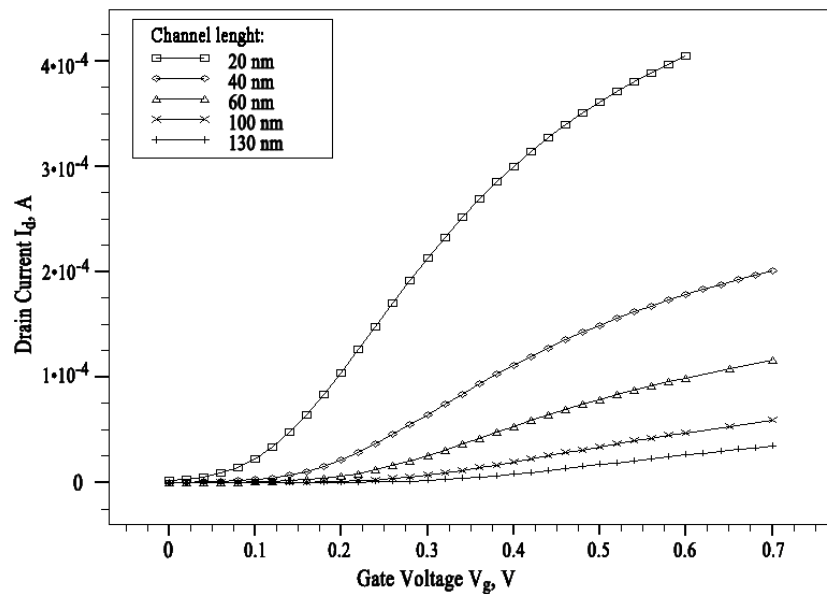

Figure 1 – I_D/V_G dependencies for MOSFETs with different channel length

Experiments show that AN.CVT, DN.CVT, S1.KLA, ALPHA1N.KLA, MUMINN.KLA, EN.CVT, especially AN.CVT, significantly affect on the transistor threshold voltage V_{TH} and drain current I_D. However, the extent of their influence depends on the size of devices. As an example, Fig. 2 shows the I_D/V_G dependencies that demonstrate differences in the degree of influence of the parameter EN.CVT when changing channel length.

III. CONCLUSION

The results of identification of the most significant Darwish model parameters for different channel length are presented. This problem was solved in the frame of the screening experiments methodology. The dependence of the degree of influence of parameters on the length of the channel is shown. These results will be used in the procedure of the parameters extraction of the deep submicron compact model of microelectronics devices.
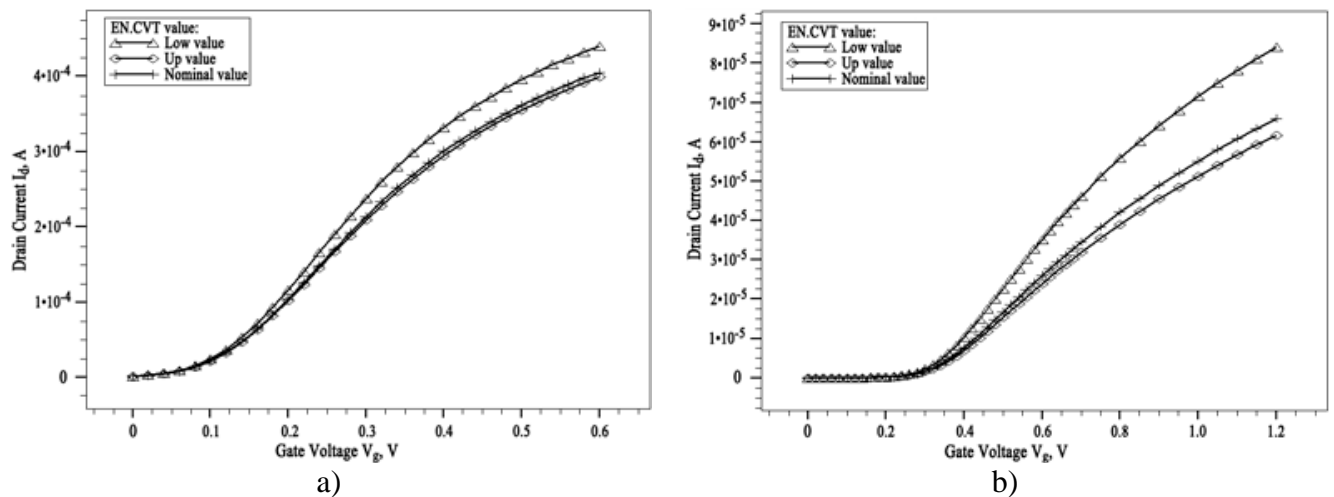
a)   b)

Figure 2 – I_D/V_G dependencies for MOSFETs with channel length
of 20 nm (a) and 130 nm (b) for different value of EN.CVT

REFERENCES

[1] ATLAS_user's_manual.pdf, 2012. http://silvaco.com/products/device_simulation/atlas.html.
[2] R. L. Plackett, and J. P. Burman, "The design of optimal multifactorial experiments," Biometrika, vol. 33, pp. 305-325, 1946.
[3] J. P. C. Kleijman, "Screening designs for polyfactor experimentation," Technometrics, vol. 17, No. 4, pp. 487-493, 1975.
[4] M. Darwish et al, " An improved electron and hole mobility model for general purpose device simulation," *IEEE Trans. Electron Devices*, 44(9), pp.1529-1538, Sep. 1997.

DEEP SUBMICRON RADIATION HARDENED STATIC RANDOM-ACCESS MEMORY IP

A. Kostrov

Belarusian State University of Informatics and Radioelectronics, *Minsk*, *Belarus*

I. INTRODUCTION

Modern System-on-a-Chip (SoC) is impossible to develop without built-in memory blocks. The availability of embedded memory enables SoC to perform fast, complex operations with large data arrays. Therefore the percentage of chip area occupied by various memories is constantly growing. Design of ICs which include large-scale memory blocks requires special software – IP Memory Block Compiler that would permit netlist and die topology to be created. Memory compilers allow quickly and automatically generate specifically sized memory blocks to be used in the design of ASICs.

Static Random-Access Memory (SRAM) is often embedded in microprocessor or microcontroller systems as their main memory component. SRAM permits quickly develop a highly reliable SoC required for spacecraft subsystems or instruments that are often used in extreme temperature and radiation environments, such as those in outer space, on the Moon and Mars. The reliability of electronics in the spacecraft becomes one of the most important concerns. Exposure to the high-energy subatomic particles and electromagnetic radiation may cause transient effects in memories such as glitches and soft errors, or permanent damage to the chip like lattice displacement, latch-up, or SEUs (single event upsets). Very-deep-submicron technologies with aggressive device and voltage supply downsizing have significantly reduced the critical charge required for bit storage in memory cells. This means low energy particles can flip the state in memory cells, therefore making memories sensitive to atmospheric neutrons as well as to alpha particles created from materials within the chip. In addition, the increased number and density of cells leads to increased probability of SEU occurrence.

To achieve acceptable SRAM memory radiation hardness, it may be necessary to employ one or more radiation impact mitigation techniques, such as radiation hardening by layout and circuit design, circuit/system redundancy, and/or data error correction codes. Under low radiation operating conditions or when the ASICs are shielded from radiation impact, radiation hardening means implemented into ASICs lead to sub-optimum performance. For example, radhard SRAM would be consuming much higher power – a precious resource in space missions. Therefore, space missions need a special memory compiler to be used. The compiler would permit designing ASICs targeted to tolerate required radiation levels and to be able to balance the radiation hardness, speed of operation and power consumption.

II. GENERAL INFORMATION

Pacific Microchip Corp. proposes to develop a novel configurable memory compiler for radiation hardened single port SRAM IP. The compiler will provide the choice between three types of memory cells that are based on 6-transistor (6T) improved architecture. The three memory cell designs will be aiming at different levels of immunity to radiation while consuming different levels of power. The novel compiler will implement such radiation hardening techniques and methods as:
– Radiation Hardening-By-Design (RHBD),
– Radiation Hardening-By-Layout (RHBL),
– Radiation Hardening-By-System (RHBS).
The radiation hardening means will include:
– N-channel Edge-Less Transistors (ELT) to mitigate Total Ionization Dose (TID) and Single Event Latchup (SEL);
– Miller capacitor connected between the two latches of the SRAM cell for mitigating Single Event Upset (SEU);

- PNPN parasitic thyristor triggering threshold increasing by adding guard rings for minimizing SEL;
- Bit interleaving for Multi-Bit Upset (MBU) mitigation;
- Single error correcting/double error detecting (SEC-DED) codes for SEU hardening;
- Triple-Modular Redundancy (TMR) with majority voters to reduce Single Event Transients (SET).

The proposed compiler features include:

1. The size of compiled memory SRAM: 8x2 bits (minimum), 32768x72 bits (2 Mb) (maximum)
2. Possible word width: from 4 to 72 bits with a step increment of 1 bit;
3. Word depth is from 8 to 32768 bits, depending on the width of the multiplexer.

Architectural flexibility of the compiled SRAMs will be achieved by using multiplexing to support a wide range of options in the aspect ratio of IP modules. Three levels of multiplexing will be supported: mux8, mux16, mux32. SRAM will have four control signals: 1) a user-defined non-inverting or inverting clock CE/CEB; 2) an output enabler (OEB); 3) a chip select (CSB); and 4) a read/write enable (WEB). Input and output data (I [n]) and (O [n]) will have separate ports. The output buffer circuit will be capable of operating in two user-defined modes: 1) a 3-states output and 2) a stable zero (hard "0") output. OEB control will be used to switch between output data enable mode and one of the user defined modes.

For successful using of memory modules as parts of SOC, designer needs to have behavioral description including timings and power models in Synopsys format for further timing and power analysis. For this reason compiler has to provide accurate and fast algorithm for calculation of these parameters. A mathematical model will be developed to describe the dependence of delay and power consumption on the combination of input factors (number of words, bits, output load and the input signal slope). The regression model will be used to determine the changes in the IP module parameters such as delay and power consumption and the aggregate change in the input factors (words, bits, load, input slope).

The Phase I effort will focus on cell, critical peripheral circuit and layout design as well as on the radiation hardened SRAM architecture. As a result of this Phase I effort we will provide the proof of the feasibility of implementing the proposed novel memory IP compiler. During Phase II, we will develop the flexible and configurable compiler, create layout and circuit databases for compiler, fabricate and test the proposed memories designed to meet the stringent radiation hardness and optimized power consumption requirements of space missions. We anticipate our proposed memory will be implemented based on the currently available IBM 45nm SOI CMOS or 65/90nm bulk CMOS technology. Phase II will result in the SRAM IP compiler, with memory prototypes ready for commercialization in Phase III.

Potential space applications for SRAM include microprocessor or microcontroller systems required in navigation, communication, command and control for launch vehicles, payloads, satellites, and any other space flight system requiring survivability in natural space radiation environments. Other systems used in space missions that require the storage of significant quantities of information include battery powered wearable electronics, portable monitors and devices. These systems would benefit from the proposed SRAM complied for minimum power consumption while trading the radiation hardness.

CONCLUSIONS

The proposed memory compiler will be used to design integrated memory arrays based on specifications defined through developed graphical user interface. The methodology for application of the memory compiler will also be prepared. As a result, we will provide a data file required for a specified type of the SRAM memory arrays.

The proposed novel memory compiler of radiation hardened SRAM IP offers a flexible solution for SoC and ASICs to meet the stringent radiation, performance, size and weight requirements of space applications.

SIMULATION OF CELLULAR PHONE RADIATION PROPAGATION IN BIOLOGICAL TISSUE AND MULTILAYER SHIELDING STRUCTURES

A. Prudnik, A. Kazeka, T. Borbotko
Belarusian State University of Informatics and Radioectronics, Minsk, Belarus

Summary: The process of cellular phone radiation propagation in biological tissue and multilayer shielding structures was simulated using mathematical modeling. Antenna patterns are calculated and their changes when applying protective shields are studied. The reflection and transmission coefficients of antenna were calculated.

I. INTRODUCTION

Rapid development and introduction into the daily life of new information technologies and means of information transmission and processing (computers, mobile communications, etc.) led to the emergence of new types of manmade factors — the emission of electromagnetic radiation in the range from subsonic to super-high frequencies. The mechanism of interaction between electromagnetic radiation (EMR) and biological tissues and human organism is not ascertained, but the common approaches are based on thermal effect or low-level radiation influence [1]. It was shown that this type of effects, especially after long term exposure and with inadequate protection from such effects, leads to increased fatigue and the development of various types of diseases of the human organism. In many cases the negative consequences of actions can only be detected through a decade or a few generations.

At the same time ensuring of the electromagnetic safety of the human operator from electromagnetic radiation of new types devices requires a lot of intellectual, material and time resources. According to the results of research in this area are developed state standards, sanitary rules and norms, which include regulations that limit the levels of electric and magnetic fields of different frequency bands, as well as regulations that establish the maximum permissible exposure levels for specific exposure conditions and groups of people.

The first aim of this work is to establish the quantitative characteristics of the influence of electromagnetic radiation on the human body, depending on the quality indicators of the technical protection tools, using mathematical modeling. The second one was to develop hardware and software for evaluation the effectiveness of protective devices of the human body from the EMR of personal computer or cell phone.

II. EXPERIMENT

Modeling of electromagnetic waves propagation in a system source of radiation – biological object – protection tool was performed using the finite difference method, with assistance of the software package XFdtd (version Bio-Pro). To study the interaction of the EMR with a biological object the model of the human head was used.

To investigate the dependence of the distance between the source of and the biological object on the EMR propagation characteristics receiving antenna was placed in the center of the human head model and transmitting antenna was placed at distances 10, 20 and 50 mm from it.

Electromagnetic shielding effectiveness was measured out by measuring equipment SNA 0.01–18, which allows measuring the reflection and transmission coefficients in the frequency range 0.7–2.14 GHz.

III. RESULTS AND DISCUSSION

It was shown that the electrical component of the EMR penetrates into the human head less than magnetic one, thus electrical component is characterized by greater absorption in biological tissues. This is due to the fact that the magnetic component force (Lorentz force) acts on electrically charged particles less than the force of the electric component [2]. An increase of distance between the transmitting antenna and the biological object from 10 mm to 20 mm leads to a decrease of the

transmission coefficient of 1 dB to –53 dB, which is caused by increase of losses during the propagation of electromagnetic wave in air space. In addition the reflection coefficient is reduced from –22 dB to –35 dB, which is caused by the multiplicity of the distance to the wavelength of EMR frequency range, while leading to greater absorption in the biological tissue. Increasing the distance up to 50 mm allowed reducing the transmission coefficient up to –58 dB, while the reflection coefficient increased to –13 dB.

The impact of EMR on biological tissues leads to a change of the water structure involved in biochemical processes [3]. The antenna pattern of EMR source (cell phone antenna) is determined by such impact. Therefore, to create a tool to protect the biological objects from intentional radiation with a view to minimize impact on the source parameters it is reasonable to use water-containing shields [4]. Moreover, it is possible to create a material with electromagnetic characteristics similar to biological tissues. To calculate influence of water-containing shield on the electromagnetic characteristics the shield model was placed between the models of the biological object and the EMR source. The dimensions of the shield varied in length 80 mm, 120 mm and in width of 10, 20, 40 and 60 mm, similar to a metal shield. The thickness of the shield (3.2 mm) was not changed, which is two cells of a countable space. It was shown on the basis of calculations that the use of water-containing shield reduced the transmission coefficient by 1–3 dB at its width 40, 60 mm, and at its length 120 mm. In addition the reflection coefficient remains within the –14÷16 dB, which is greater by 2–15 dB than without its use and fewer 2–6 dB than with the use of metal shield. This change is due to partial absorption of EMR by shielding material [5].

It was shown that the antenna pattern at the shield width of 40, 60 mm, and the length of 120 mm became greater at the angle of 90° by 1 dB, at the angle of 165° up to 17 dB and at the angles of 185° and 270° by 3 dB in comparison with its absence. The highest value of the antenna pattern observed at a distance 20 mm and 50 mm.

Placement of 120×60 mm water-containing shield between the biological object and the EMR source does not affect the antenna pattern in comparison with its absence. The metal shield is more effective water-containing one, but its application is characterized by greater reflection coefficient, which can increase the number of radiation effects in biological objects.

To increase the efficiency of water-containing shield, you can use a multilayer structure. Enhancing of its effectiveness could be ensured by placing a metal foil between the two layers of shielding material. The first layer will reduce the electromagnetic wave reflected from the second layer in air space. The second layer is necessary to provide the effectiveness of the whole of shield. The third layer is necessary for the absorption of electromagnetic wave that is reflected from the human head. The dimensions of protection tool was determined in accordance with the results of previous experiments (120×60 mm). The thickness of a water-containing layer was 3.2 mm, corresponding to two cells of a countable space. The thickness of the metal layer corresponds to one edge of the cell counting space. The model of the three-layer structure was placed close to the model of a biological object at a distance of 20 mm from the EMR source. The dependence of the reflection and transmission coefficients on the frequency in the presence and in the absence of the multilayer shield was calculated. On the basis of the calculations it was shown that the use of the multilayer shield the reflection coefficient decreased by 4.3 dB and the transmission coefficient decreased by 2.3 dB compared to the metal shield. In comparison with water-containing shield the reflection coefficient increased by 4.1 dB and the transmission coefficient decreased by 25.1 dB.

From simulation results revealed that the 120×60 mm multilayer shield is most effective (transmission coefficient –79.1 dB), but the antenna pattern of EMR source has no significant changes compared with the antenna pattern in its absence. Reducing the reflection coefficient of this shield will reduce re-reflection of the electromagnetic wave from various surrounding objects to the cell phone user. In this regard, the use of a multilayer shield will not only reduce the impact of radiation on biological objects, but also reduce the impact on the EMR source.

The experimental frequency dependencies of the transmission and reflection coefficients were obtained. It was shown that the single-layer shield reduces radiation from –12 to –18 dB. Its reflection

coefficient varies from –3 to –8 dB. The use of multilayer shielding structures provides an increment of the transmission coefficient to –35 dB, but the reflection coefficient decreased from –2 to –6 dB.

Full-scale testing of cellular phone radiation propagation with different shielding structures was performed using a cellular phone Nokia N78. The dependencies of the signal power level on the type of shield at the measurement point were obtained.

The power level of the cellular phone was decreased to 10.9 dB in the measuring point by a metal screen/ It was caused by electromagnetic wave being reflected by the high conductivity material.

Use of the single-layer shield led to a reduction of the electromagnetic radiation to 3.9 dB. The use of multilayer shielding structures provided a reduction of the electromagnetic radiation to 17.8 dB.

CONCLUSIONS

The model of the interaction of electromagnetic radiation with a biological object (human head) and the protection tool was proposed. It allows assessing the impact of electromagnetic radiation on a biological object in a system source of radiation – biological object – protection tool using calculated reflection and transmission coefficients. The calculation of these coefficients is performed with assistance of finite-difference method which allows taking into account the features of the electromagnetic wave propagation in the interfaces of air, protection tool as well as a biological object, which allows to characterize the influence of protection tool and biological objects on the antenna pattern of the EMR source.

The peculiarities of the interaction of radio waves (frequency 1800 MHz) with a biological object (ε=43.2; σ=1.29 S/m) are established. The increase of the distance from the radiation source to the biological object from 10 to 50 mm leads to an increase in the transmission coefficient from –53 to –60 dB with simultaneous increase of the reflection coefficient from –35 to –12 dB, which allows reduce the impact of EMR on a biological object.

REFERENCES

[1] Borbotko T.V., Kolbun N.V. Anthropogenic Sources of Electromagnetic Radiation. Principles of Personal and Social Safety (in Russian). Editor L.M. Lynkou, Minsk, BSUIR, 2008. ISBN 978-985-6767-85-5.

[2] V. Bogush, T. Borbot'ko, N. Kolbun, L. Lynkov, Novel composite shielding materials for suppression of microwave radiation, in Proc. of the 16th International conference on microwaves, radar and wireless communications (MICON 2006), Krakow, Poland, 2006. Vol. 2, P. 345–348.

[3] BioInitiative Report: A Rationale for a Biologically-based Public Exposure Standard for Electromagnetic Fields (ELF and RF). August, 2007.

[4] Lynkov L., Proudnik A., Borbotko T., Kolbun N. Wideband electromagnetic shields and absorbers. Korean-Belarusian joint workshop on nanocomposite technology. Daejeon, Korea, 2009. The Korea Atomic Energy Research Institute (KAERI). P. 52–86.

[5] Kolbun N.V., Borbotko T.V., Kazeka A.A., Proudnik A.M., Lynkou L.M., Simulation of electromagnetic radiation passing through liquid-containing nanostructured materials. Proc. of the SPIE. 2008. Vol. 7377. P. 7377–09.

PHOTO- AND UNDER X-RAY LUMINESCENCE FROM XEROGELS EMBEDDED IN MESOPOROUS ANODIC ALUMINA

N. Gaponenko[1], V. Kortov[2], V. Pustovarov[2], S. Zvonarev[2],
A. Slesarev[2], M. Rudenko[1], L. Khoroshko[1], A. Asharif[4],
H. Sohrabi Anaraki[1], A. Podhorodecki[3], G. Zatrub[3],
J. Misiewicz[3], and S. Prislopskii[4]

[1]*Belarusian State University of Informatics and Radioelectronics*, 220013 *Minsk, Belarus*
[2]*Ural Federal University named after the first President of Russia B. N. Yeltsin, Yekaterinburg, Russia*
[3]*Institute of Physics, Wroclaw University of Technology*, 50-370 *Wroclaw, Poland*
[4]*Stepanov Institute of Physics, National Academy of Sciences of Belarus, Minsk, Belarus*

Porous anodic alumina (PAA) films with pore and cell sizes ranging from 170 to 190 and 240 to 270 nm, respectively, have been generated on aluminum and monocrystalline silicon substrates followed by spin-on sol-gel derived coating with the subsequent thermal treatment producing microporous xerogel. The distribution of the xerogels corresponding to the chemical contents of willemite, garnet, titania, alumina, doped with terbium and strontium in PAA was investigated. Most xerogels, after annealing at 1000 °C, are mainly distributed near the pore bases, leaving much of the pore volume unfilled.

The distribution of yttrium aluminum composite in PAA is compared for sol-gel and co-precipitation methods. The xerogel/PAA structures reveal terbium-related luminescence under ultraviolet and X-ray excitation, with the strongest luminescence in the direction along the channels of the pores. The same xerogels generated on monocrystalline silicon reveal no luminescence under X-ray and weaker photoluminescence.

Thus, PAA enhances photo- and under X-ray luminescence from terbium doped xerogels. The fabricated structures are considered as a type of low-cost, thin-film convertor of X-ray irradiation into visible light, with an average cell size of the convertor of about 250 nm. Examples of polychromatic luminescent images on the basis of porous anodic alumina are also presented.

SECTION 3 – MOLECULAR DYNAMICS AND DFT SIMULATION

STRUCTURE OF SHOCK WAVES IN UNDERWATER EXPLOSION

S. Igolkin, A. Melker
Department of Mechanics and Control Processes
St. Petersburg State Polytechnic University, Russia

I. INTRODUCTION. HYDRODYNAMICS, MOLECULAR DYNAMICS, AND UNDERWATER EXPLOSIONS

Until the present time the study of underwater explosions was a privilege of hydrodynamics, which studies the motion of liquids and their interaction with solids. In theoretical hydrodynamics, for description of the movement of an incompressible liquid, having continuity and fluidity, as well as viscosity, one uses the continuity equation and Navier-Stokes' equations. It is difficult to solve this problem by simply writing a complete system of conservation laws in the form of differential equations and closing defining relations, or by developing unique computer programs and codes [1].

Contrary to the customary approach, we have used molecular dynamics [2] for studying underwater explosions. The main motive is such: since the accepted methods of studying "a wealth of phenomena which nature is not well understood" seem to be ineffective, it is reasonable to try other methods. It should be noted that molecular dynamics has shown its effectiveness in studies of a great variety of phenomena, e.g. radiation damage of solids, deformation and fracture of materials, nucleation, evolution and self-organization of biological structures and so on [2]. The problem of modeling underwater explosion, formation and propagation of explosion-generated water waves using molecular dynamics was carefully argued in [3]. In this contribution we used the approach described in that article.

II. COMPUTATIONAL PROCEDURE

We restricted ourselves to 2D computer simulations. To gain a more penetrating insight into the explosion phenomenon, we excluded explosive debris from further research. For this purpose, we developed a simpler explosive model [3]. A certain number of water particles were placed in a circular area of a given size at a predetermined distance. Thereafter the particles were subjected to radial compression. As a result of changing the distance between particles, the compressed structure accumulates a large amount of elastic energy. During decompression these particles acquire enormous velocities, producing an explosion.

In classical molecular dynamics [2], the motion of a system of N particles is described with the help of Newton equations. There are various numerical schemes for solving the classical equations of motion, from the simplest first order Euler's methods to the predictor – corrector scheme of high order accuracy. One of the most common and, at the same time, stable and efficient approach to the time discretization of Newton's equations is the Velocity–Verlet algorithm [4] which was used in the present study as a compromise between speed and accuracy. Integration of the motion equations allows us to find the trajectories of particles. If the initial positions and velocities of the particles are given, the evolution of the system in time depends only on the potential, which determines the interaction between the particles. There are a lot of potentials which are used in molecular dynamics calculations [5]. We have chosen the Lennard–Jones potential. The reasons are given in [3].

III. RESULTS AND DISCUSSION

Movie. The calculations were done with a system consisting of 27,500 particles. An explosive was inserted into the water after reaching the equilibrium. The temporal evolution of underwater

explosion is demonstrated in Fig. 1. Fig. 1a (left) shows the system before explosion; the zoom area specifies the location and structure of explosive. Decompression of the explosive creates a shock wave and a cavity (Fig. 1b, left). It should be emphasized that the cavity is not empty and resembles fog (rarefied water). The expanding shock wave produces a dense compression shock in a narrow region (Fig. 1c, left). Simultaneously, at this moment the shock-wave front reaches the free surface. Thereafter the cavity reaches the surface transforming into a water crater (Fig. 1a, right). The following picture resembles a volcanic eruption (Figs. 1b, 1c, right). At first the volcano is very active and then becomes extinct.

  Structure of a shock wave. Up to now there is no complete physical theory describing quantitatively nucleation, development and damping of shock waves. The existing theories, as was mentioned above, have a formal thermodynamical character. The only exception is the book [6] but it contains too many assumptions and became out of date. However, if one wants not only to describe the properties, but understand their nature, one should establish their origin turning to the particles which constituent the system [7]. Unfortunately there is no experimental methods which are able to give such information.
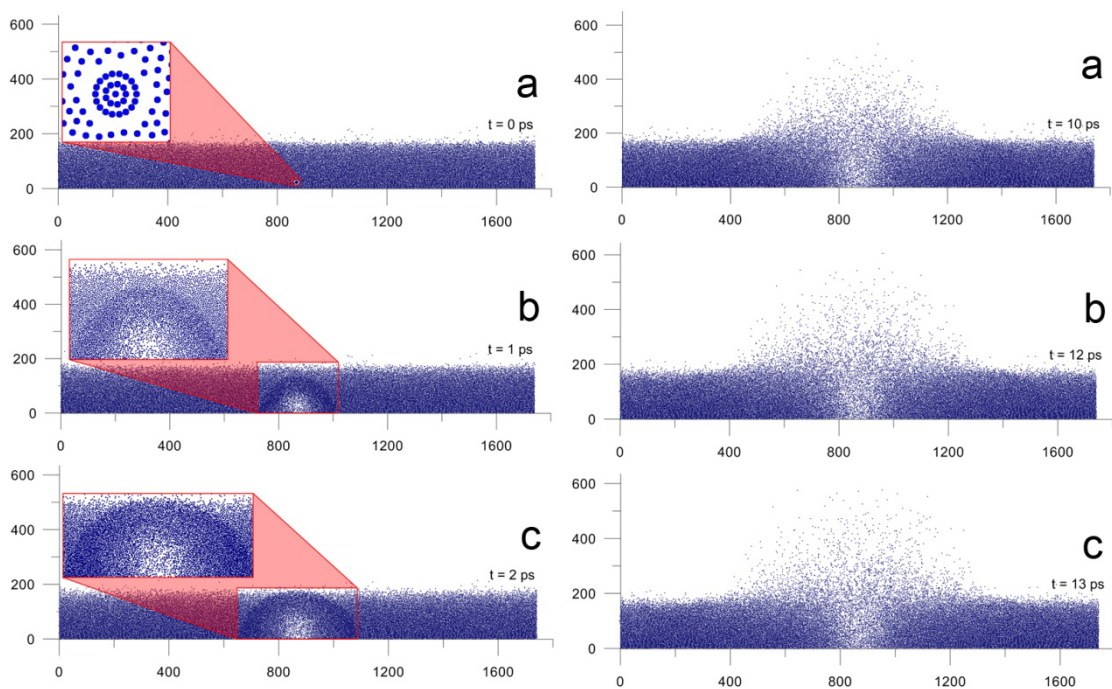
Figure 1 – Time evolution of underwater explosion, t = 0 – 13 ps. Units are in nm-1.
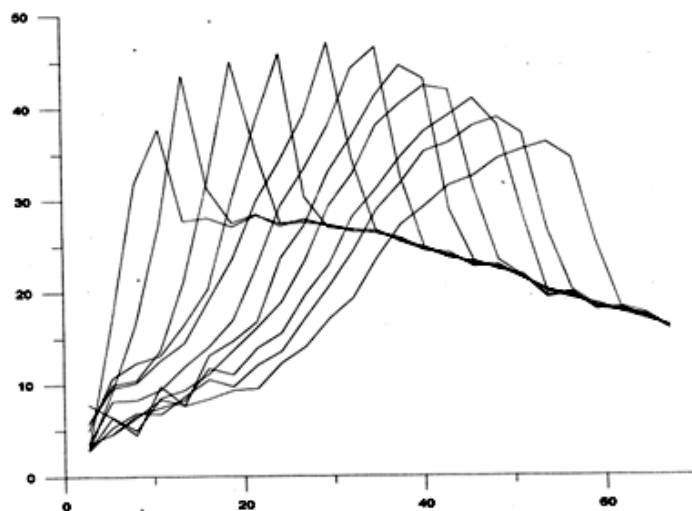
Figure 2 – Time evolution of shock-wave shape, $t = 0$–5 ps. Units are in nm^{-1}.

In the previous paper [3], we have promised to do the next step, namely, to use one more advantage of molecular dynamics, i.e. to study simultaneously both dynamical structure of a system, observing the motion of separated particle, and to calculate averaged characteristics of the system, e.g. energy, pressure, temperature, etc., especially their distribution in the system and their changing in time. For this purpose we have developed a special technique. The example of such calculation is represented in Fig. 2 which shows the evolution of shock-wave shape in the thirty degree sector (counter-clockwise from x-axis) in an orderly sequence. The wave is moving from left to right.

REFERENCES

[1] V. K. Kedrinskii, *Hydrodynamics of Explosion*: *Experiments and Models* (Springer, 2005).
[2] A. I. Melker. // *Proceedings of SPIE* **6597** (2007) 659702.
[3] S. Igolkin, A.I. Melker // *Materials Physics and Mechanics* **23** (2012) 147.
[4] M. P. Allen, D.J. Tildesley, *Computer Simulation of Liquids* (Clarendon Press, 1989)
[5] A. I. Melker // *Reviews on Advanced Materials Science* **20** (2009) 1.
[6] Ya. B. Zeldovich, Yu.P. Raizer, // *Physics of Shock Waves and High-temperature Hydrodynamic Phenomena* (Fizmatgiz, Moscow, 1966), in Russian.
[7] A. I. Melker // *Dynamics of Condensed Matter*, *vol*. 1, *Vibrations and Waves*; *second edition* (St. Petersburg Academy of Sciences on Strength Problems, 2013), in Russian.

COMPUTER SIMULATION OF BRITTLE BEHAVIOR IN Ti_3Al

L. Yakovenkova

Institute of Metal Physics of RAS, *Ekaterinburg*, *Russia*

Abstract – Orientation dependence of fracture behavior in Ti_3Al is investigated. The model of shear microcracks nucleation in basal, with screw ***a*** superdislocations coalescence, is introduced. It is demonstrated, that long-range stress of dislocations in a slip band plays an important part in the process of microcrack nucleation.

Ti_3Al (ordered hexagonal superstructure $D0_{19}$) is the main component of the number alloys, which are known as promising materials for heat-resisting and heatproof applications. Brittleness of the intermetallic compound hinders its practical applications. The orientation dependence of the fracture behaviour of a Ti_3Al single crystal was discovered as well: the deformation before fracture reaches the value of ~250% for prism slip, while for basal slip brittle fracture observes immediately after loading even with compression. The relationship between the susceptibility of a metal to cleavage and plastic relaxation of stresses near the crack tip by emitting dislocations for Ti_3Al single crystals has been studied using the Rice-Thompson model. Using the method of computer simulation the surface energy which determines the ability of a crack to opening and the energies of unstable stacking faults which determine the energies barriers that should be overcome in the processes of dislocation slip have been obtain. Criteria of brittle fracture of Ti_3Al with allowance for experimentally observed types of cleavage planes and dislocation slip systems have been estimated. Decohesion energy and the energy of unstable stacking faults for the basal plane, prismatic and pyramid planes was studied using molecular dynamic method with EAM interatomic potentials [1]. It was shown that cleavage in Ti_3Al is due to low decohesion energy values, which facilitates cracking, and high energies of unstable stacking faults, which prevents the formation of a plastic zone and stress relaxation at crack tip. An analysis of the relationship between the decohesion energy and the energy of unstable stacking faults indicates the intrinsic nature of brittleness of Ti_3Al caused by specific features of interatomic interactions in these intermetallic compounds.

The dislocation model of the formation of shear type microcracks in basal plane slip band, based at the analysis of the core structure of ***a***-superdislocations in the basal and prism planes [2,3], is discussed. It was established that and the core of the dislocations of edge as well as screw orientation in the plane of the prism is planar [4]. Nonplanar core structure of the screw dislocations in the basal plane was detected. Model for shear microcracks nucleation in basal slip band take into account the processes of coalescence of screw ***a***- superdislocations in basal plane and cross-slip into prism plane. As a result of consecutive stages of internal dislocations rearrangements the total configuration energy lowers, because the reactions occur between attracting partials. The final configuration is stable. It consists of the bands of anti-phase boundaries in the initial basal plane and in the planes of cross slip – the prism planes. The model of shear microcracks nucleation in basal planes, with screw ***a***-superdislocations coalescence, takes into account the long-distance elastic interaction of ***a***-superdislocations. The molecular dynamic method was used to study the processes of coalescence of screw ***a***- superdislocations in basal slip band. It is demonstrated, that long-range stress of dislocations in a slip band plays an important part in the process of microcrack nucleation. The formation of short bands of prism slip accompanying the (0001) basal slip was explained. Consecutive coalesce of microcracks in the basal plane results in macrocrack nucleation. Based on the suggested model, the mechanisms of macrocracks formation are discussed.

REFERENCES

[1] Yakovenkova L.I., Kirsanov V.V., Karkina L.E., Balashov A.N. Rabovskaya M.Ya.N-particle potentials of interatomic interaction in Ti_3Al and simulation of planar defects in(0001), {1100}, {2021} and {1121} planes. // Phys. Met. Metallogr. 2000. Vol.89. P.31-38.

[2] Yakovenkova L., Malinov S., Novoselova T., Karkina L. Fracture behaviour of Ti_3Al single crystals for the basal slip orientation. // Intermetallics. 2004. V.12. P.599-605.

[3] Yakovenkova L., Malinov S., Karkina L., Novoselova T. Crack geometry for basal slip of Ti_3Al. // Scripta Materialia. 2005. V.52. P.1033-1038.

[4] Yakovenkova L.I., Karkina L.E., Rabovskaya M.Y. The atomic structure of the 1/3<2110> superdislocation core and prismatic slip in Ti3Al. // Technical Physics. 2003. Vol.73. No.1. P. 60-66.

COLLISIONS AND STABILITY OF QUANTUM WAVE PACKETS

A. Bagmanov[1], *A. Sanin*[2]

[1]*Independent Researcher*

[2]*Saint-Petersburg State Polytechnical University, Department of Theoretical Physics, Russia*

Abstract *– Time evolution of the quantum wave packets is discussed in context of the non-linear cubic Shrödinger equation and equivalent hydrodynamical description. In hydrodynamical description, the quantum Hamilton-Jacobi equation for action is rewritten in variables: probability density and probability flow density. These variables are smooth at the node points. The studied dynamical systems have finite dimensions and impenetrable walls, they have been analyzed at the different initial conditions including the Gaussian-like form. Our interest in investigation of the properties of dynamical non-linear equations is caused by existence of stable solutions which correspond to the quantum non-spreading wave packets. Behavior of the localized wave packet in one-dimensional system is characterized by classic-like trajectory and collisions against walls. The packet keeps localized form during some time interval and can oscillate around some "stable" profile. To describe the time evolution of two wave packets on plane we have to integrate the non-stationary two dimensional Shrödinger equation for the two-particle wave function taking into account the symmetry properties. But, as first step, in present investigation the problem was essentially simplified. The particles were considered as spinless, and wave function was presented in the product form of two functions. Now, the collisions between quantum wave packets of two particles will also occur. During some time interval, fragmentations of packets are generated. Then they return to its original shape and move as classical particles. In both cases, non-linearity plays self-organizing role in comparison to the regimes when non-linear cubic term is absent.*

I. SINGLE WAVE PACKET DYNAMICS

In simple case, we investigated solutions to the one-dimensional Shrödinger equation

$$i\frac{\partial \Psi}{\partial t} = -\frac{1}{2}\frac{\partial^2}{\partial x^2}\Psi + k|\Psi|^2\Psi + U\Psi \tag{1}$$

for wave function $\Psi(x,t)$ with different initial conditions in the form $\Psi_0 = C\cdot sch(x)\cdot \exp(iV_0 x)$ and $\Psi_0 = 1/\sqrt[4]{2\pi\sigma^2}\cdot \exp\{-(x-x_0)^2/4\sigma^2\}$. The equivalent description is given by hydrodynamical equations

$$\frac{\partial N}{\partial t} = -\frac{\partial J}{\partial x}\,,$$

$$\frac{\partial J}{\partial t} = \frac{\partial}{\partial x}\left(-\frac{J^2}{N} + \frac{1}{4}\left(\frac{\partial^2 N}{\partial x^2} - \frac{1}{N}\left(\frac{\partial N}{\partial x}\right)^2\right) + \kappa N^2\right) - \frac{\partial U}{\partial x}N,\ \kappa = -k. \tag{2}$$

Here, *N*, *J* are probability density and probability flow density, respectively. The variables (*N*, *J*) are smooth at the node points. Stationary solutions (1) and (2) were also studied. Our interest to the properties Eq. 1 is caused by stable solutions which correspond to the quantum non-spreading wave packets [1]. In context of listed equations, we investigated soliton-like wave packets, fragmentations under collisions against the walls of potential well and self-reconstruction to its original form caused by nonlinearity. The comparison with solutions at $\kappa = 0$ is carried out.

II. INTERPACKET COLLISIONS (COLLISIONS BETWEEN PARTICLES)

To describe two wave packets at the same time we offer the simplified dynamical model where collisions between packets can be described with potential terms as follows

$$i\frac{\partial \Psi_1}{\partial t} = -\frac{1}{2}\Delta\Psi_1 - \kappa|\Psi_1|^2\Psi_1 + U_{1\leftarrow 2}(\Psi_2),$$

$$i\frac{\partial \Psi_2}{\partial t} = -\frac{1}{2}\Delta\Psi_2 - \kappa|\Psi_2|^2\Psi_2 + U_{2\leftarrow 1}(\Psi_1). \tag{3}$$

Here, $\Delta = \dfrac{\partial^2}{\partial x^2} + \dfrac{\partial^2}{\partial y^2}$; $U_{1 \leftarrow 2}(\Psi_2)$, $U_{2 \leftarrow 1}(\Psi_1)$ are modeled terms describing collisions. It is essentially to propose that mean coordinates of two colliding particles behave by nearly classical way. Our calculations confirm this statement. It is important to note both packets show light fragmentation w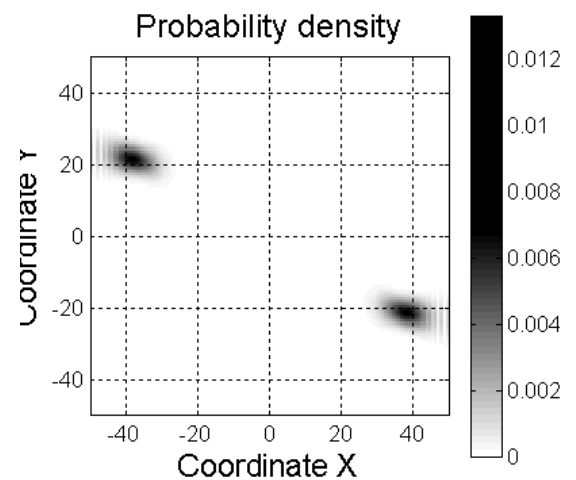hen they are placed nearby. For initial specified packets and $\kappa = 5$, the time evolution is presented in Figs. 1-4.
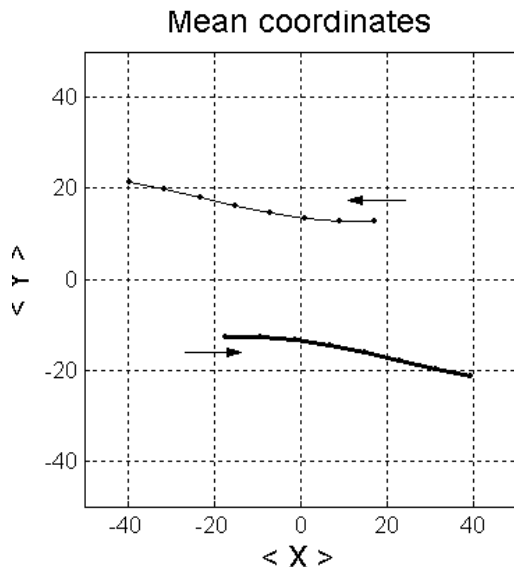
Figure 1 – Mean coordinates of particles
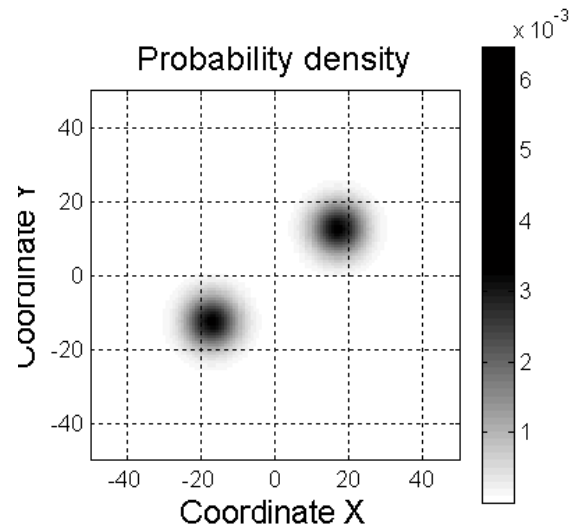
Figure 2 – Wave packets at t = 6.28
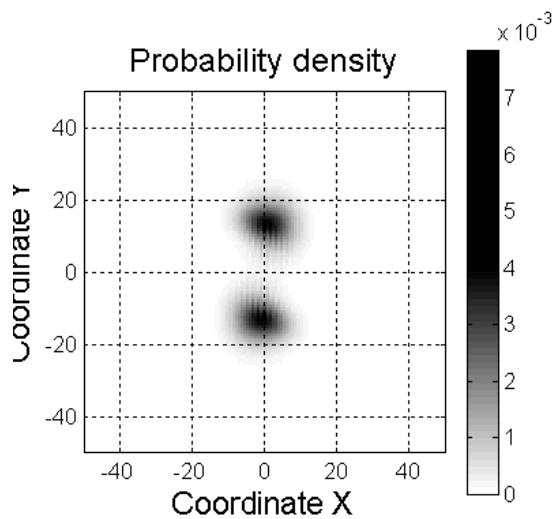
Figure 3 – Wave packets at t = 18.85

Figure 4 – Wave packets at t = 50.27

In both cases, non-linearity plays self-organizing role in comparison with regimes when non-linear cubic term is absent.

REFERENCES

[1] A. L. Sanin. A. T. Bagmanov, Waves in quantum systems with nonlinearity and walls // Material Physics and Mechanics, V. 13, No. 2, 2012, P. 117-123.
[2] A. T. Bagmanov, A. L. Sanin, Smooth solutions of modified Madelung equations. Nonlinear phenomena in Complex Systems // An Interdisciplinary Journal, V. 12, No 3. Belarus, 2009 P. 289-294.

ATOMISTIC SIMULATION OF MARTENSITIC TRANSFORMATION IN Fe$_{80}$Ni$_{20}$ NANOPARTICLES INITIATED THEIR AGGLOMERATION

L. Karkina, I. Karkin

Institute of Metal Physics, RAS, Ekaterinburg, Russia

Abstract – The mechanisms governing the formation of structural state and kinetics of transformations in the metallic clusters Fe$_{80}$Ni$_{20}$ during martensitic transformation are investigated by molecular dynamics (MD) method.

I. Introduction

Martensitic $\gamma \rightarrow \alpha$ transformation in a defect-free crystal is not happening during MD study. Analysis of the free energy of the alloy Fe80Ni20 depending on the lattice along the path at Bain deformation at $\alpha \leftrightarrow \gamma$ transformation shows that there is a high energy barrier between the fcc and bcc states, so the transformation is not obtained in the MD simulations at cooling the fcc phase. By lattice defects, locally, the barrier is lowered, so there may be a nucleation of a new phase. For example, in the crystallites with periodic boundary conditions, simulating an infinite crystal, the martensitic transformation could be observed in the presence of ~ 2at% vacancies. Martensitic $\gamma \rightarrow \alpha$ transformation has been studied by the MD method in cubic nanocrystalline particle size of 24 nm with free surfaces [1]. The transformation started from the top of the cube, where the atomic coordination number is reduced and lowered the $\gamma \rightarrow \alpha$ transformation barrier. During the time interval t ~Δ 30 ps at T = 50K the transformation is completed, the typical twinned martensite crystals are emerging on the edges of the surface of the cube and are distributed inside the crystallite.

In [2] studied the martensitic transformation in polycrystalline alloy Fe80Ni20 fine-grained (~ 3 nm in diameter), which were obtained by compacting under pressure at a temperature T = 800K. Analysis of the radial distribution function showed that in the regions near the grain boundaries formed bcc - like structure. Upon cooling of the polycrystalline $\gamma \rightarrow \alpha$ transformation begins from the grain boundaries. Number bcc phase continuously increases and reaches at T = 25K of ~ 52%. Thus, martensitic transformation could be observed only in lattice with defects, where the barrier is lowered locally, for example nearby the grain boundaries.

In this work, the martensitic transformation was studied near the boundaries, formed by agglomeration of the two nanoparticles. It was studied the effect of particle disorientation on the coalescence processes and on disorientation of the particles after the martensitic transformation.

II. Results of MD simulation

The kinetics of structural transformations was performed by the molecular dynamic method using N-body Meyer-Entel [3, 4] potentials of interatomic interactions constructed by embedded-atom method. These potentials permit one to calculate the values of the lattice parameters, elastic modules, cohesive energy, and vacancy-formation energy for Fe and Ni. They also give the magnitudes of the energy differences between fcc and bcc phases for Fe-Ni alloys close to the experimental ones and correctly reproduce the concentration dependences of the temperatures of martensitic and austenitic transformations in bulk materials.

Two agglomerated particles with fcc lattice and with the atoms number N=10185 (diameter d~6 nm) cooled from the temperature T=1400K to T=0K. The cooling of clusters was carried out by a discrete change of temperature with a step of 20K. The cooling rate equals to ~4x10^{12} K/s. In the initial configuration the two particles were rotated relative to each other to obtain desired disorientation. The disorientation of particles corresponded to the special large-angle asymmetrical tilt grain boundaries Σ11, Σ3 and Σ9. Disorientation axis was <110>, the disorientation angles were 70.53 degrees for the boundary Σ3, 50.47 degrees for the boundary Σ11 and 38.94 degrees for the boundary Σ9. The plane of contact was selected (010).

After cooling to T ~ 200-300K each particle undergoes martensitic transformation (Fig.1). The shift in the transformation process starts from the boundary between two particles near the surface and

further extends through the entire particle. Depending on the initial disorientation of the particles we obtained either single-domain state (Fig1,c), or there is an agglomerate of two disoriented particles with a bcc lattice (Fig1a,b). Each particle consists of 1-2 domains (Fig.1a,b).

Sintering in the fcc phase leads only to insignificant change in the disorientation of one particle with respect to the other particles of a given size [5]. Figure 2 shows the orientation relationship between one of the particles after sintering in fcc phase and after martensitic transformation for $\Sigma 11$ boundary. The analysis shows that between fcc and bcc phases are realized Kurdjumov-Sachs orientation relations. The dotted line near the center of the pole figure marked parallel poles <110> fcc phase and <111> bcc phase. Center pole figure also coincides with the axis of disorientation FCC particles in the initial configuration. For the boundary Σ 11 disorientation angle between the particles in the initial configuration is 180-129.53 = 50.47 degrees. Axis of disorientation in the bcc phase is parallel to the <111> direction, so that the angle of disorientation is close to an element of the point group symmetry of the bcc phase (Fig.1c) after completion of the martensitic transformation.

a)   b)   c)
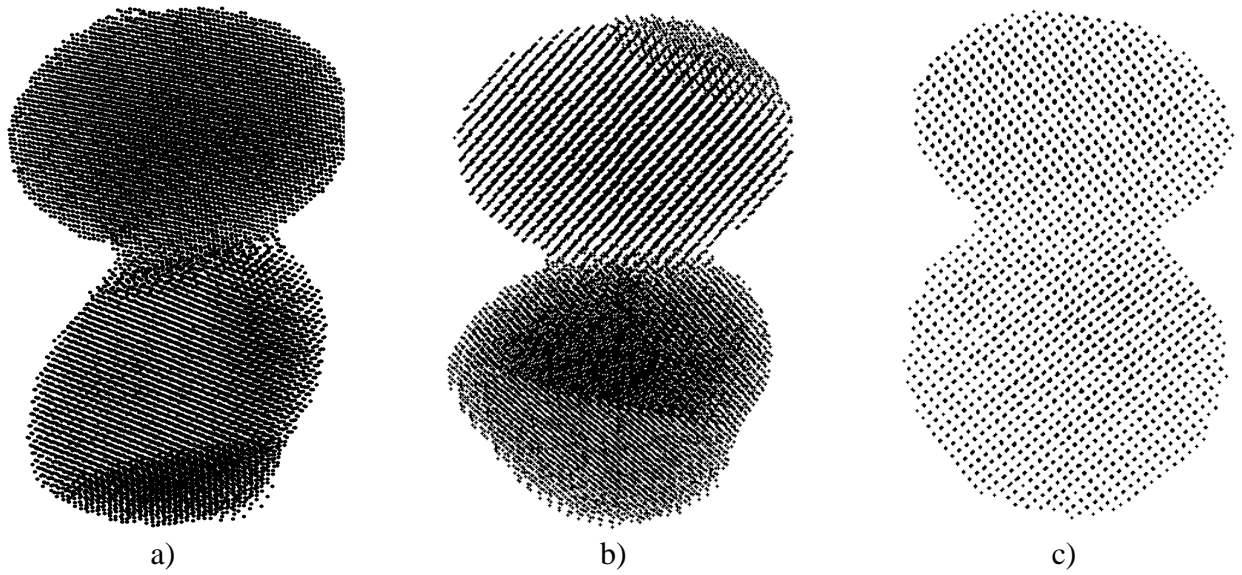
Figure 1 – $\gamma \rightarrow \alpha$ transformation of the two particles agglomerate
with the grain boundaries $\Sigma 3$ (a), $\Sigma 9$ (b) and $\Sigma 11$ (c), temperature T=0K.
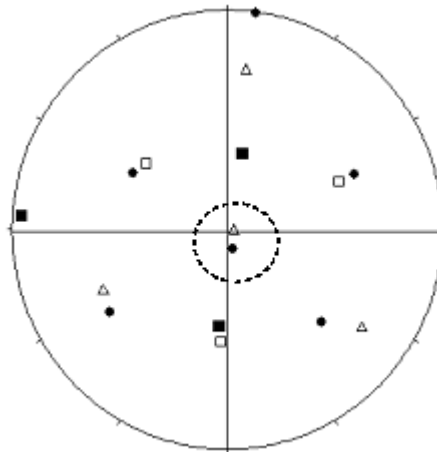
Figure 2 – Cooperative pole figure fcc and bcc phases. Shaded symbols refer to the fcc phase,
not hatched - to the bcc phase. Circles denote the poles of the <110> squares - <100>, triangles - <111>

III. CONCLUSIONS

We have studied $\gamma \rightarrow \alpha$ transformation during cooling in agglomerated disorientated two particle clusters of Fe80Ni20 alloy by the method of molecular dynamics. It has been found that the shift in the transformation process starts from the boundary between two particles near the surface and

further extends through the entire particle. It is demonstrated that depending on the initial disorientation of the particles it was obtained either single-domain state or there was an agglomerate of two disoriented particles with a bcc lattice.

REFERENCES

[1] P.Entel, R.Meyer, K.Kadau. "Molecular dynamics simulations of martensitic transitions", Phil. Mag. B, **80** (2), 183-194 (2000).

[2] K.Kadau, P.Entel, P.S. Lomdahl. "Molecular-dynamics study of martensitic transformations in sintered Fe-Ni nanoparticles", Computer Physics Communications, **147**, 126-129 (2002).

[3] K. Kadau, P. Entel, T.C. Germann, P.S. Lomdahl and B.L. Holian, "Large-scale molecular-dynamics study of the nucleation process of martensite in Fe-Ni alloys", Journal de Physique IV, **11**, 8-17 (2001).

[4] R.Meyer, P.Entel, "Martensite – austenite transition and phonon dispersion curves of Fe$_{100-x}$Ni$_x$ studied by molecular-dynamics simulations", Phys. Rev. B, **57** (9), 5140-5147 (1998).

[5] L. E. Kar'kina, I. N. Kar'kin, Yu. N. Gornostyrev, and L. I. Yakovenkova, "Size Effect during Two Particle Agglomeration: Results of Molecular Dynamics Simulation", Bulletin of the Russian Academy of Sciences: Physics, **73**(8), 1030–1033 (2009).

MODELING AND INVESTIGATION OF
THE HETEROFULLERENES $C_{59}X$ (X=Na, Li, Mg, Be)

O. Kozlova[1], *J. Tamuliene*[2]

[1]*Belarusian State University of Informatics and Radioelectronics*, *Minsk, Belarus*
[2]*Institute of Theoretical Physics and Astronomy*, *Vilnius University*, *Lithuania*

Abstract – Geometric and electronic structure of the heterofulerenes $C_{59}X$ (X=Na, Li, Mg, Be) has been studied theoretically. The main emphasis has been given to the stability of the heterefolerenes and their both HOMO and LUMO energies and ability to stabilize negative charge. Obtained results proves the application possibility of investigated heterofulerenes as components of solar cells.

In various fields of science and technology growing interest of researchers is dedicated to the variety of unusual physical and chemical properties of fullerenes and promising prospects of their possible applications.

Particularly, heterofullerenes (the type of fullerenes) attrack great attention because of their various interesting features associated with quasi-two-dimensional structure, high anisotropy and acceptor properties. So far successful heterofullerenes, containing the elements of B, N, Si, O, P, As and Ge etc., have been reported. Remarkable structural, electronic, optical, and magnetic properties were shown during the experimental and theoretical investigation of this material.

The objects of our study were structures based on C_{60} fullerene, so-called heterofullerene $C_{59}X$ (where X - the alkali metal Na, Li, Be and Mg). These system offers new possibilities for studying low-dimensional magnetic phenomena, particularly because the forces between carbon and metal elements (Na, Mg, Li, Be) appear to be very weak. In order to determine the most stable system with an implanted atom, the highest I_h and lowest C_1 symmetry of C_{60} fullerene were chosen. Heterofullerene structures of C_1 and I_h symmetries are shown on Figs. 1 and 2, respectively. The investigations were performed by B3LYP exchange – correlation hybrid functional [1] with 6-311G basis set implemented in Gausssian 03 programe package [2]. We have checked all possible different positions of implanted atoms.
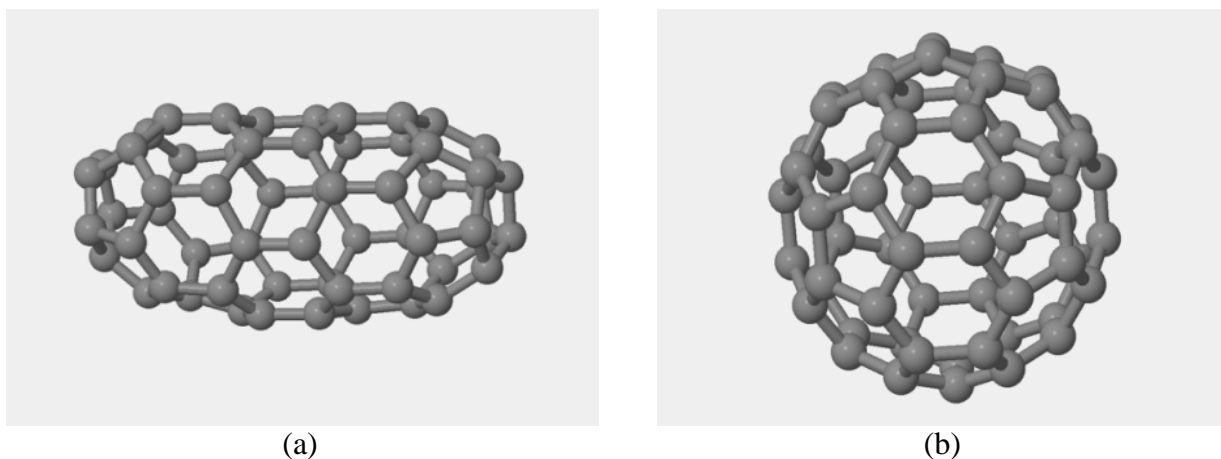

(a)   (b)

Figure 1 – 3D structure of C_{60} fullerene with C_1 (a) and I_h (b) symmetry

The most advantageous positions of Li, Be, Na, and Mg atoms in the system are determined, and their magnetic properties, such as the magnetizability, are investigated. By results of analysis we can say that there is a significant difference between the positions of the implanted atoms in heterofullerenes with symmetry C_1 in opposite heterofullerenes with symmetry I_h. At the same time the pure fullerenes are the most stable systems. However, results obtained indicate investigated fullerene as strong diamagnetic. On the other hand, the new modeled materials with a symmetry I_h exibited smaller HOMO-LUMO gap than that of the pure fullerenes. But this is not quite true in case of heterofullerene with symmetry C_1. Calculated values of HOMO-LUMO gap are shown in Table 1.

TABLE 1 – Values of HOMO-LUMO gap

Cage of fullerenes C_{60} with I_h symmetry		Cage of fullerenes C_{60} with C_1 symmetry	
Fullerene system $C_{59}X$	HOMO-LUMO gap, eV	Fullerene system $C_{59}X$	HOMO-LUMO gap, eV
where X= C (pure)	2.87	where X= C (pure)	1.31
where X= Na	1.39	where X= Na	1.33
where X= Li	1.96	where X= Li	1.28
where X= Mg	1.55	where X= Mg	1.19
where X= Be	1.63	where X= Be	1.25

It is known that HOMO-LUMO gap may be related to ability of the hetrofullerenes to generate photocurrent. Thus, smaller band gap indicate that low-energy light could be used when the above described heterofullerenes would be used to generate photocurrent.

REFERENCES

[1] B. Miehlich, A. Savin, H. Stoll, and H. Preuss, *Chem. Phys. Lett.*, Vol.157, pp. 200-06,1989.
[2] J. Frisch Gaussian 09, Revision A.1, *Gaussian*, *Inc.*, *Wallingford CT*, 2009.

RHEOLOGICAL PROPERTIES OF AMORPHOUS AND NANOCRYSTALLINE METALLICALLOYS UNDER TRANSIENT CREEP

D. Fedotov, T. Pluzhnikova, L. Novgorodov, A. Yakovlev, V. Feodorov
Tambov State University, Russia

Abstract – The laws of the various strains of amorphous and nanocrystalline metallic alloys under transient creep. Found that the deformation of amorphous alloys and nanokristallichevkih in transient creep stepwise. It is noted that below the crystallization temperature deformation proceeds heterogeneously above homogeneously. Morphological features of the condition of surfaces and fracture surfaces of samples at various stages of creep.

I. INTRODUCTION

Metallic glasses (MG) in many references are similar to ordinary glasses and liquid metals [1]. One of the amazing properties of amorphous alloys is their ability to plastic flow. In an amorphous solid there isn't translational symmetry, and, consequently, the dislocation in the classical understanding of the nature of the defect. [2] Thus the amorphous solid must be completely brittle. But in MG plastic, deformation occurs yet. Plastic deformation in the amorphous alloys can occur homogeneously or non-homogeneous. The evolution of the structure of metallic glasses is the most important problem of the physics of strongly disordered systems. The actual problem of physics of disordered media is the study of plastic flow of MG as well as increasing the number of research methods of their mechanical properties.

In this regard, the goal of this paper is to study of deformation and fracture of various amorphous and nanocrystalline metallic alloys under transient creep.

II. INSTRUCTION FOR AUTHORS

Studies had been using tapes of amorphous Co-based systems: Co-Fe-Mn-Si-Cr-B-Ni (AMAG-170-179 AMAG, AMAG-180), Co-Fe-Mn-Si-B-Cr (AMAG-183 AMAG-186) and ribbon of the nanocrystalline iron-based alloy Fe-Cu-Nb-Si-B (AMAG-200) obtained by spin-ningovaniya. The objects of study were the samples measuring $55 \times 3,5 \times 0,02$ mm.There was created and developed a method of installation of the experiment to test for creep. A sample was helded between two jaws, one of which is fixedly connected to the upper part of the installation, the lower jig in turn was attached to the sample and remained in a free state in the specimen by creating initial mechanical stress-tions ~13,5 MPa. Then the sample was placed in an oven. During the experiments, the heating of the samples was determined pyrometer Testo 845. The heating rate was 0,65 °C/s. Elongation of the specimens were fixed on a digital video camera. Then the pro-plagued scan video frame by frame, which is determined on the basis of the change in length of the sample during the experiment.

There were built dependences of relative samples' deformation from time.

Prior to the crystallization temperature according to the observed long stops corresponding to a certain amount of deformation. After the temperature of crystallization of the dependence varies. Stops of deformation become less long-inflammatory, and the number of deformation jumps at a fast rate increases.

It is established that the destruction of the samples Co-based alloys occurs when the strain reaches 25% and a temperature ~600-700 °C. It is noted that in the Co-based alloys below the crystallization temperature deformation occurs hetero-genetic above homogeneously.

Studies of amorphous structural state at different stages of the heating carried out on the fracture surfaces of the samples. For this purpose, samples after heating to a temperature of Position recovered and destroyed by bending. Fig. 2 shows the morphology of the fracture surface of the alloy samples AMAG-186. It was established that the samples at a heating temperature of more than 400 °C, there is a pronounced grain structure. With increasing temperature, the heating of the sample size increases crystals. When heated to 400 °C is about the size of 100 nm while heating to 500 °C and 600 °C ~ 250 nm and ~500 nm, respectively. Similar changes are confirmed by X-ray structure analysis.

106

The diffraction patterns instead of "halo", typical for amorphous structures there is a series of diffraction peaks.
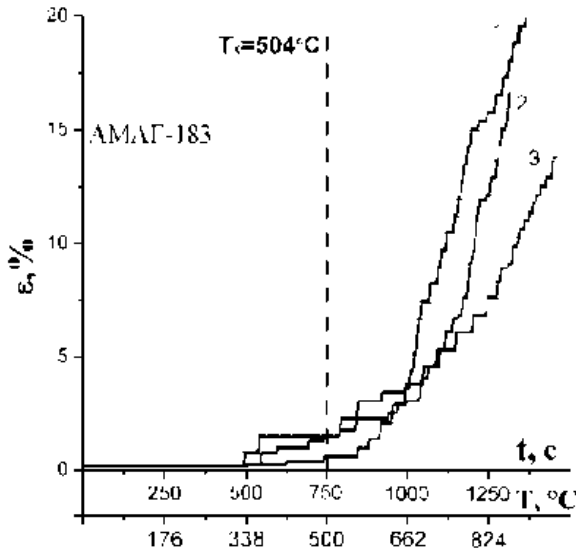

Figure 1 – Dependence of the strain (ε, %) of the time (t, c) for the alloy specimens AMAG-183
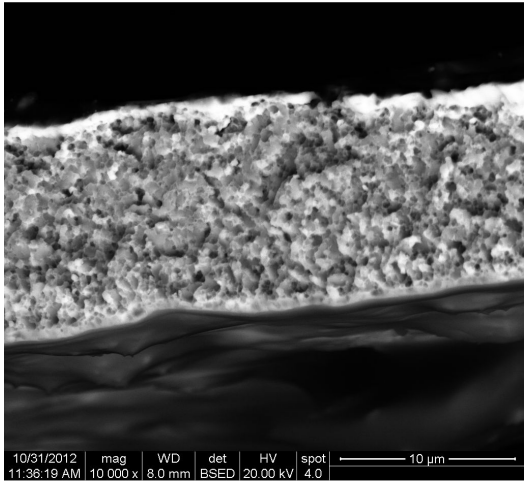(1, 2, 3 - various samples of the same alloy) T_c - crystallization temperature

Figure 2 – Grain structure on the fracture surface of the sample alloy AMAG-186 were heated 600 °C

It is found that the destruction of the samples is viscous at temperatures above 600 °C. It was also noted that the crystal grain textured along the axis of tension. In the destruction of the sample thickness in the formation of sink marks is reduced to 5% from the initial condition, and corresponds to approximately 1 micron.

Formation of steps on the dependence on ε-t connected with the fact that when the crystals separate shear bands locked to them and deformation not develops. This corresponds to a long time-recurrent periods in which the development of the deformation occurs. As the temperature increases the number of crystals and the number of shear bands. Above the deformation temperature crystallization becomes homogeneous and its background blocking strips deformation becomes significantly less time. Creep goes into steady state throughput of the abrupt flow.

Fig. 3 shows the dependence of the strain versus time for alloy AMAG-200. Deformation has a stepwise character.

Samples of the alloy AMAG-200 under specified conditions of the experiment are not destroyed, the relative de-formation samples is 15%.

Fig. 4 shows the morphological peculiarities of the surface of the alloy samples AMAG-186 under-vergnutyh heat 400 °C.
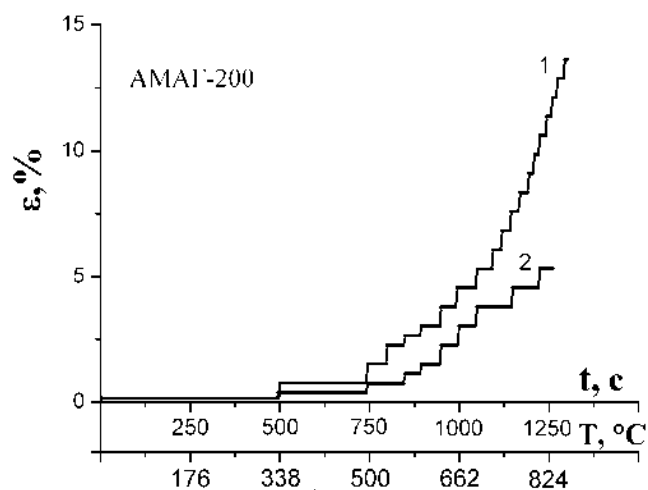
Figure 3 – Dependence of the strain (ε, %) of the time (t, c) for the alloy specimens AMAG-200 (1, 2 – different samples of the same alloy)
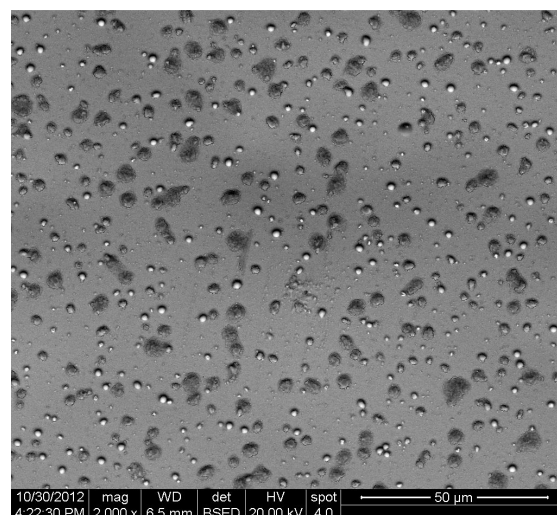
Figure 4 – The formation of oxide particles on the surface of the alloy samples AMAG-186 were heated 400 °C

It can be seen that heating the samples leads to the appearance of the different surface structures, the size of which increases with increasing heating temperature. The element composition is established that they are the oxides of the various components of the alloy. On the surfaces of the alloy AMAG-200 depending on the heating temperature, the appearance of different colors occurs ran-STI.

III. CONCLUSION

Thus, it is experimentally found that the deformation of amorphous and nanocrystalline alloys in transient creep stepwise. It is noted that the amorphous alloys appear first deformation jumps to the crystallization temperature. As the temperature decreases the time between adjacent irregular, and the magnitude of the deformation jump remains almost constant.

REFERENCES

[1] Манохин, А.И. Аморфные сплавы / А.И. Манохин, Б.С. Митин, В.А. Васильев, А.В. Ревякин. М.: Металлургия, 1984. 160 с.
[2] Глезер, А.М. Разработка методики измерения механических свойств тонких ленточных материалов / А.М. Глезер, О.Л. Утевская // Композиционные прецизионные материалы: Тематический отраслевой сборник (МЧМСССР) / под. ред. Б.В. Молотилова М.: Металлургия, 1983. С. 78–82.

SIMULATION OF POLYMOLECULAR ADSORPTION OF HYDROGEN AND OXIGEN ON CARBON NANOTUBES

A. Chashynsky, V. Barkaline

Belarusian National Technical University, Minsk, Belarus

Abstract – Polymolecular adsorption and dissociation of hydrogen and oxygen molecules during adsorption on carbon nanotubes are discussed.

I. INTRODUCTION

The developing of the technology of selective deposition of vertically and horizontally oriented with respect to substrate surface carbon nanotube (CNT) arrays seems one of the most promising achievements of modern nanotechnology. Such arrays may consist of single wall and multiwall nanotubes with diameter from dozens to hundreds nanometers and lengths up to several micrometers and present an example of highly ordered dispersive medium with significant contribution of van der Waals interactions to all thermodynamic properties of the material. Main task of simulation of adsorption on carbon nanotube arrays is the determination of the adsorption type (physical or chemical) and the adsorption characteristics (the location of adsorption sites, adsorption bond lengths and energies).

II. SIMULATION AND DISCUSSION

In present paper quantum mechanical calculations were carried out using density functional theory implementation in NWChem quantum chemistry package [1] in local approximation. It is necessary to stress that DFT usually do not describe long-range behavior of electronic density properly because of the rapid decrease of Gaussian functions at long distances. In NWChem there is special correction accounting van der Waals interaction of distant atoms. This correction is described by additional term in interatomic potential:

$$E_{vdW} = -s_6 \sum_{i=1}^{N_{atom}-1} \sum_{j=i+1}^{N_{atom}} \frac{C_6^{ij}}{R_{ij}^6} \left(1 + e^{-\alpha(R_{ij}/R_{wdW}-1)}\right)^{-1}$$

(1)

Factor s_6 in (1.43) is defined by the exchange-correlation functional and basis set chosen. For exchange potential B3LYP s_6 is equal to 1.05. Then, $C_6^{ij} = \sqrt{C_6^i C_6^j}$ is the factor of dipole-dipole polarization interaction between i-th and j-th atoms, R_{wdW} и R_{ij} are van der Waals radius and interatomic distance correspondingly. Parameter α is used for control the interaction at intermediate distances.

To study multi-molecular adsorption and to take account of the interaction in the adsorbed phase, we used in computation exchange functional of the electron density B3LYP, but in the atomic basis 6-31G. A {16, 16} tube fragment $C_{54}H_{18}$ of larger area was used for the analysis. Quantum mechanically optimized hydrogen molecules were placed above the fragment. The performed computation ascertained that molecular hydrogen is capable of both physical and chemical adsorption on nanotubes and in chemical adsorption, the hydrogen molecule decays into atoms which get attached to different carbon atoms of the nanotube. In physical adsorption, the adsorbed hydrogen forms a lattice, which in the general case is incommensurable with the nanotube lattice when the hydrogen atoms in a molecule are arranged vertically or horizontally with respect to the nanotube surface. In this case it becomes impossible to refer the adsorbed molecule to a certain hexagonal cell of the nanotube, and a single adsorbed hydrogen molecule takes the larger area of the nanotube surface than the area of the stated cell. The effective adsorbing surface of the nanotube diminishes accordingly. It should be noted that in contrast to the molecular-dynamics computation, the vertical orientation of the hydrogen molecules in physical adsorption seems preferable in terms of the energy criterion. For three adsorbed hydrogen molecules, the energy gain in this case is about 21 meV. Moreover, in vertical adsorption, the area taken by one hydrogen molecule is smaller than in the case of horizontal orientation of adsorbed

molecules. The character of hydrogen adsorption on the nanotubes becomes more complicated with due account of chemical adsorption when the hydrogen molecule decays into atoms which bond chemically with the carbon atoms of the nanotube. In physical atomic adsorption, as well as in molecular one, the distance between the hydrogen atom and the nanotube is approximately 2.7 -3.1 Å, while the interatomic distance in the hydrogen molecule is about 0.7 Å. With the distance between the molecule and the nanotube reduced by half (the distance to the carbon atom is 1.4 Å), the hydrogen molecule dissociates and the chemical bonds are formed between the hydrogen atom and the neighboring carbon atoms of the nanotube, with the length of C-H bonds being 1.2 Å. When other hydrogen atoms are added to the system, the chemical bond can either appear or vanish. Various structures of the adsorbate are possible in multi-molecular adsorption, including both chemically and physically adsorbed phases.

Fig. 1 shows the dependence of the depth of the adsorption minimum on the adsorbate structure. It is worth noting that in accordance with the quantum mechanical approach, the value of energy includes the total energy of hydrogen molecules in the ground state. As is seen from the plot, the point 4H2 (four physically absorbed hydrogen molecules) indicates the loss in energy (4.502 eV) in comparison with the structure 3H2 H H (three physically adsorbed hydrogen molecules plus one – chemically adsorbed with dissociation). Thus, physical adsorption is preferable as it gives the energy minimum. It should also be mentioned that in physical adsorption, the mutual orientation of the hydrogen molecules is not fixed. In this regard, taking account of the rotational degree of freedom of the adsorbed phase may appear important for the analysis of the adsorption characteristics of nanotubes. This fact can obscure the kinetics of adsorption processes on nanotubes.
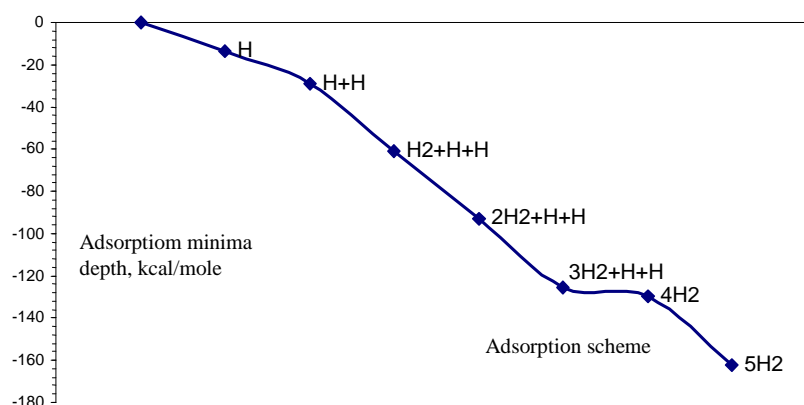
Figure 1 – Adsorption energy for different structures of the adsorbed phase.

The obtained data enable us to state that the hydrogen molecules form quasi-regular structures on the basis of the triangle lattice with the period independent of the period of the graphene lattice.
Since in process of adsorption of hydrogen molecules, they may dissociate into atoms, particular attention was given to studying adsorption of two hydrogen atoms on the external wall of the nanotube {16,16} in a wide range of interatomic distances and the distances between the atoms and the nanotube. The hydrogen atoms move along the basis vector of the graphene lattice, the motion starts far from the carbon atom. The height of the hydrogen atoms over the nanotube fragment is from 0.8 Å до 2.6 Å, the van der Waals interaction is taken into account. The binding energy of the hydrogen atoms on the nanotube surface is calculated as follows:

$$E_{Sorb} = E_{System} - E_{Tube} - 2 \cdot E_{H}$$

(2)

where E_{System} is the energy of the nanotube fragment {16,16}, E_{Tube} is the energy of the structure consisting of the nanotube fragment 16×16 and hydrogen atoms, E_{H} is the energy of the hydrogen atom. The research results are given in Figure 2.
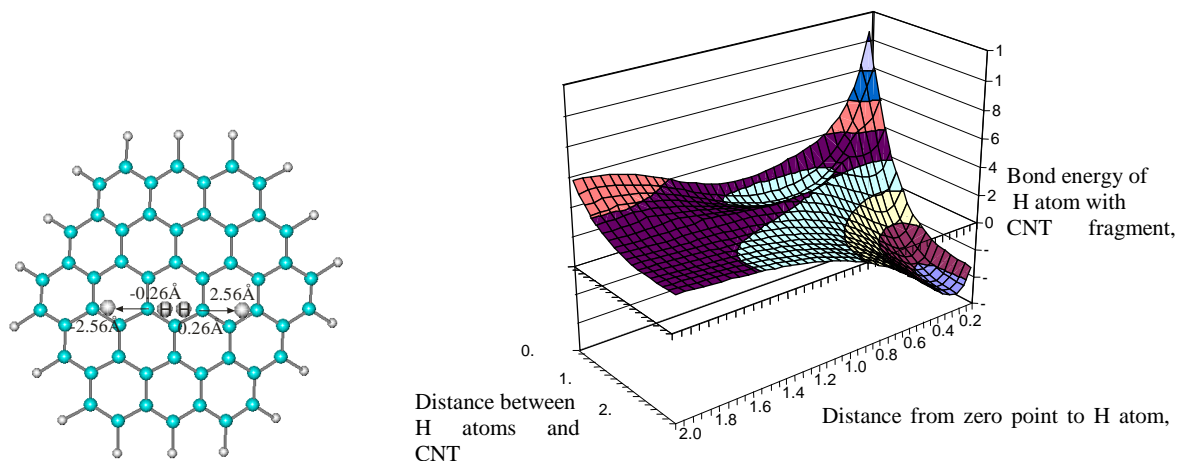
Computation was made on the grid cluster BY-BNTU.

Figure 2 - The structure of the system "two hydrogen atoms – the fragment of carbon nanotube" and the dependence of the hydrogen binding energy with the CNT fragment on the position of the hydrogen molecule over the surface of the nanotube fragment

III. CONCLUSION

The simulation task of the adsorption of gas molecules on carbon nanotube arrays has hierarchical nature. It begins at quantum mechanical level where electronic properties of adsorption system are studied and the physical or chemical character of adsorption is determined with calculation of corresponding parameters of adsorption sites. Then interaction in adsorbed phase is studied and spatial distribution of adsorbed molecules is obtained. In the cases where physical adsorption dominates the molecular mechanics methods can be used for these studies.

REFERENCES

[1] Valiev M., Bylaska E.J., Govind N., Kowalski K., Straatsma T.P., van Dam H.J.J., Wang D., Nieplocha J., Apra E., Windus T.L., de Jong W.A. (2010) NWChem: a comprehensive and scalable open-source solution for large scale molecular simulations. *Comput. Phys. Commun.* **181**, 1477.

NOVOSADOV'S METHOD OF MOLECULAR HARMONICS RESEARCH FOR QUANTUM MECHANICS COMPUTER MODELING

Ya. Douhaya

Belarusian National Technical University, *Minsk*, *Belarus*

Abstract – Analytical solving of single-electron Schrödinger equation in Columb multi-nuclear field proposed by Novosadov results with molecular orbitals represented as linear sum of hydrogen like orbitals centered in atom cores. Author research a possibility of Novosadovs method application for modeling of atoms and molecular systems. Results of calculations of H2+ electron density and interaction energy dependence on distance for H-H, C-C and metan- ch4 are represented.

I. INTRODUCTION

For solutions of the Schrödinger equation, various approximate methods including Self Consistent Field and Density Functional Theory are using. To construct the wave function Gaussian orbitals are used, which are poorly reproduce the electron density distribution in atoms and molecules and have the wrong asymptotic behavior at a distance from the nucleus. Novosadov proposed methods of construction and algorithms for computing multi-center matrix elements in the basis of atomic orbitals with the exponential asymptotic behavior, which include Slater hydrogen-like functions, and Bessel functions. Developed algorithms are universal for all orbital types are numerically stable and allows to achieve any accuracy.

II. SINGLE-ELECTRON SCHRÖDINGER EQUATION SOLVING

For solving problem of one electron moving in the fixed nuclei field Shcrodinger equation could be represented as

$$\left(\frac{1}{2} p^2 - \sum_{\alpha=1}^{N} Z_\alpha r_\alpha^{-1} \right) \psi = E\psi$$

(1)

where $r_\alpha = \left| \vec{r} - \vec{R}_\alpha \right|, \vec{r}, \vec{R}_\alpha$ - electron and α- nuclei coordinates correspondingly.

In the electron pulse space equation (1) is represented as integral equation:

$$\frac{1}{2} p^2 \psi(p) - \frac{1}{2\pi^2} \sum_{\alpha=1}^{N} \int Z \exp[i(\vec{p} - \vec{p}\,')\vec{R}_\alpha\,](\vec{p} - \vec{p}\,')^{-2} \psi(\vec{p}\,')d^3\vec{p}\,' = E\psi\vec{p})$$

(2)

Equation (2) can be transformed to angle pulse variable by stereographic projection on the Riemann sphere:

$$p_0\tau(\alpha)\psi(\alpha,\theta, \ ) = (2\pi^2)^{-1}\int Z(\vec{p},\vec{p}\,')[4\sin^2(\omega/2)]^{-1}\Psi(\alpha',\theta', \ ')d\Omega_4'$$

(3)

,

After applying bilinear expansion

$$[4\sin^2(\omega/2)]^{-1} = \sum_{n=1}^{\infty}\sum_{l=0}^{n-1}\sum_{m=-l}^{l} n^{-1}\Psi_{nlm}(\Omega_4)\Psi_{nlm}(\Omega_4\,')$$

(4)

eq. (3) leads to matrix equation

$$Tc - p_0 Ic = 0, (5), \text{ where } p_0 = (2|E|)^{1/2}$$

Finally, discrete electron specter solving reduced to matrix equation

$$A(p_0)\vec{c} - p_0 I \vec{c} = 0 \tag{6}$$

Elements of matrix A are calculated as

$$A_{\alpha n l m}^{\alpha' n' l' m'} = [Z_\alpha Z_{\varepsilon'}(nn')^{-1}]^{1/2} S_{n l m}^{n' l' m'}(\vec{R}_{\alpha \alpha'}), \tag{7}$$

$$S_{\alpha n l m}^{\alpha' n' l' m'} = \sum_{NLM} \pi^{1/2} p_0^{-3/2} u_{NLM}(\vec{R}_{\alpha \alpha'}) \, \varUpsilon(n'l'm', nlm; NLM), \tag{8}$$

$$T(n'l'm', nlm; NLM) = (2\pi^2)^{-1} \int 4 p_0^2 (p_0^2 + p^2)^{-1} \psi_{n'l'm'}(\varOmega \varOmega)_{nlm}(\varOmega \varOmega)_{NLM}(\varOmega \varOmega) d \tag{9}$$

Where $u_{NLM}(\vec{R})$ - hydrogen like orbital, and R_{aa} – distance between Ra and Ra atoms centers.
Fixing parametr p0 in the matrix elements we can find specter p0i(p0). Points where the curves p0i(p0) cross line y=p0 corresponds solving of eq. (6) and consequently eq. (3).
When parameter p0 and eigvectors are found wave function can be introduced as

$$\Psi(r) = p_0^{-1} \sum_{\alpha=1}^{N} \sum_{nlm} (Z_\alpha / n)^{1/2} c_{\alpha n l m} u_{nlm}^*(r - R_a) \tag{9}$$

Where c_{alnm} is a_{lnm} element of eigenvector c and

$$N \in [|n - n'| + 1, n + n' - 1], \quad L \in [|l - l'|, l + l'], \quad M = m - m'; \quad N > L, \quad L \ge |M|$$

III. ATOMIC SYSTEMS PROPERTY CALCULATIONS

On the figure 1 specter p0i(p0) calculated for the molecula H2+ and C2 are represented. Matrix A degree is reduced to 10x10 by setting maximum n to 2. According to figure 1 a) there are 4 solution for p0 . Others curves cross line y=p0 only in po=0.
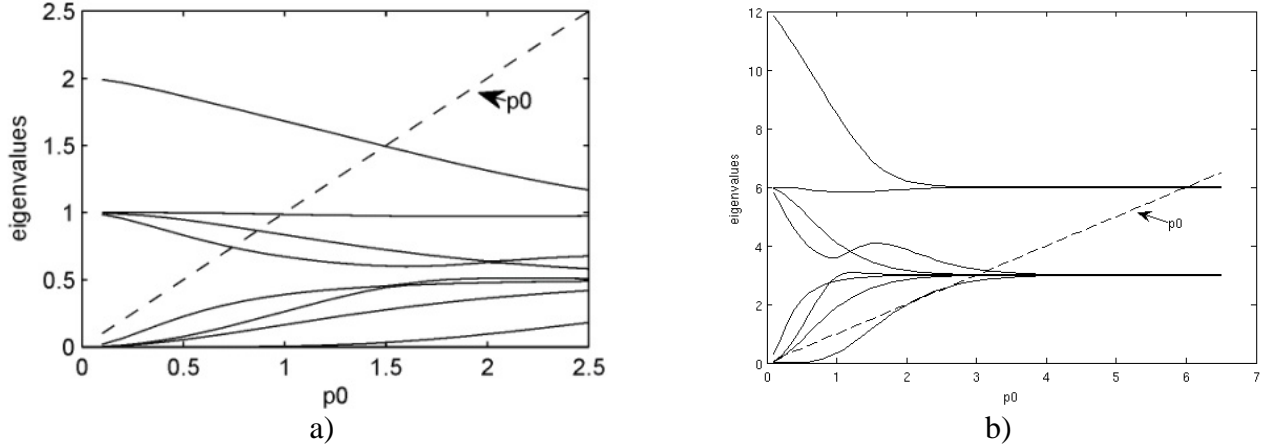
Figure 1 – p0i(p0) calculated for a) H2+ b) C2

On the figure 1 b there are 10 solutions for p0 corresponding to energies of ten orbitals formed from atom C orbitals and four additional solutions where curves cross the line y=p0 corresponding higher energies that may be caused by matrix reduction and not have physical sense.

The value of two lower wave functions square is calculated for the systems of two hydrogens atoms where distances between atoms are 1.7 and 5 a.u. (figure 2 a,b).
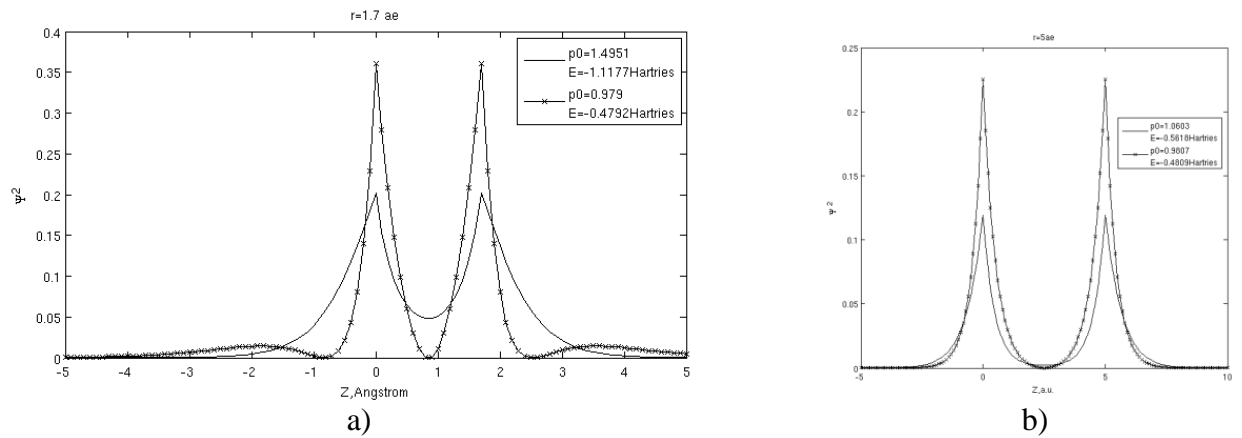
Figure 2 – Wave functions square calculated for the systems of two hydrogens atoms

Figures 2 a,b shows that molecula H2+ has binding and antibonding orbitals which trend to atomic orbitals when the distance between atoms increase. Calculation of one-electron energy dependence in field of two proton represented on figure 3 shows that the Matrix A reduced to n=1 is insufficient to correct calculation of electron state.

When the p0 is maximum of possible solutions all eigenvalues of matrix A are smaller than p0 and when the p0=0 all eigenvalues are biger. Therefore the number of solutions in the field more than some value can be calculated as the number of eigenvalues curves above the line y=p0 for p0=value when there are no more than one crossing with the line y=p0 for every curve.

III. CONCLUSION

Developed by the authors computer implementation of the method of molecular harmonics can solve the one-electron problem, which has important theoretical value in quantum chemistry. The calculated energies and the lower orbital wave functions of simple atomic structures are consistent with those of experimental and theoretical studies.

REFERENCES

[1] P. B. Johns, "A symmetrical condensed node for the TLM method," *IEEE Trans. Microwave Theory Tech.*, vol. MTT-35, pp.370-377, Apr. 1997.

[2] V. Trenkic, C. Christopoulos, and T.M. Benson, "Efficient computational algorithms for TLM," in 1*st Int. Workshop TLM*, Univ. Victoria, Canada, Aug. 1995, pp. 77-80.

[3] C. Christopoulos, *The transmission-Line Modeling (TML) Method*. Piscataway, NJ: IEEE Press, 1995.

MOLECULAR DYNAMICS SIMULATION OF CARBON NANOTUBE ARRAYS RESPONSES ON MECHANICAL AND ELECTRICAL HIGH FREQUENCY FORCES

A. Pletezhov, *V. Barkaline*
Belarusian National Technical University, *Minsk*, *Belarus*

Abstract – Torsional mode excitation of carbon nanotube bundle in high frequency electric field is revealed by molecular dynamics numerical experiment. Signal propagation in linear chain of carbon nanotubes linked by van der Waals forces is discussed.

I. INTRODUCTION

Study of carbon nanotube bundles behavior in electromagnetic field is of essential interest in the design of nanodevices of radio and UHF frequency regions [1]. This interest is caused by the existence of resonant properties of carbon nanotubes (CNT) and significance of van der Waals interactions in determining of the dynamics of CNT arrays, which lead to strong nonlinearity in their behavior in electromagnetic and acoustic fields.

The most applicable method of simulation of CNT based nanosystems seems to be the method of molecular dynamics, which implies the calculation of trajectories of all atoms of the systems by numerical integration of classical equations of motion with empirically defined force fields describing interatomic interactions [2].

II. EXCITATION OF CNT BUNDLES BY HIGH FREQUENCY ELECTRIC FIELD

In the presented paper we used the molecular dynamics package NAMD (NAnoscale Molecular Dynamics) [3] with graphical interface VMD (Visual Molecular Dynamics) [4], which are freely available. NAMD package uses the CHARMM force field developed mainly for the description of intermolecular interactions in biopolymers. Its usage for CNT array modeling seems to be proved too.
The system under study was the array of seven parallel nanotubes cupped from one side with length 200 Å and diameter 13 Å with chirality parameters {10,10}. CNTs formed regular triangle lattice with minimal intertube distance 6 Å (Figure 1, initial state picture). Nanotube cups can have manually introduced electrical charges, which are totally compensated by opposite charges at graphene layer placed under the array. Harmonically varying charges on the array and graphene layer simulated the external electric field with frequency 25 GHz. Simulation results for several times are presented in Figure 1 too. Total simulation time was 41 ps.

The data presented show the excitation of binding modes as well as torsional mode of CNT bundle. The last observation seems to be new and unexpected. Besides that the small amplitude vertical motion of CNT was observed with frequency much more high then frequency of charging which corresponds to the excitation of vibrational eigen mode of traction-and-compression type.
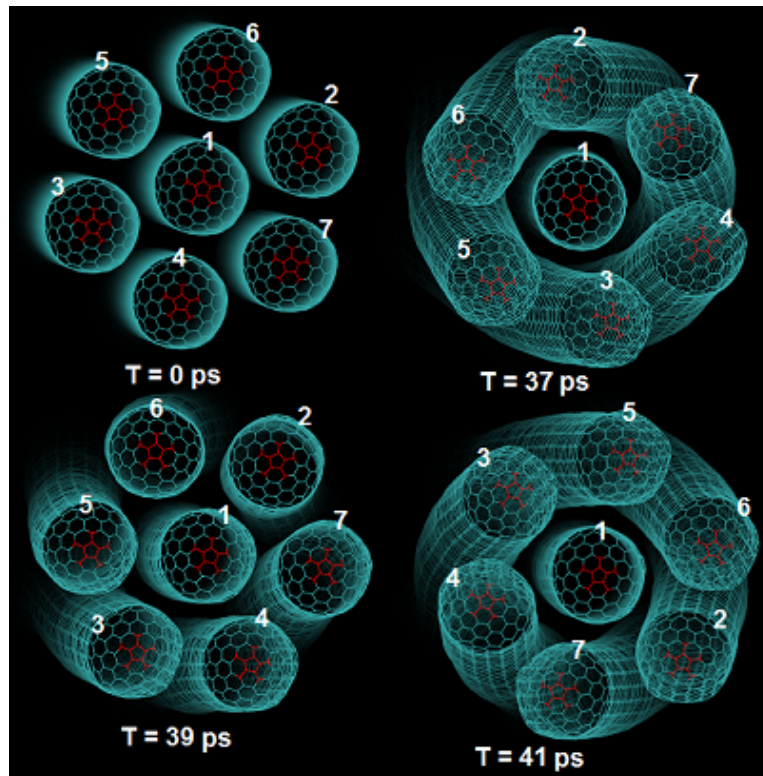
Figure 1 – Torsional mode of CNT bundle under the action of an electrical field

III. PROPAGATION OF EXCITATION IN CNT LINEAR CHAIN

In Figure 2 the results of simulation of the mechanical excitation of CNT linear chain are presented. The system under study was the array of seven one-side cupped nanotubes with length 200 Å, diameter 13 Å and chirality parameters {10,10}. Before geometry optimization parallel CNTs formed linear chain with minimal intertube distance 14 Å. After such optimization one get the array configuration presented at the first picture in Figure 2. Total simulation time was 100 ps.
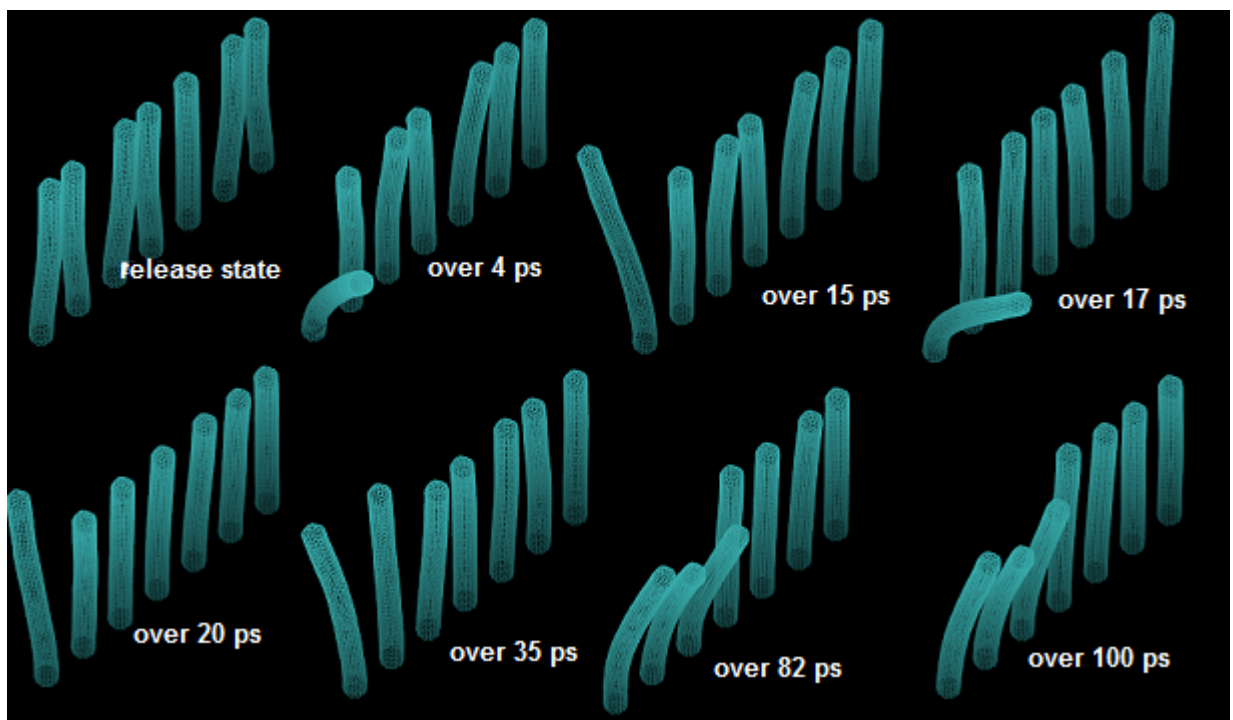
Figure 2 – CNT chain excited by giving the velocities
to the atoms on the cup of first tube in transversal direction

The idea of numerical experiment was the mechanical excitation of the array by giving transversal velocity to the atoms of the cup of first tube and observing the propagation of excitation through the chain due to van der Waals interaction. Finite state of the array is interpreted as the effect of input signal. Varying the signal one gets various output state of the array. In principle, such array plays a role of analogous memory nanodevice.

It is necessary to note that displacement amplitude of the tubes decreases with the distance along the chain and for fifth, sixth and seventh tubes the displacements have not component clearly corresponding to the input signal. The response to the signal does not propagate further forth tube. Additional studies are needed for clarification this damping and memory effect. In principle such linear array could be used as learning element of nanosize artificial neuronal network.

IV. CONCLUSION

Numerical experiments on the electrical and mechanical excitation of carbon nanotube arrays of various form are realized with the NAMD+VMD simulation packages. For CNT bundle in high frequency electric field the excitation of torsional mode is discovered. For CNT linear chain array the damping of the mechanical excitation is found and boundary memory effect is described.

REFERENCES

[1] Barkaline V., Abramov I., Belogurov E., Chashynski A., Labunov V., Pletezhov A., Shukevich Y. Simulation of Carbon Nanotubes and Resonant Excitation of Their Mechanical Vibrations of by Electromagnetic Field for Nanoradio Applications / V. Barkaline [et al.] // Nonlinear phenomena in complex systems, vol. 15, no. 1 (2012), pp. 23 – 42.

[2] Frenkel D., Smit B. Understanding Molecular Simulation. From Algorithms to Applications – London: Academic Press, 2002, 638 p.

[3] Phillips, J.C. Scalable molecular dynamics with NAMD / R. Braun, W. Wang, J. Gumbart, E. Tajkhorshid, E. Villa. C. Chipot, R.D. Skeel, L. Kale, K. Schulten. // J. Comp. Chem, 2005. P. 1781 – 1802.

[4] Humphrey, W., Dalke, A. and Schulten, K., "VMD - Visual Molecular Dynamics", J. Molec. Graphics, 1996, vol. 14, pp. 33-38.

AB-INITIO SIMULATION OF VANADIUM OXIDE ELECTRONIC PROPERTIES

V. Koleshko[1], A. Gulay[1], V. Gulay[1],
I. Bobachenok[1], O. Kozlova[2], V. Nelayev[1]
[1]Belarusian National Technical University, Minsk, Belarus
[2]Belarusian State Universities of Informatics and Radioelectronics, Minsk, Belarus

Abstract – The modeling of the electronic properties of vanadium oxides with the effect of the Mott—Hubbard was conducted. Software package VASP was used as the simulation tool, in particular,r method of augmented plane wave (PAW-method). Calculated electron densities and the band structures of vanadium compounds of homologous series V_nO_{n+1} and V_nO_{n-1} are presented.

In order of effect high quality of NDTCS-2013 Conference Proceedings the authors are requested to follow instruction given in this sample paper.

The crucial feature of some transition compounds is a jump of conductivity with increasing temperature or pressure, which can reach many orders of magnitude (the effect of Mott-Hubbard). Mott-Hubbard insulators are crystals with dielectric properties, the manifestation of which connected with the strong electron-electron interaction, but not with the influence of the periodic field of the lattice crystal (as in usual insulators or semiconductors). This state realizing in the case when the energy U of the electron-electron (Coulomb) interaction is greater than the average kinetic energy of the electrons. In that case, a measure became the width of the allowed band W. A simple band diagram of a solid state is suitable, when U < W, and, if U > W, the energy band may be partially filled with electrons, as in metals, but electrons located on adjacent atoms inhibit to the movement of electrons required to charge transfer. Due to the manifestation of the repulsion forces they localize each electron in its atom that actually turns into a dielectric material.

Typical representatives of materials with the "metal-insulator" transition are homologous series of vanadium oxides V_nO_{n+1} and V_nO_{n-1}. A software package VASP (Vienna *Ab-Initio* Simulation Package) was used as a simulation environment of its electronic properties, which implements *ab-initio* approach to quantum-mechanical calculations in molecular dynamics (MD). *Ab-initio* method uses pseudopotentials system with sets of basic elements of plane waves. This approach, implemented in the VASP, based on the local density approximation (a free energy as a variable value) and accurate estimation of instantaneous electronic ground state in each of MD-step and also using of effective diagonalization of the matrix schemes and effective Puley mixing.

The interaction between ions and electrons in the software package is described by Vanderbilt ultrasoft pseudopotential (US-PP), or a method augmented plane wave (PAW). Both methods allow for a significant reduction of required number of plane waves in the transition metal atoms. Besides, VASP relatively simple calculates strength values, which are used for relaxation of atoms into ground state. VASP also allows to trace the displacement of the individual particles in the system and evaluate their self-diffusion coefficients, to calculate the average change time of the nearest neighboring particles, and to identify a range of other physical properties. Particularly attractive in the study of active sensor materials is the ability of using VASP to calculate the dependences of these characteristics on the temperature and the external and internal elastic deformations.

The main methodology used in VASP involves the solution of the Schrodinger equation for the electron-nuclear subsystem of the modeled structure and evaluation of the final full energy of the system, forces and other parameters and values. The method used in this paper is the PAW-method, which allows properly calculating the lattice constants, adequately estimating spin-polarization and physical properties of the materials. The problem of modeling atomic structures and electronic properties of rare-earth compounds in a general form involves finding optimal calculation algorithms in the VASP software package, estimating input parameters of the modeled system for attaining the required precision and selecting a methodology for adequate determination of properties of the sensory materials in question.

The idea of the used algorithm is that the calculations start from a relatively small number of atoms in the modeled crystallite, afterwards based on these results the structure is translated to the required size. Although before that a number of tests are run, for example the optimal number of points that determine the degree of fragmentation of the reciprocal space is calculated, the minimum energy of the modeled system is evaluated as well. The number of points determines the precision of the determined atomic coordinates in the lattice: for dielectric materials ten points per unit cell are enough.

A cubic lattice structure of the F_{m3m} (No. 225) space group was used to represent a primitive cell of VO (Fig. 1). The following procedures were used for modeling vanadium oxides: creating input files with the simulation task; relaxation of vanadium oxide lattice structure; analysis of the compounds lattice unit cell; determination of electronic properties of vanadium oxide. The static self-consistent potential of the crystallographic structure of the compound was calculated after the relaxation procedure. The results were obtained in the form of DOS and zone diagram structure at the k-points of the Brillouin zone: L–Γ–M–W–X–L (Figs. 2, 3).

The unit cell V_4O_9 was performed using the orthorhombic crystal structure of P_{nma} (No. 62) space group. The Fermi level of compound is 0.57 eV, a direct transition value is 1.05 eV at T *k*-point (in the calculation of the band structure diagram on the following *k*-points of the Brillouin zone: X-D-Z-T-R-S-X). V_2O_5 orthorhombic crystallographic structure of the space group P_{mmn} (No. 59) was used to represent the unit cell. The Fermi level of V_2O_5 is 0.51 eV, indirect transitions was observed at R-Γ and R-Y k-points (traversal path S-D-R-Y-S). VO_2 compound characterized with an indirect transition with value 0.9 eV, wherein the maximum of the valence band is at R k-point, and the minimum of the conduction band is at M k-point (traversal path - Z-L-M-X-R-Z).
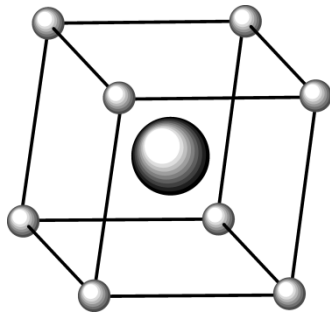
Figure 1 – Primitive unit cell of VO:
⬤ — vanadium, ◯ — oxygen
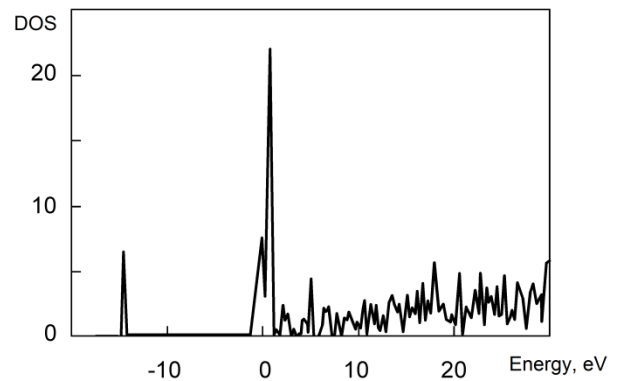
Figure 2 – VO density of states; Fermi level is equal to -2,22 eV and sets at zero point
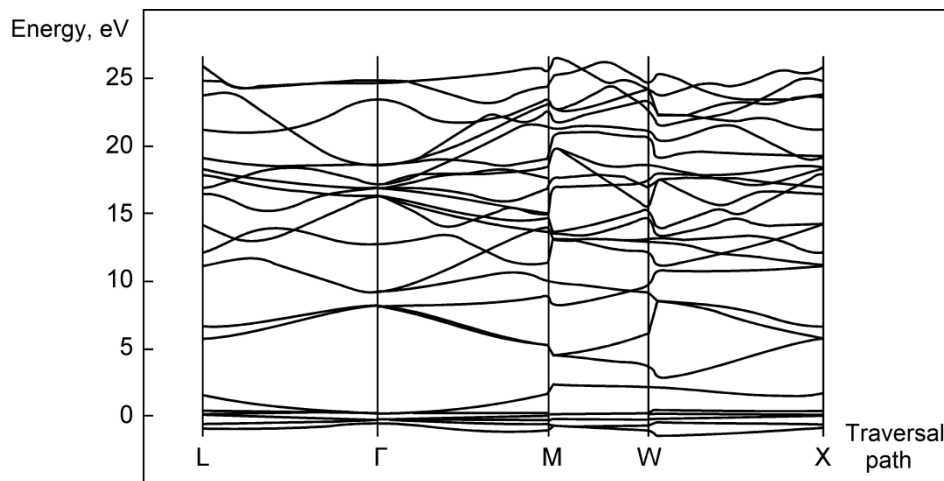

Figure 3 – Zone diagram of VO structure

The analysis of the zone diagram shows that VO has an indirect gap transition with a value of 0.38 eV, wherein the maximum of the valence zone is at the M k-point and the minimum of the conduction zone is at the W *k*-point.

INVESTIGATION OF ELECTRONIC STRUCTURE
OF HEUSLER ALLOYS: CUBIC AND TETRAGONAL CELLS

T. Breczko[1], J. Tamuliene[2]
[1]*University of Bialystok, Poland*
[2]*Vilnius University, Institute of Theoretical Physics and Astronomy, Lithuania*

Abstract – The work is devoted to the Heusler alloys as a candidate for applications in spintronics. On the basis of experimental studies the electronic structure of these alloys by computer simulations were carried out. Hence, the purpose of our work is to simulate and to explain the variety of structural properties of the Ni_2MnGa and Co_2MnGa compounds by using state-of-the-art computational ab-initio methods. The total energy calculations for the cubic and the tetragonal structures, band structure and its nature and magnetizability have the compounds are investigated. The obtained results will explain the dependence of the magnetic properties of the alloys on the geometrical structure as well influence of Co and Ni on these properties.

I. INTRODUCTION

Half-metallic ferromagnetic alloy have been studied as a candidates for the metal-based the spintronic-logic devices. Among many half-metallic ferromagnetic materials special attention has been done on Heusler alloys such as Ni_2MnGa and Co_2MnGa that show high Curie temperature and high spin polarization [1-5]. Several studies by means of X-ray and neutron diffraction measurements indicate that the alloys present $L2_1$ structures with mainly ferromagnetic ordering [6]. However, R. J. Kim and et al. found a well-ordered crystalline state, a disordered state, and crystalline state with an intermediate order and exhibited influence of structural order on the physical properties of the Co_2MnGa films [7]. The similar phenomena for the Ni_2MnGa are described in work [8]. More often, the substrate temperature is mentioned as having dramatic effects on the structural ordering and magnetic properties, however the effects of structural disorder on the various physical properties of these alloys are not fully understood. Moreover, the dependence of electronic structure on the alloy geometrical structure is insufficiently described although it could be the main reason to understand what can be responsible for many of the alloy properties.

Hence, the purpose of our work is to simulate and to explain the variety of structural properties of the Ni_2MnGa and Co_2MnGa compounds by using state-of-the-art computational ab-initio methods. The total energy calculations for the cubic and the tetragonal structures, band structure and its nature and magnetizability have the compounds are investigated. The obtained results will explain the dependence of the magnetic properties of the alloys on the geometrical structure as well influence of Co and Ni on these properties.

II. RESULTS

At present time quantum mechanical investigation of the Ni_2MnGa and Co_2MnGa possessing $L2_1$ structure were investigated. The views of the structures are presented in Fig. 1. The aim of the first investigation is to establish how the electronic properties of the alloys are changed when the Ni atoms in the lattice are changed by the Co atoms and vice versa.

Let us to remember that the Co and Ni atoms are different not only due to different electrons but also due to electronic configuration. The Co atom electronic configuration is $[Ar]4s^23d^7$ while Ni one is $[Ar]4s^23d^8$ and $[Ar]4s^13d^9$. Thus, there is some disagreement as to which the Ni electronic configuration should be considered the lowest energy configuration [9-11]. Of course, the isolated atoms and atoms in the compounds electronic configurations are different, but it could be essential to explain properties of the compound that is related with charge redistribution.

First, our investigated systems are open shell systems due to odd number of the Mn atoms. However, the highest electronegativity numbers, what indicate ability an element attract electrons toward it, are the Co and Ni atoms in the investigated compounds. Indeed in our investigated Ni_2MnGa compound the largest negative charge possesses Ni atoms, while charge of the Ga and Mn atoms is positive or negative (Fig.1). Moreover, the charge is not distributed equally that leads to appearance of

the high dipole moment (144.67 Deby) with large dy component (dy=139.63 Debye) that could indicate concentration of the negative charge and, as consequence, large uncompensated spin presence.

Indeed, the largest spin densities are obtained on the Mn atoms that electronegativity is smaller than Ni (Fig. 2). Thus, we predict, that it could be happens due to an electronic configuration changes and different oxidation states of the atom presented in the different places of the investigated compound. Hence, the Ni atoms attract the electrons to form chemical bonds, while an additional electron is located on Mn atoms mostly due to their configuration of d orbital [12]. It is necessary to remember that only Mn atom could have oxidative state such as -1, -2 or -3, while other atoms of the compound oxidative state is positive and indicate that theses atoms may not accept an additional electron. It is necessary to pay attention to different spin densities on the Mn atoms located in different places of the investigated compound (Fig.2). Thus, the results obtained indicate geometrical structure of the compound is important for their magnetic properties.

The above conclusion is confirmed by the investigation results of the $Ni_2Mn_{0.375}Ga_{0.625}$ compound (Fig.3). It is clear to see the largest spin density on the Ni atom, when Mn atom is changed by Ga.
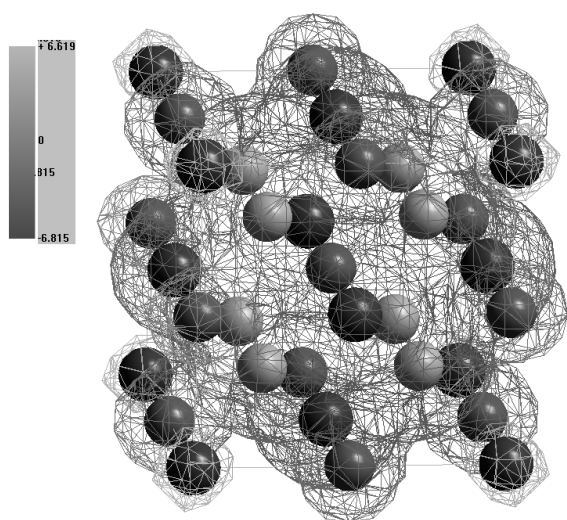
Figure 1. The 3D Mapped Isosurface of Electrostatic Potential of the Ni_2MnGa compound. The light grey colored bubble is Ni, dark grey – Mn and black –Ga
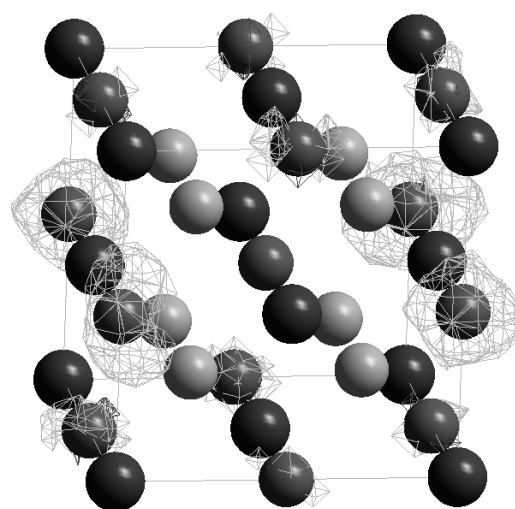
Figure 2. The 3D Isosurface of Total Spin Density. The light grey colored bubble is Ni, dark grey – Mn and black –Ga.
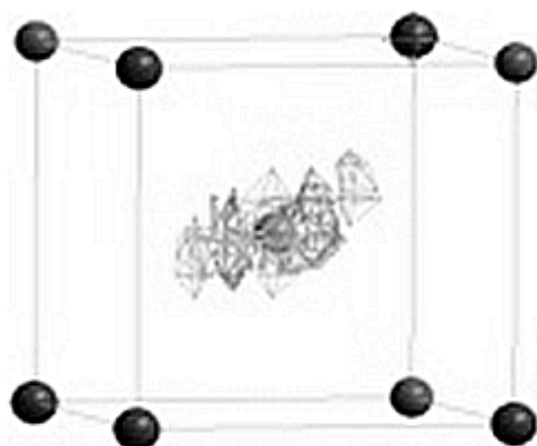
Figure 3. The 3D Isosurface of f the total spin $Ni_2Mn_{0.375}Ga_{0.625}$ alloy. The light grey colored bubble is Ni, dark grey – Mn and black –Ga.

It is necessary to mention that the last one system is closed shell system, i.e. there is no free electron. In this case, the Ni atom possessing the highest electronegativity numbers attracts electrons toward it. However the spin density on the Ni atom is equal to 0 approximately due to several reasons: the attracted electrons may form chemical bonds and there is no the free electron

CONCLUSION

The primary results of the investigations exhibited that the spin density of the Ni$_2$MnGa alloy are atom placement depended.

REFERENCES

[1]   S. Fujii, S. Sugimura, S. Ishida, S. Asano, J. phys: condens. Matter **2** (1990) 8583.

[2]   T.M. Breczko, V. Nelayev, K. Dovzik , M. Najbuk and M. Bramowicz, Experimental investigation and computer simulations of selected physical properties of the Ni$_2$MnGa alloys // Proc. of SPIE Vol.**7377** (2008).

[3]   T. Breczko, V.V. Barcaline, Ya. V. Douhaya. Electronic properties of Heusler Ni-Mn-Ga alloys, Фазовые превращения и прочность кристаллов, 6-я Конф., Черноголовка, (2010) 79.

[4]   T. Breczko, V.V. Barcaline, R.M. Grechishkin, V.V. Nelayev, Magnetic properties of Ni$_2$MnGa alloy// Materials Physics and Mechanics **9** (2010) 53.

[5]   Breczko Teodor, Barcaline Viatcheslav and Douhaya Yana, Modeling of smart material properties of Heusler alloys, Material Science Forum Vols. 738-739, pp 426-430 (2013).

[6]   Ayuela, J. Enkovaara, K. Ullakko, R. M. Nieminen, J.Phys.: Condens. Matter **11** (1999) 2017.

[7]   R. J. Kim Y. J. Yoo, K. K. Yu, T. U. Nahm, Y.P. Lee, Y.V. Kudyavtsev, Oksenenko, J. Y. Rhee, K.W. Kim, Journal of the Korean Physical Society, **49**, 3, (2006) 996.

[8]   Alexey T. Zayak, Ph.D. thesis "A first-principles investigation of the magnetic, structural and dynamical properties of Ni$_2$MnGa",(2003).

[9]   R.H. Petrucci et al. "General Chemistry" (8th ed., Prentice–Hall 2002) p.950

[10] NIST Atomic Spectrum Database .

[11] G.L. Miessler and D.A. Tarr, "Inorganic Chemistry" (2nd ed., Prentice–Hall 1999) p.38

[12] S. E. Kulikova, S.V. Eremeev, T. Kakehita, S. S. Kulikov, G. E.Rudenski, Materials Transactions, **47**, 3 (2006), 599.

ELECTRONIC PROPERTIES OF QUASI-TWO-DIMENSIONAL MOLYBDENUM DISULFIDE WITH COBALT IMPURITIES

O. Kozlova, V. Nelayev

Belarusian State University of Informatics and Radioelectronics, Minsk, Belarus

Abstract – In variety of new materials a special place hold materials with nanoscale structure. Two-dimensional materials has attached a great attention due to its outstanding physical phenomena occurred at the nanolevel. There is a big interest in transition-metal dichalcogenides, due to their layered structure; they have extremely anisotropic properties, and therefore an intercalation processes easy to conduct. Reduced dimensionality can sometimes lead to magnetic behavior in systems, which are not magnetic in the bulk. That is why our investigation is aimed to determine the possibility of molybdenum disulfide (MoS_2) magnetic properties manifestation under cobalt (Co) impurities condition. Electronic properties study of quasi-two-dimensional structure of MoS_2 with Co impurities are presented. Calculations were carried out using VASP (Vienna *Ab initio* Simulation Package).

I. INTRODUCTION

Recent studies have demonstrated the important role of nanostructures in various fields of science and technology. Thus, molybdenum disulfide is a ''layered'' transition metal dichalcogenide semiconductor with an indirect band gap that has attracted considerable interest in connection with its catalytic and electronic properties [1]. The ''layered'' structure of MoS_2 (Fig. 1) is formed by a S–Mo–S sandwiches bonded together by weak Van-der-Waals forces (hexagonal unit cell parameters: a = 3,12 Å; b = 3,12 Å c =11,98 Å) [2]. The two-dimensional unit MoS_2 cell has one Mo atom and two S atoms. Each of the Mo atoms is coordinated to six S atoms in a triangular prismatic form. However, considering that Mo layer doesn't lies in one plane with S layer it would be more correctly to conclude quasi-two-dimensional structure of MoS_2. Because of the weak van der Waals interactions between the sheets of sulfide atoms, MoS_2 has a low coefficient of friction, resulting in its lubricating properties. MoS_2 may be mechanically exfoliated using scotch tape to create 2D MoS_2 samples, similarly to graphene. MoS_2 has a number of unique properties, which allow it potential applications in transistors, flexible displays, and optics [3].
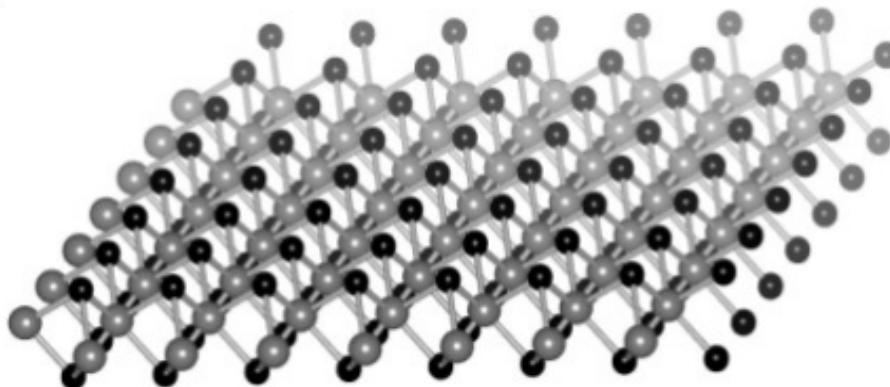

Figure 1 – Crystallographic structure of quasi-two-dimensional MoS_2

II. METHODOLOGY

Nowadays a very important further step in electronic properties prediction is development of modern methods of materials simulation. Thus, further progress in understanding of physical phenomena at nanoscale level may be realized by use of *ab initio* simulations taking into account difficulties of experimental nanoobjects investigations.

A rather interesting problem is the investigation of nanostructured materials with impurities of magnetic metallic fragments, due to which manifestation of significant magnetic properties became possible as it was with the ternary compound $TlMeX_2$ [4].

The research presented in this paper aims to investigate the electronic and magnetic properties of quasi-two-dimensional molybdenum disulfide with impurities of cobalt, a well-known ferromagnetic metal. The study of spin-dependent properties of two-dimensional structure of MoS_2 with Co clusters impurities was carried out by means of a software package VASP (Vienna *Ab initio* Simulation Package) [5, 6]. The interaction between the ions and electrons in the simulated system is described by the Plane Augmented Waves (PAW) method. With the use of program package VASP it is possible to calculate the forces and stresses, which are used to relax atoms into their ground state. GGA-PBE pseudopotentials were applied for description of the interaction between the atomic cores and electrons. The calculations were performed using periodic conditions. In order to exclude the influence of impurities on each other a super-cell with size of 6×6 hexagonal unit cells of MoS_2 was created. Energy cutoff of 500 eV for the plane-wave expansion has been used.

III. RESULTS AND CONCLUSION

Calculation results analysis of electronic density states and band diagram (Figs. 2, 3) of the perfect MoS_2 quasi-two-dimensional structure and MoS_2 structure with two Co-impurities shows the presence of additional energetic levels located near to band gap midpoint. Co impurity cluster increasing causes a sharp narrowing of the band gap to 0.91 eV and increasing of the magnetic moment value from 0.0008 µB (perfect quasi-two-dimensional structure) to 1.94 µB. Despite the observed changes of the electronic and magnetic properties with increasing impurity cluster, most of the MoS_2 structures still retain direct band transition. These facts suggest the possibility of using two-dimensional MoS_2 as a structural element for sensor and spintronic devices.
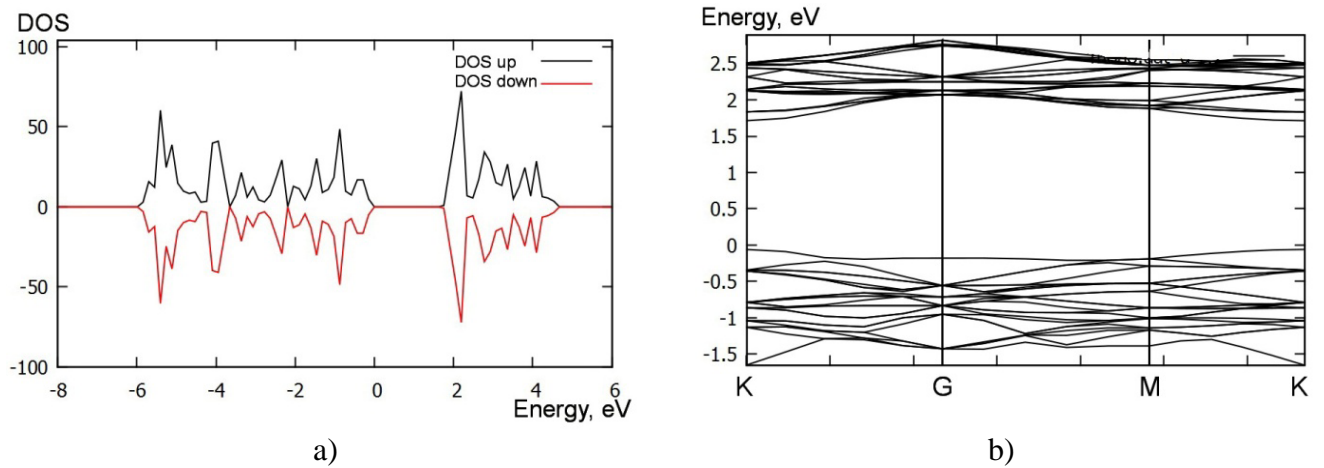
Figure 2 – DOS (a) and energy bands (b) of the perfect quasi-two-dimensional MoS_2 structure
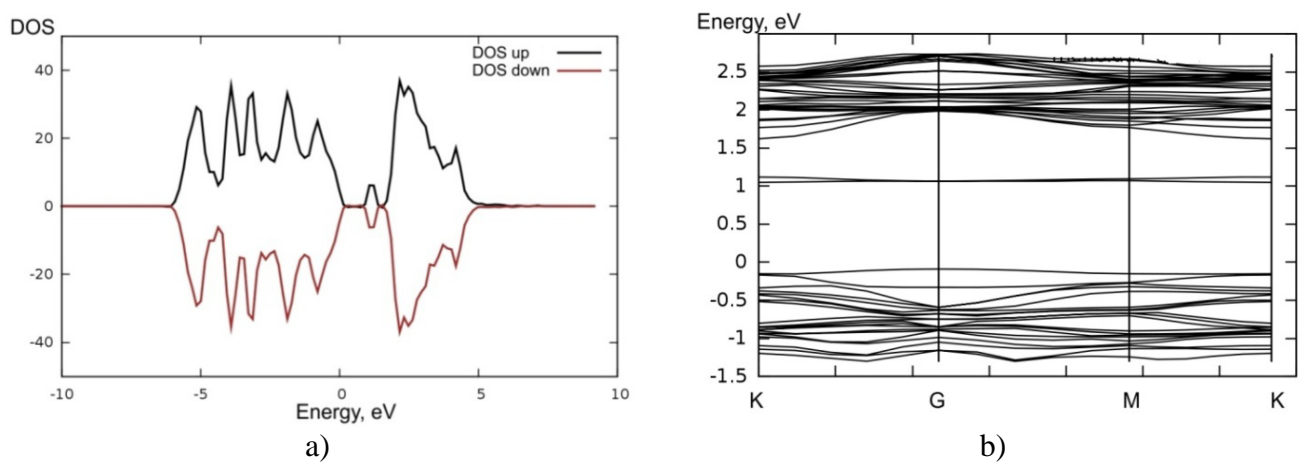
Figure 3 – DOS (a) and energy bands (b) of quasi-two-dimensional
MoS_2 structure with two Co-impurity clusters

Thus, within the framework of density functional theory using the software package VASP spin-dependent properties of quasi-two-dimensional MoS_2 structure with different size of Co impurity cluster were studied. Iit was shown a significant effect of Co impurity cluster on the electronic and magnetic properties of MoS_2. Further research in this area will allow to study in detail and explain the effect of impurities on the characteristics of investigated semiconductor.

REFERENCES

[1] B. Radisavljevic, A. Radenovic, J. Brivio, V. Giacometti, Single-layer MoS_2 transistors, Nature Nanotechnology, 2011, Vol. 6, P. 147–150.

[2] A. Gulay. Y_2O_3 and MoS_2 electronic properties simulation // MEMSTECH'2011. – P. 111 – 114.

[3] E. Kadantsev, P. Hawrylak. Electronic structure of a single MoS_2 monolayer / Solid State Communications. – Vol. 152. – 2012. – P. 909 – 913.

[4] O. Kozlova, V. Lyskousky, V. Nelayev. Electronic properties of ternary compounds with vacancy clusters: ab initio simulation // Mater. Phys. Mech.– No 2. – Vol. 13. – 2012. – P. 124 – 129.

[5] G. Kresse, J. Joubert. From ultrasoft pseudopotentials to the projector augmented-wave method / G. Kresse // Phys. Rev. B – 1999. – Vol. 59. - P. 1758-1765.

[6] G. Kresse. VASP the guide: tutorial / G. Kresse // Austria, University of Vienna. – 2003. – P. 94 – 104.

SIMULATION OF INTERACTION BETWEEN BACILLUS SUBTILIS BACTERIA AND SILICON SURFACE

V. Nelayev[1], V. Burko[1], V. Stempitsky[1],
E. Kolomiets[2], V. Kuptsov[2], A. Berezhnaya[2]
[1] *Belarusian State University of Informatics and Radioelectronics, Minsk, Belarus*
[2] *Institute of Microbiology of National Academy of Sciences of Belarus*

Abstract – The investigation of the physical and energy affinity between *Bacillus Subtilis* bacterial cell wall and the silicon surface is discussed in the frame of finding optimal conditions for efficient immobilization of bacteria in porous silicon.

I. INTRODUCTION

The high chemical toxicity of pesticides is strong stated fact. Now it is the main ecologic problem in the world. Consequently, it is needed to create safe and effective biological products for plant diseases struggle. Biopesticides, in contrast to chemical pesticides, are generally characterized by high selectivity of action against harmful organisms and by lower non-target kinds toxicity. Endophytic bacteria are used as the base of such biopesticides. They penetrate into the inner plant tissues and prevent the ingress of pathogens diseases into the plant organisms. Next problem is the immobilization of the bacteria in special "containers", for example, in pores of porous materials. We investigate the possibility of the above problem solution in the frame of molecular dynamics methodology.

II. OBJECTS OF INVESTIGATION

In this work we investigate the possibility of use a porous material (porous silicon as wide known material in microelectronics), which is the biologically active material at the expense of increased chemical reactivity, as a container for the Bacillus Subtilis bacteria. Bacteria, located in the pore, is isolated from external influence, i. e., it is "preserved" and its fermentation processes are slowed, which will extend the term of the storage and simplify transportation conditions. The problem is to determine the physical and energy affinity between Bacillus Subtilis bacterial cell wall and the silicon surface in order to find optimal conditions for efficient immobilization of bacteria in porous silicon.

Bacterial protoplast is surrounded by peptidoglycan, which is essentially one giant molecule, "crosslinked" through glycosidic and peptide bonds, and composing the bulk of the cell wall of Gram-positive bacteria, which include the Bacillus Subtilis bacteria.

Thus, investigation objects are the fragment of Baillus Subtilis bacterial cell wall (single-layer system of peptidoglycan molecules (Fig. 1 and 2)) and the surface of silicon with the main crystallographic orientations <110> and <001> [1, 2, 3]. Silicon with crystallographic orientation <111> is not considered in this research, because this orientation is not peculiar to the pores of silica. Since the a typical pore of silicon size order of several microns, and the size of the cell wall fragments order of tens of nanometers, it is possible to neglected the curvature of the pore walls.

III. METHODOLOGY

Modeling the interaction between single-layer system of peptidoglycan molecules and silicon surface performed using HyperChem software package intended for the quantum-mechanical (first-principles) and molecular-dynamic simulations of atomic structures. Force fields used by HyperChem are MM+ (based on the MM2), Amber, OPLS and BIO+ (based on the CHARMM) [4]. The simulated murein layer is a 16 repeating peptidoglycan molecules that linked together by peptide bridges, as shown in Fig. 2. Obtained structure of murein is shown in Fig. 3. The spatial optimization of the murein structure with a view to minimize the potential energy performed using a force field Mm+ and spatial optimization algorithm of Polak-Ribiere [5]. The minimum total energy of a single-layer murein molecule is about 325 kcal/mol with a standard deviation equal to 0.01 kcal/mol.
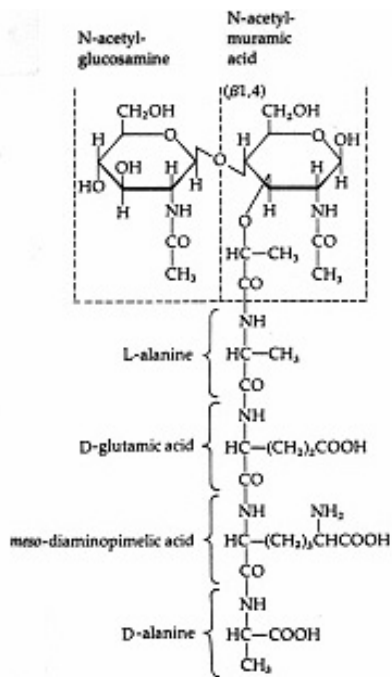
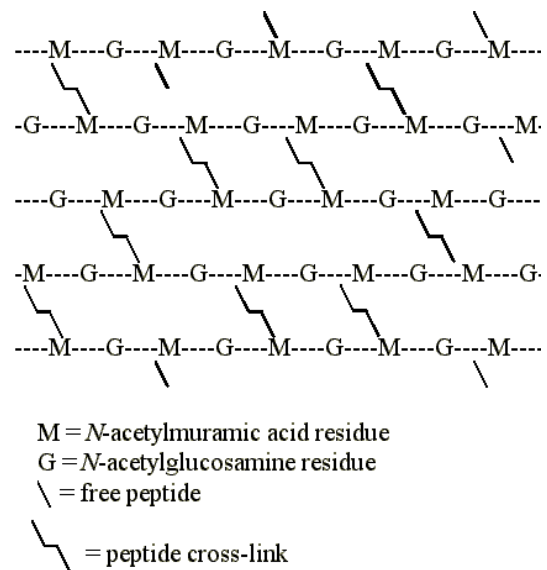Figure 1 – The structure of the repeating
peptidoglycan molecules

M = *N*-acetylmuramic acid residue
G = *N*-acetylglucosamine residue
\ = free peptide

= peptide cross-link

Figure 2 – The single-layer system
of peptidoglycan molecules

IV. RESULTS AND DISCUSSION

Simulation results of the interaction between obtained murein layer and the surface of silicon with the crystallographic orientation <110> showed that decreasing the distance between the silicon surface and murein, magnitude of the total potential energy of the murein layer decreases to ~30 kcal/mol (at the distance ~3Å between molecular monolayer system murein and the silicon surface), which indicates a good affinity between murein layer and surface of silicon with this crystallographic orientation. The results of modeling the interaction between murein and the surface of silicon with the crystallographic orientation <001> showed that the total potential energy of the molecule murein decreased to only ~98 kcal/mol, which indicates that the physical and energetic affinity between the murein layer is best possible when silicon has crystallographic orientation <110>.
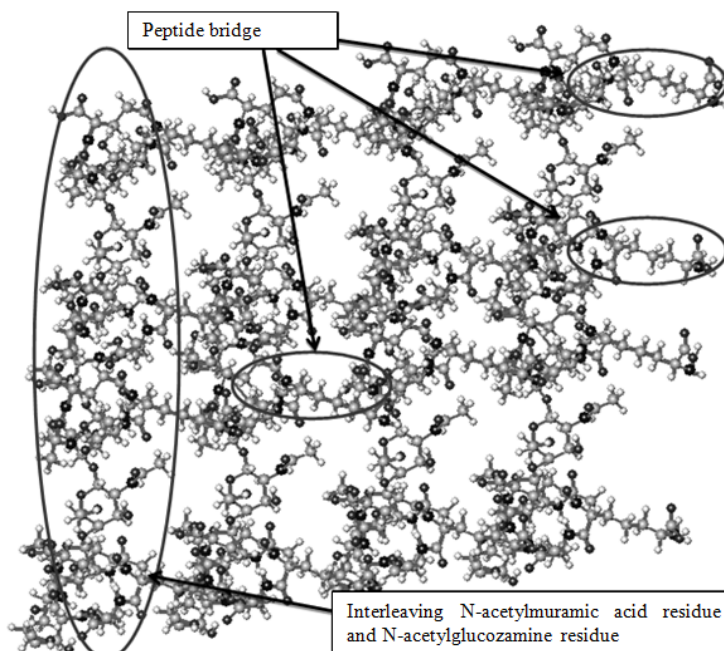
Figure 3 – Single layer of peptidoglycan molecules

127

V. Conclusion

Thus, the results of investigation presented in this paper showed: the possibility of using porous silicon as a container for transportation and storage of Gram-positive bacteria such as Bacillus Subtilis bacteria; an effective method for solving such problems is the method of molecular dynamics; the surface of silicon with crystallographic orientation <110> is the best affinity to single-layer of peptydoglican molecules, which is the cell wall of Gram-positive bacteria.

References

[1] W. Vollmer, D. Blanot, M. Pedro, *"Peptidoglycan structure and architecture" FEMS Microbiol. Rev.*, vol. 32, pp 149–167, 2008.

[2] K. Todar, *The Genus Bacillus*. [Electron resource] – Access mode: http://textbookofbacteriology.net/.

[3] M. Blaber, *The Bacteria*: *An Introduction*. [Electron resource] – Access mode: http://www.mikeblaber.org/oldwine/bch5425/lect10/lect10.htm/.

[4] HyperCube Inc. Official site HyperChem [Electron resource] – Access mode: http://www.hyper.com/.

[5] N. L. Allinger, J. Am. Chem, Conformational analysis 130. MM2. A hydrocarbon force V1 and V2 torsional terms, Soc., 99, p. 8127, 1977.

AUTHORS INDEX

NEW APPROACHES TO HIGH-TECH: NANO-DESIGN, TECHNOLOGY, COMPUTER SIMULATIONS

Proceedings of 15th International Workshop NDTCS'2013
June 11-15, 2013, Minsk, Belarus

Computer design and composing by V. Stempitsky

Published in author's edition